FOSSIL ENERGY

DOE/BC/14977-11
(DE96001259)

IMPROVED EFFICIENCY OF MISCIBLE CO_2 FLOODS AND ENHANCED PROSPECTS FOR CO_2 FLOODING HETEROGENEOUS RESERVOIRS

Annual Report for the period
April 18, 1995 through April 17, 1996

By
Reid B. Grigg and David S. Schechter

October 1996

Performed Under Contract No. DE-FG22-94BC14977

New Mexico Petroleum Recovery Research Center
New Mexico Institute of Mining and Technology
Socorro, New Mexico

Bartlesville Project Office
U. S. DEPARTMENT OF ENERGY
Bartlesville, Oklahoma

DISCLAIMER

This report was prepared as an account of work sponsored by an agency of the United States Government. Neither the United States Government nor any agency thereof, nor any of their employees, makes any warranty, expressed or implied, or assumes any legal liability or responsibility for the accuracy, completeness, or usefulness of any information, apparatus, product, or process disclosed, or represents that its use would not infringe privately owned rights. Reference herein to any specific commercial product, process, or service by trade name, trademark, manufacturer, or otherwise does not necessarily constitute or imply its endorsement, recommendation, or favoring by the United States Government or any agency thereof. The views and opinions of authors expressed herein do not necessarily state or reflect those of the United States Government.

This report has been reproduced directly from the best available copy.

Available to DOE and DOE contractors from the Office of Scientific and Technical Information, P.O. Box 62, Oak Ridge, TN 37831; prices available from (615) 576-8401.

Available to the public from the National Technical Information Service, U.S. Department of Commerce, 5285 Port Royal Rd., Springfield VA 22161

DOE/BC/14977-11
Distribution Category UC-122

Improved Efficiency of Miscible CO_2 Floods and Enhanced Prospects for CO_2 Flooding Heterogeneous Reservoirs

Annual Report for the period
April 18, 1995 through April 17, 1996

By
Reid B. Grigg and David S. Schechter

October 1996

Work Performed Under Contract No. DE-FG22-94BC14977

Prepared for
U.S. Department of Energy
Assistant Secretary for Fossil Energy

Jerry F. Casteel, Project Manager
Bartlesville Project Office
P.O. Box 1398
Bartlesville, OK 74005

Prepared by
New Mexico Petroleum Recovery Research Center
New Mexico Institue of Mining and Technology
Socorro, New Mexico 87801

Table of Contents

List of Tables vi

List of Figures vii

ABSTRACT x

EXECUTIVE SUMMARY 1

INTRODUCTION 2
- Background 2
- Program Objectives 2
- Report Content 2

TASK 1: CO_2-FOAMS FOR SELECTIVE MOBILITY REDUCTION 3
- Introduction 3
- Experimental Work to Verify the Existence of SMR 4
  - Parallel Flow System 4
    - Flow Behavior of CO_2 and Brine 5
    - Flow Behavior of CO_2-Foam 6
  - Series Flow System 6
- Modeling Work to Assess the Usefulness of SMR 8
- Conclusions 9

TASK 2: REDUCTION OF THE AMOUNT OF CO_2 REQUIRED IN CO_2 FLOODING 11
- Introduction - Background 11
- Reduction in Operating Pressure for CO_2 Flooding 11
- Improvement in Mobility Control 12
- Experimental Tests 13
  - Phase Behavior Tests 13
    - Conventional PVT Study 13
    - CO_2 Swelling Tests 13
  - Continuous Phase Equilibrium Tests - Spraberry Recombined Reservoir Oil 15
  - Slim Tube Tests - Spraberry Oil at 138°F 16
  - CO_2 Foam Coreflood Test 16
    - Experimental Descriptions 16
    - Results and Discussion 17
      - Test Series I 17
      - Test Series II 17
  - Summary and Conclusions 18
- Modeling 18

Foam Simulations 18
Foam Model 19
Foam Simulators 20
Compositional Foam Simulator 20
Pseudo-Miscible Foam Simulator 21
Results and Discussion 21
Test Problem I 21
Test Problem II 22
Test Problem III 22
Horizontal Well Simulations 23
Well Model 23
Modifications to MASTER 23
Validation Results 23
Conclusions - Modeling 24

TASK 3: LOW IFT MECHANISMS WITH APPLICATION TO MISCIBLE FLOODING IN FRACTURED RESERVOIRS 25
Introduction 25
Studies on Low IFT Measurement 25
Background 25
Method Description 27
Experimental Apparatus 29
Results and Discussion 29
Summary 30
Investigations on CO_2 Gravity Drainage 31
Background 31
Equilibrium Gravity Drainage 31
Low IFT and Non-equilibrium Gravity Drainage 32
Laboratory Experiments 33
Core Samples 33
Oil 33
Results 33
Discussion 34
Mathematical Models 34
Model Description 34
Comparisons 37
Equilibrium Gravity Drainage 37
Non-equilibrium Gravity Drainage 37
Discussion 38
Summary 39

NOMENCLATURE 40

REFERENCES 42

Appendix A. Formulation of Free-fall Gravity Drainage 49
Assumptions 49
Governing Equation 49
Solution 52

Appendix B. Numerical Solution of Diffusion Equation 53
Assumptions 53
Governing Equation 53
Initial Condition 53
Boundary Conditions 53
Numerical Solution 54

CONCLUDING REMARKS 107

ACKNOWLEDGMENTS 107

List of Tables

TABLE 1
Sulimar Queen separator oil - CO_2 swelling test @ 70°F 56
TABLE 2
Spraberry recombined reservoir oil - CO_2 swelling test @ 75°F 57
TABLE 3
Composition of synthetic brine 58
TABLE 4
Berea core properties 58
TABLE 5
Summary of baseline experiments 59
TABLE 6
Summary of foam tests 59
TABLE 7
Reservoir data 60
TABLE 8
Pendant drop parameters for 7 pure substances 60
TABLE 9
Surface tension values in mN/m from pendant drop measurements 61
TABLE 10
Composition of oil produced by gravity drainage 62

List of Figures

Figure 1. Schematic diagram of the axial sectional area of a composite parallel core. 63
Figure 2. Schematic diagram of the high pressure experimental apparatus for a parallel composite core. 64
Figure 3. Flowing quality behavior of CO_2/brine in a parallel Core (I). 65
Figure 4. Flowing quality behavior of CO_2/brine in a parallel Core (II). 65
Figure 5. Effluent profiles in a simulated parallel core with higher permeability region in the center. 66
Figure 6. Effluent profiles in a simulated parallel core with lower permeability region in the center. 66
Figure 7. Foam flowing quality behavior in a parallel core (II). 67
Figure 8. Foam flowing quality behavior in a parallel core (I). 67
Figure 9. Mobility dependence on permeability in parallel composite cores at darcy flow velocity of 4.3 ft/day. 68
Figure 10. Mobility dependence on permeability in a series composite core. 68
Figure 11. Schematic of the mobility measurement experimental setup for a series composite core. 69
Figure 12. Mobility dependence on displacing fluid on permeability. 69
Figure 13. Oil recovery or vertical sweep efficiency for a five-layer reservoir model. 70
Figure 14. CO_2 density versus pressure and temperature. The points indicate CO_2 density at a number of system MMP's. 70
Figure 15. Density versus temperature comparison for pure CO_2 and CO_2 with extracted hydrocarbon content. 71
Figure 16. Slim tube recovery versus pressure for reservoir oils S and F[27]. 71
Figure 17. Comparison of core-tertiary CO_2 floods from references 15 and 27. 72
Figure 18. Comparison of CO_2 Floods in a visual micromodel with and without foam just above and below the MMP of about 1000 psig. 72
Figure 19. Sulimar Queen Phase Behavior Diagram using separator oil and CO_2. 73
Figure 20. Sulimar Queen phase behavior diagram expanded in the three-phase region for separator oil and CO_2. 73
Figure 21. Sulimar Queen Phase Diagram expanded in the Liquid-Liquid region. Constant upper phase contours shown. 74
Figure 22. Spraberry Recombined Reservoir Oil with CO_2 constant volume % vapor contour lines. 74
Figure 23. Gas volume percent versus pressure for each CO_2 concentration with Spraberry recombined reservoir oil. 75
Figure 24. PV (pressure-volume) curves from three Spraberry Recombined Reservoir Oil with added CO_2. 75
Figure 25. Density and viscosity measurements versus time for both the top and bottom production. Spraberry recombined reservoir fluid with CO_2 at 2450 psig and 138°F. 76
Figure 26. Density and viscosity measurements versus time for both the top and bottom production. Spraberry recombined reservoir fluid with CO_2 at 2100 psig and 138°F. . . 76

Figure 27. Spraberry Recombined Reservoir Oil: Composition versus time in the CPE for the top production at 2100 psig and 138°F. 77
Figure 28. Spraberry recombined reservoir oil: composition versus time in the CPE for the bottom production at 2100 psig and 138°F. 77
Figure 29. Spraberry Recombined Reservoir Oil: Composition versus time in the CPE for the top production at 2450 psig and 138°F. 78
Figure 30. Spraberry Recombined Reservoir Oil: Composition versus time in the CPE for the bottom production at 2450 psig and 138°F. 78
Figure 31. Slim Tube production comparisons versus pore volumes of CO_2 injected for three tests, 1700, 1900, and 2000 psig. 79
Figure 32. Schematic of the coreflood test apparatus. 79
Figure 33. Total mobility of CO_2/brine versus total flowrate for gas fractions of 0.8, 0.667, 0.5, 0.333, and 0.2 (Core A). 80
Figure 34. Total mobility of CO_2/brine versus total flow rate for flow rates of 16.8, 8.4, and 4.2 cc/hr (Core A). 80
Figure 35. Total mobility of CO_2/brine versus gas fraction for total flow rates of 16.8, 8.4, and 4.2 cc/hr and foam mobility versus gas fraction at a total flow rate of 4.2 cc/hr (Core B). 81
Figure 36. Total mobility of CO_2/brine versus total flow rate for gas fractions of 0.8, 0.667, 0.5, 0.333, and 0.2 and foam mobilities at a total flow rate of 4.2 cc/hr (Core B). 81
Figure 37. Pressure drop response of the foam test with 20% foam quality. 82
Figure 38. Pressure drop response of the foam test with 33.3% foam quality. 82
Figure 39. Pressure drop response of the foam test with 50% form quality. 83
Figure 40. Pressure drop response of the foam test with 66.7% foam quality. 83
Figure 41. Pressure drop response of the foam test with 80% foam quality. 84
Figure 42. Comparison of oil rate history for problem I. 84
Figure 43. Comparison of gas-oil ratio for problem I. 85
Figure 44. Comparison of water-oil ratio for problem I. 85
Figure 45. Comparison of cumulative oil production for problem I. 86
Figure 46. Comparison of CO_2 injection profile at 263 days for problem I. 86
Figure 47. Foam resistance factor versus interstitial velocity at 66.7% foam quality and different surfactant concentrations. 87
Figure 48. Foam resistance factor versus interstitial velocity at 80% foam quality and different surfactant concentrations. 87
Figure 49. Foam resistance factor versus interstitial velocity at 85.7% foam quality and different surfactant concentrations. 88
Figure 50. Effect of scaling parameter F on oil rate response for problem I. 88
Figure 51. Comparison of oil rate history between UTCOMP and MASTER for problem II. 89
Figure 52. Comparison of cumulative oil production between UTCOMP and MASTER for problem II. 89
Figure 53. Comparison of oil rate history for problem III. 90
Figure 54. Comparison of gas-oil ratio for problem III. 90

Figure 55. Comparison of cumulative oil production for problem III. 91
Figure 56. Comparison of oil rate history between MASTER and UTCOMP for problem III. 91
Figure 57. Comparison of cumulative oil production between MASTER and UTCOMP for problem III. 92
Figure 58. Comparison of oil rate history for case 3a of seventh SPE comparative solution project. 92
Figure 59. Comparison of water-oil ratio for case 3a of seventh SPE comparative solution project. 93
Figure 60. Comparison of oil rate history for case 3b of seventh SPE comparative solution project. 93
Figure 61. Comparison of water-oil ratio for case 3b of seventh SPE comparative solution project. 94
Figure 62. Geometry of a pendant drop. 94
Figure 63. Sketch of pendant drop experimental setup. 95
Figure 64. Measured IFT for brine/heptane/alcohol system. 95
Figure 65. IFT versus density difference for pure CO_2. 96
Figure 66. Measured ethane densities. 96
Figure 68. Density difference of ethane versus reduced temperature. 97
Figure 67. Surface Tension versus reduced temperature for ethane. 97
Figure 69. Surface tension versus density difference for ethane. 98
Figure 70. Measured phase densities for CO_2. 98
Figure 71. Density difference for CO_2 versus reduced temperature. 99
Figure 72. Surface tension versus reduced temperature for CO_2. 99
Figure 73. Surface tension versus density difference for CO_2. 100
Figure 74. Shape factor/surface tension of pure CO_2 drops. Note change in shape as low IFT is attained. 100
Figure 75. Oil recovery from a Berea core. 101
Figure 76. Pressure history for low permeability core experiment. 101
Figure 77. Oil recovery from a Spraberry core. 102
Figure 78. Corrected oil recovery from the Spraberry core. 102
Figure 79. Solution to demarcator and recovery for Fs = 1.0. 103
Figure 80. Solution to demarcator and recovery for Fs = 0.5. 103
Figure 81. Model calculated dimensionless concentration. 104
Figure 82. Comparison of calculated and observed oil recoveries. 104
Figure 83. Matched and observed oil recoveries from Berea core. 105
Figure 84. Matched and observed recoveries from a Spraberry core. 105
Figure 85. Calculated recovery components for Spraberry core. 106
Figure 86. Calculated recovery components for Spraberry core. 106

ABSTRACT

The overall goal of this project is to improve the efficiency of miscible CO_2 floods and enhance the prospects for flooding heterogeneous reservoirs. This objective is being accomplished by extending experimental and modeling research in three task areas: 1) foams for selective mobility control in heterogeneous reservoirs, 2) reduction of the amount of CO_2 required in CO_2 floods, and 3) low IFT processes and the possibility of CO_2 flooding in fractured reservoirs. This report provides results of the second year of the three-year project for each of the three task areas.

In the first task, we are investigating a desirable characteristic of CO_2-foam called Selective Mobility Reduction (SMR) that results in an improvement in displacement efficiency by reducing the effects of reservoir heterogeneity. Research on SMR of foam during the past year has focused on three subjects: 1) to verify SMR in different rock permeabilities that are in capillary contact; 2) to test additional surfactants for the SMR property; and 3) to develop a modeling approach to assess the oil recovery efficiency of SMR in CO_2-foam on a reservoir scale. The experimental results from the composite cores suggest that the rock heterogeneity has significant effect on two phase (CO_2/brine) flow behavior in porous media, and that foam can favorably control CO_2 mobility. The numerical modeling results suggest that foam with SMR can substantially increase the sweep efficiency and therefore improve oil recovery.

The second task has continued examining increasing the efficiency of CO_2 by decreasing the mass of CO_2 required to produce a barrel of oil by minimizing the flood pressure and/or by using foam to increase the sweep efficiency. During the past year a number of phase behavior tests have been performed for determination of the effect of pressure, temperature, and reservoir fluid composition on recovery efficiency. Coreflood tests have been performed to examine foam formation versus interstitial flow rate and foam quality (volume fraction of gas). The foam tests have been used to develop descriptions of the mechanisms associated with the displacement of oil by CO_2-foam injection that are input parameters for reservoir simulation. The programming and testing of two reservoir simulators and testing on a reservoir scale for the foam option were completed this year. The behavior seen in our simulations closely matched behavior seen in an earlier field CO_2 foam pilot. The horizontal option developed and report in the first annual report was tested and verified during this past year.

In the third task the work in developing methods to measure and predict interfacial tension (IFT) at reservoir conditions has progressed well. Under conditions near miscibility the IFT approaches zero and systematic errors of traditional methods become unacceptable at low IFT. During this past year a new method for determination of low IFT has been developed based on a static force balance on the lower half of the pendant drop. The results of surface and interfacial tension determined using this new method indicates it is more accurate than the traditionally used methods in the low IFT region (IFT < 1 mN/m). A second area of major achievement is the development of a new mathematical model to describe free-fall gravity drainage with equilibrium fluids based on Darcy's law and film flow theory. The new model shows better accuracy than existing models for the 20 sets of experimental data examined.

EXECUTIVE SUMMARY

In Task 1, we have progressed further in our studies in Selective Mobility Reduction (SMR), the property of CO_2-foam by which mobility is reduced by a greater fraction in higher than in lower permeability cores. This property promises to improve displacement efficiency in CO_2 floods by reducing the effects of reservoir heterogeneity. This year we have verified SMR in both series and parallel heterogeneous composite cores. The uneven distribution of fluid in heterogeneous composite cores has been verified and more importantly we verified the positive effect of CO_2-foam in compensating for the effects of heterogeneity in the cores. The favorable effects of CO_2-foam and the augmented positive effect of SMR-CO_2 foams on reservoir scale have been implied using a simple reservoir model.

In Task 2, we have continued work in developing a phase behavior data bank that concentrates on the effects of pressure, temperature, and fluid compositions on the development of efficient CO_2 displacements under reservoir conditions. This information can be used directly to understand phase behavior in reservoir fluid - CO_2 displacements and are also used to determine IFT and solubility parameters under dynamic reservoir conditions. All of these are being used to predict miscibility and recovery in CO_2 displacement under reservoir conditions. Coreflood tests have continued and are being used to identify and quantify a number of variables in foam flooding; effects of flow rate, gas foam quality (gas volume fraction), and surfactant concentration. During the first year foam and horizontal well features were developed. During this second year the foam feature was refined and tested to verify the feature. The foam model under the initial test demonstrated phenomena that were similar to those seen in the East Vacuum CO_2-Foam Pilot Test. This feature has been installed in two types of reservoir simulators and is ready for field tests. The horizontal feature was tested using an SPE test problem and was within the range of fourteen other versions.

In Task 3, we are investigating multiphase flow behavior in fractured reservoirs. Understanding the relationship of fluid flow and reservoir heterogeneity in fractured reservoirs is the key factor in developing a strategy of improving oil recovery in these reservoirs. During this year we have continued to improve on the apparatus for measuring IFT at reservoir conditions. The traditional method for determining IFT using the pendant drop technique works well except at low IFT. A new method for calculation of low IFT has been developed and shown to work at low IFT. The new method is based on a static force balance on the lower half of the pendant drop. The second area of major achievement was the development of a new mathematical model to describe free-fall gravity drainage with equilibrium fluids based on Darcy's law and film flow theory. The ability to measure and predict IFT under reservoir conditions and to describe gravity drainage are necessary developments toward the goal of improving oil recovery in fractured systems that previously have not been seriously considered for CO_2 flooding.

INTRODUCTION

Background

Because of the importance of CO_2 flooding to future oil recovery potential in New Mexico and West Texas, the Petroleum Recovery Research Center (PRRC) has maintained a vigorous experimental program in this area of research for the past sixteen years. This research has been supported by the Department of Energy (DOE), the State of New Mexico, and a consortium of oil companies. Based on encouraging results obtained in a project entitled "Improvement of CO_2 Flood Performance," the DOE awarded a grant to the PRRC in 1989 to transfer promising research on CO_2-foam to a field demonstration site which was a successful forerunner of DOE's Class I, II, and III projects. As part of the field demonstration test, the PRRC provided laboratory and research support for the design of the project entitled "Field Verification of CO_2-Foam," and continued to perform experimental work related to mechanisms involved in CO_2 flooding. The current project is a continuation of the prior work in those and new related areas.

New concepts are being investigated that could provide a more favorable response from the use of foam for achieving mobility control in CO_2 floods, the possibility of obtaining good oil recovery efficiency while still using less CO_2 than is commonly practiced in field operation, and the possibility of CO_2 flooding vertically fractured reservoirs. Each of these areas have potential of increasing oil production and/or reducing cost in fields presently under CO_2 flood are viewed as candidates for future CO_2 flooding. Also, the results of this research should expand viable candidate fields to include lower pressure and much more heterogeneous or fractured reservoirs.

With large quantities of oil unrecoverable in fractured reservoirs, new concepts are being considered for these reservoirs that have the potential of recovering huge volumes of the remaining oil. These new concepts demonstrate the need for research into improvements for CO_2 flooding in heterogeneous reservoirs so that domestic oil recovery from these reservoirs can be maximized and premature abandonment of potentially productive wells prior to implementation of IOR can be avoided.

Program Objectives

The objective of this work consists of an experimental and modeling research aimed at improving the effectiveness of CO_2 flooding in heterogeneous reservoirs. The intent is to investigate new concepts that can be applied by field operators within the next two to five years. The proposed activities will consist of experimental research in three closely related areas: 1) exploration of the applicability of selective mobility reduction, 2) the possibility of higher economic viability of floods at reduced CO_2 injection pressures, and 3) taking advantage of gravitational forces during low IFT, CO_2 flooding in tight, vertically fractured reservoirs.

Report Content

This report describes work performed during the second year of the project. Separate discussions and supporting material are provided for each of the three task areas.

TASK 1: CO_2-FOAMS FOR SELECTIVE MOBILITY REDUCTION

Introduction

The objective of Task 1 is to identify CO_2-foam systems that exhibit selective mobility reduction (SMR) that reduces the mobility of CO_2 by a greater fraction in high rather than low permeability cores in laboratory experiments. Unlike Darcy flow of ordinary fluids in rocks where the mobility is proportional to rock permeability, the mobility of foam with SMR is less than proportional to core permeability and foam flows through higher permeability rocks at a lower rate than would be expected for the given pressure gradient. With such a property, foam can flow at same velocity in high and low permeability regions in the reservoir formations, preserving the uniformity of the flood front while propagating through rocks with non-uniform permeability. Presumably, this can reduce the effect of both vertical and horizontal rock heterogeneity in the reservoir formation, and as a consequence, the use of a CO_2-foam showing SMR would delay CO_2 breakthrough and lead to a greater displacement efficiency in heterogeneous reservoirs.

In the past, the occurrence of SMR has been verified experimentally with separate, relatively uniform and small size core samples.[1-6] Our latest results found the SMR property of CO_2-foam in core samples with permeability ranging from 30 md to 900 md using two different surfactants.[7] Research on SMR of foam during the past year has focused on three subjects: 1) to verify SMR in different permeabilities of rocks that are in capillary contact; 2) to test additional surfactants for the SMR property; and 3) to assess the oil recovery efficiency of SMR for CO_2-foam systems on a reservoir scale.

To examine SMR under more realistic conditions of heterogeneity, laboratory experiments were conducted with one series and two parallel composite core systems. These experiments showed that SMR of CO_2-foam exists in composite, heterogeneous cores that are more characteristic of reservoir conditions. As a consequence, foam with SMR property should be applicable in the field where the high and low permeability sections are in capillary contact. These interesting and striking results lead us to believe that SMR can be used to significantly improve oil recovery from heterogeneous formations that are candidates for CO_2 flooding. Measurements in parallel composite core experiments also gave rise to another interesting result which showed that the rate of CO_2 flow, when coinjected with water, is greater than might be expected through the high permeability region. This effect suggests that in ordinary water alternating with gas (WAG)-CO_2 floods, oil recovery can be even less than expected. Fortunately, the laboratory results also demonstrated that instead of WAG, a much more effective means of simultaneously protecting CO_2 floods against early breakthrough and of increasing overall production from them, is to use a foam flood. Most of these experimental results, which were published in two technical papers[8,9] and presented at two SPE conferences, will be briefly discussed in the following sections.

To assess the efficiency of an SMR displacing agent in a typical oil recovery process, a numerical simulation model was developed. This model was based on the calculation techniques described by Lake[10] and was extended to consider the features of SMR for fluid displacement in parallel layers of a formation. The modeling results, as expected, showed that the sweep efficiency is improved when an SMR fluid is used in the displacement. Even a slightly favorable SMR fluid (which will be discussed later), that shows a slight dependence of mobility on rock permeability, can significantly reduce the number of pore volumes required to achieve the same degree of recovery as that realized with an ordinary mobility reducing agent. We will briefly discuss the modeling results in the last section of Task 1. A more detailed discussion, is found in the paper by Tsau *et al.*.[7]

Experimental Work to Verify the Existence of SMR

In order to experimentally verify the existence of SMR in which both high and low permeability regions are in capillary contact, core systems containing well-defined high and low permeability regions must be used and arranged in the flow system as different portions of a heterogeneous reservoir. Two types of such flow systems, parallel and series, were constructed and experiments were conducted in the laboratory.

Parallel Flow System

The parallel system involves cores in which high and low permeabilities are parallel to the flow direction. Early in our work, we planned a test in which a core would be cut from a rock containing two regions, so that the plane separating the two includes the diameter of the core. End-to-end flows through the two sections are to be kept separate, so as to measure the two mobilities. Our search for samples, from which such parallel heterogeneity cores can be cut, has not produced any candidate cores from reservoirs. We nevertheless have a few samples of quarried rock that meet this standard. Plans have been made to cut a core from a quarried rock with a suitable permeability ratio for the test. In the mean time, the search for core samples having natural heterogeneity is still continuing.

We have been successful in the construction of composite cores with two different coaxial porous systems. Figure 1 shows a schematic diagram of the axial sectional area of a composite core of two regions of permeabilities. The composite cores, 1.40″ (3.56 cm) diameter, consist of a fired berea core with a 5/8″ (1.59 cm) central hole drilled from end to end. This central region is filled with relatively uniform (either sieved or elutriated) silica sand particles. Two series of tests have been conducted in two different composite cores which had permeabilities of 0.5 darcy and 5.2 darcy in the central sandpacks, permeabilities of 1.40 and 1.37 darcy in the annular berea core regions, and were designated as Core (I) and Core (II) respectively.

Fluid inputs of aqueous brine and high-pressure CO_2 entered these parallel core systems from floating-piston cylinders driven by distilled water, from positive displacement injection pumps (see Fig. 2 for system schematic). The input faces of the parallel composite cores were exposed to incoming flow that consisted of CO_2 alone, brine alone, CO_2/brine mixture without surfactant, or a foam mixture of CO_2 with a brine containing either 500 ppm or 2500 ppm of one of three surfactants (Chaser™ CD1045, CD1050, and Enordet X2001). The output flows from the two regions are separated by a circular barrier of the same diameter as the central zone of the composite. Each of the two output regions have their own exit plumbing, each leading into a TEMCO BPR-50 back pressure regulator (BPR) in which the dome pressure was maintained at 2100 psi. The two low-pressure liquid outputs from the BPR's (brine or surfactant-brine) flow into receiving flasks placed on digital scales, while the two outputs of atmospheric pressure CO_2 flow through a wet-test meter and a dry-gas volumeter.

A series of steady-state flow tests were performed on these composite cores to measure overall permeability to brine alone, total mobility during simultaneous flow of CO_2 and brine mixtures, and mobility of CO_2-foam. In all the tests, the mobility λ, was defined in terms of the measured flow rate Q, the pressure drop Δp, the length L, and cross-sectional area A as follows:

$$\lambda = \frac{QL}{A\Delta p} \tag{1}$$

In cases where no surfactant was used, this value is equal to the ratio of permeability to viscosity, or for different phases, the sum of the ratios of effective permeabilities to the viscosities of the corresponding fluids. For foam, where it is difficult to agree on the definition of viscosity, we simply calculate mobility from the equation (which is also directly usable in field calculations), in order that the results may be easily understood.

Flow Behavior of CO_2 and Brine

In parallel flow tests where capillary contact was present between the two permeability regions of the composite cores, the mobility measurements were striking with and without surfactant in the CO_2/brine flow. During the simultaneous flow of CO_2 and brine with no surfactant, capillary contact causes an equalizing flow of brine from the higher to the lower permeability region; and as a result, the high permeability zone water saturation becomes depleted (richer in CO_2), while the low permeability zone increases in water saturation. Figure 3 shows the flowing behavior of CO_2/brine in the first composite core (Core (I)). As indicated in this plot, while the total flowing quality of CO_2 in the system rises rapidly and reaches a plateau at 80% gas quality at about three total injection pore volumes; the flowing quality of CO_2 in the high permeability region (central section) increases swiftly and reaches 85% gas quality after about two pore volumes of total injection. However, the flowing quality of CO_2 in the low permeability region (annulus section) increases slowly and reaches an average gas flowing quality of 60% after about five pore volumes of total injection. The separation of the flowing quality of CO_2 in these two regions increases the mobility ratio in the two zones significantly greater than the permeability ratio. Thus, the rate of CO_2 flow through the high permeability region is even greater than might be expected.

A similar but more significant evidence of such behavior is shown in Fig. 4 where the higher permeability region in the second parallel composite core (Core (II)) is in the annulus section, while the lower permeability region is in the central section. In this case, the brine in the high permeability region (annulus section, having greater cross-sectional area) laterally flows to the lower permeability region (central section). Thus, the central region has a higher water saturation than the annulus of Core (I) with a gas quality less than 60%. As a result, the separation of flowing quality of CO_2 in two regions becomes larger than in the previous examples.

The behavior of such a two-phase flow in a heterogeneous porous system was supported by computational modeling results. The DOE reservoir simulator MASTER,[11] recently modified at the PRRC,[12] was used to verify this experimental observation. By using hypothetical petrophysical data, we simulated the displacement and steady-state flow of CO_2 and surfactant-free brine at the experimental conditions. The computational results qualitatively agree with what has been observed in the laboratory measurements. Figure 5 presents the computational effluent profiles in terms of flowing quality of CO_2 as a function of pore volume of total fluid injected into the Core (I) system. These effluent profiles are similar to the experimental results. A higher quality of gas is flowing through the center portion of system (a high permeability region) compared to that in the annular (a low permeability region). A lower water saturation region in the higher permeability layer in such a parallel flow system apparently is caused by the redistribution of saturation as a result of capillary equilibrium when two different permeability regions are in capillary contact. As a matter of fact, the average water saturation derived from the model calculation is 0.44 in the high permeability region whereas the average water saturation in low permeability region is 0.48. This slight saturation contrast becomes more noticeable in the second parallel system using Core (II) where the low permeability region is in the center.

The effluent profiles for the flow of CO_2 and surfactant-free brine in the second parallel core system are presented in Fig. 6. As indicated from this plot, the flowing quality of gas in the center portion (low permeability region) is much lower than that in the annulus region (high permeability region). The water saturation in the low permeability region increases to 0.54 whereas the high permeability region decreases to 0.46. These computational results indicate that the saturation contrast are a result of the heterogeneity of the porous media. As a consequence, the displacement efficiency could be worse than otherwise expected in a real reservoir formation where nonuniform displacement can be induced simply by the heterogeneity of the reservoir. Fortunately, our foam experiments show that foam can be an effective displacement agent to minimize the saturation contrast, and therefore decrease the mobility contrast between different permeability regions.

Flow Behavior of CO_2-Foam

When surfactant was present in the brine, the qualities of flowing CO_2 in two different permeability regions become more uniform. As shown in Fig. 7, the curves showing the flowing qualities of CO_2 in two sections become closer to each other than observed without foam, see Fig. 4. This indicates that more CO_2 is diverted into the lower permeability section which in turn results in a higher quality of foam in the low permeability region. A similar trend is also observed when foam flows with higher surfactant concentration (2500 ppm). As shown in Fig. 8, the qualities of flowing CO_2 are also similar to each other in both regions. This suggests that CO_2 flow rate is substantially reduced through high permeability section when a foaming agent is used.

To further investigate whether SMR exists in parallel composite core systems, we plotted the mobility of displacement fluids as a function of core permeability on a log-log scale. A typical example is presented in Fig. 9 where the mobilities of CO_2/brine and CO_2-foam are plotted as functions of permeabilities in the regions of the two composite core samples. Since these core systems are not like separate core samples tested before, the fluids behave slightly different when they flow through different permeability regions which are in capillary contact. The mobility curves of CO_2/brine and CO_2-foam increase with increasing permeability in both composite cores. However, the mobility value of CO_2/brine in a high permeability region of Core (II) is much higher than that in the low permeability region of Core (I) when both permeabilities are at a comparable level (i.e., 1.3 d). This difference becomes greater with increasing flow rate. When the surfactant is present in the brine and foam is formed, the separation of mobilities between the two regions of each composite core system is reduced. The decrease of separation demonstrates the effect of using foam to minimize the total mobility contrast between different permeability zones. Moreover, the mobility data in the same graph show a favorable dependence on the rock permeability when foam is present in the composite cores. A line drawn through the data points with the presence of surfactant has a slope much less than the cases where CO_2 and brine flow together. It will be shown later that the slope of this line can be used to indicate the extent of SMR or how favorable the mobility dependence on permeability is in the displacement process. In some cases, we found that the SMR behavior is more evident when surfactant concentration is low and the flow rate is low.[8] But at all tested flow rates (Darcy flow velocities varied from 0.44 ft/day to 8.7 ft/day), SMR existed in the parallel composite core systems when surfactants were present in the aqueous phase.

Series Flow System

The second type of two-permeability region experiment, involving capillary contact between two well-defined permeability regions, is a series flow system. The series assembly uses two cores of ½″ diameter, each about three inches in length. The air permeabilities or these two core sections are 100 md and 500 md respectively. The coreholder that contains them is fitted with five equally-spaced pressure taps, in

such a way that the middle tap is near the junction between the cores. The two abutting end-faces of the cores are carefully cut perpendicular to their axes, and are further ground flat prior to mounting end-to-end. In such an assembly, the unavoidable space between the two core faces is filled with fine sand; and five pressure taps are mounted along the coreholder, defining four segments of the composite rock. The experiment yields records of four pressure differences, between each pair of successive pressure taps and an example of the average permeability of each segment is illustrated in a bottom graph of Fig. 10.

Following the method used in earlier mobility tests with single cores[2-4] and with cores in series in separate coreholders,[5,7] the fluids flowing into this new series assembly (see Fig. 11) are injected by two syringe pumps (a RUSKA for the CO_2, and an ISCO for distilled water forcing brine or surfactant-brine from a floating-piston cylinder). Pressure is maintained almost constant by leading the output fluids into a backwards running ISCO pump, which takes in the output at the total rates of the other two. The four pressure drops are recorded as functions of time after change of the injected fluid, from brine alone to CO_2/brine or CO_2/brine with surfactant. In these experiments, the mobilities of fluids through each segment of the core are calculated and compared when steady state is reached.

The heterogeneity of the series composite core was determined by measuring the brine permeability at four sections along the core. As shown in the bottom graph of Fig. 10, the segmental permeabilities of this series composite core vary from 525 md to 128 md. The brine used consists of 5.6 wt% NaCl and 1.4 wt% $CaCl_2$. Four different surfactants, Chaser™ CD1040, CD1045, CD1050 and Dowfax™ 8390 were used to generate foam with dense CO_2. The experiments were conducted at 77°F and 2000 psig with the total injection rate varying from 5 cc/hr (Darcy velocity of 3.1 ft/day) to 15 cc/hr (9.4 ft/day).

Typical results of mobility dependence on rock permeability of this series composite core are presented in Fig. 10. On this log-log scale plot, the mobility of CO_2/brine or CO_2-foam is plotted against the sectional permeability. Also, included in this plot are the values determined by the regression based on each set of data points. The numerical value represents the slope of each line of each set of data and is used to indicate how favorable the mobility dependence of fluid is to the permeability of porous media. A slope of one indicated that the mobility of fluid is proportional to the rock permeability as described in the Darcy's law. A value of less than one shows a favorable dependence of selective mobility reduction (SMR) which will lead to a more uniform displacement front when the fluid is flowing through heterogeneous porous media. It is not surprising to see that the slope of CO_2/brine data is greater than one. A similar behavior was also observed in the parallel composite core system where the total mobility contrast of CO_2/brine in two differing permeability zones was greater than the permeability contrast. This increase of mobility contrast is analogous to the increase of slope value from one to greater than one, which indicates that the mobility dependence of CO_2/brine becomes worse when the mixture is flowing through the heterogeneous porous media. Nevertheless, the results in the same graph also show that using foam can correct such a problem by not only reducing the mobility of CO_2 but changing the mobility dependence in a favorable direction (*i.e.*, when surfactant is added to the brine and generates the foam, the slope of foam mobility versus rock permeability data becomes less than one).

It is apparent that the extent of SMR depends on the type of surfactant. The slope of five surfactants varied considerably, 0.98 for Dowfax™ 8390, 0.78 for Chaser™ CD1040, and 0.51 for Chaser™ CD1045 and CD1050. As the slope becomes smaller, the flow in a heterogeneous system becomes more uniform. Although the cause of SMR is still unclear, it is expected that the use of CO_2-foam with SMR could minimize the mobility contrast between high and low permeability zones in reservoir flow, thus increasing markedly the efficiency of oil displacement. The above and earlier experimental research makes it clear that SMR of

CO_2-foam is real, is observed in parallel-core and series-core tests with capillary contact, and can be presumed to function similarly in actual field situations. It should therefore be very useful in oil recovery from reservoirs containing crude oil of suitable composition. The question remains, just how useful will it be in oil recovery in a field test. The next section describes our work in attempting to answer this question by numerical simulation of simple field situations.

Modeling Work to Assess the Usefulness of SMR

As demonstrated in our laboratory measurements,[2,3] surfactants have been identified that generate foam which exhibits SMR at reservoir conditions. SMR offers the promise of reducing the variability of flow rates as gas flows through a reservoir with large permeability contrasts between layers. Presumably, CO_2-foam systems could reduce the effect of both vertical and horizontal rock heterogeneity, and as a consequence, delay the breakthrough of CO_2 and lead to a higher displacement efficiency throughout heterogeneous reservoirs. In order to assess the efficiency of SMR for CO_2 injection, we adopted the calculation techniques described by Lake[10] and extended it to consider the features of SMR for displacement through parallel layers of a formation.

Other assumptions considered in this modeling are: 1) one dimensional displacement takes place in a parallel layered reservoir; 2) no communication occurs in the vertical flow direction; 3) the displacement of oil by the displacing fluid is piston-like and the dissipative effects of dispersion and diffusion are ignored; 4) the mobility of the displacing fluid depends on the permeability. Based on these assumptions, equations were derived to calculate successive displacing front positions in each layer, and subsequently to estimate oil recovery as a function of time and injected fluid volume. The equations and details of their derivation are available in the relevant technical paper.[7]

As we demonstrated earlier in the experimental results, SMR can be represented by the slope of the line that, on a log-log graph, shows the variation of mobility with permeability. We can take the mobility of foam as proportional to the permeability raised to a specific exponent (which is the slope of that line) and use it in the numerical calculation. If a foam showed no SMR, and acted like an ordinary fluid, this exponent would be one. If the SMR were perfect (so that there was no variation of mobility with permeability) the exponent would be zero. Systems have been found in which the mobility actually decreases over a permeability range at higher permeabilities.[1-3,5] Over the range where that extreme case is observed, the SMR exponent would be negative. For our purpose here, the exponent considered in the modeling lies between zero and one. In order to cover a greater range, in the event more extensive data were available, a database could be implemented to consider the variation of mobility with permeability in the modeling.

To demonstrate the effect of SMR on oil recovery, we considered a hypothetical five-layer horizontal reservoir in which each layer has the same porosity, thickness, and oil saturation. The permeability, however, varies in decreasing order from 500 md in the top layer to 300 md, 100 md, and 50 md in the middle layers, and 20 md in the bottom layer. The mobility dependence of displacing fluid on permeability, as represented by the SMR exponent, varies from 1.0 to 0.1. Four types of displacement fluid with different characteristics are presented in Fig. 12. The ordinary fluid as shown on this graph is simulated to be like the CO_2/brine mixture. The fluid with SMR exponent of one is simulated to be like an ordinary mobility reducing agent. Two other fluids with differing SMR values are simulated to be SMR enhanced foams. The one with the exponent of 0.75 represents foam with mild SMR. The other with the exponent of 0.1 represents foam with more favorable SMR.

The oil recovery efficiency resulting from displacement of these fluids are presented as a function of pore volumes of injected fluid in Fig. 13. The locations of arrow symbols indicate the breakthrough time at the fastest layer in this reservoir model for all cases. It is clear that breakthrough time of the displacing fluid at the fastest layer is delayed and the vertical sweep efficiency of the model is improved if the mobility of the injected fluid is reduced. At one pore volume of injected fluid, as seen in Fig. 13, the oil recovery of the ordinary displacing fluid is about 63%. The recovery is increased to 72% when the mobility of displacing fluid is reduced but showing no SMR (exponent of 1.0). The oil recovery is improved further to 78% when a mild SMR fluid (exponent of 0.75) is used and to 96% when a nearly complete SMR fluid (exponent of 0.1) is applied as a displacing agent. The benefit of using SMR-enhanced foam becomes more obvious when considering the pore volume of fluid required to achieve the same degree of recovery. In the same graph, for example, the pore volume of fluid required to achieve 90% oil recovery can be reduced from 3.0 PV (no foam) to 2.3 PV (foam without SMR) or to 1.6 PV (SMR foam with exponent of 0.75) or to 0.9 PV (SMR foam with exponent of 0.1). The modeling results suggest that the occurrence of SMR in the displacing fluid can cause substantial increases in the rate at which oil is swept from reservoirs by a miscible phase like CO_2. The value of the increase depends on the amplitude of the SMR and on the extent of the permeability contrasts encountered in the reservoir.

Because the model described here does not account for several features of a real CO_2-foam flooding process, the number presented above are primarily used to show an order of magnitude of the effect of SMR on the oil recovery. In an actual reservoir in which shape, well placement, horizontal as well as vertical permeability variations and fluid properties must be accounted for, a much more detailed and sophisticated reservoir simulation must be used. A method to account for the effects of CO_2-foam with SMR into the simulators would be to carry a variable mobility for the foam phase, in which foam mobility is determined in each CO_2-foam containing cell as a simple power of the cell permeability. As more experimental results become available, this could be improved as suggested above. We will endeavor to develop such a modification in simulators that will be used in CO_2 flood prediction, so that operators can assess the value of SMR foam in their own application.

Conclusions

During the second year of the project, our activities on this task have produced several results of interest. The experimental results from the composite cores suggest that the rock heterogeneity has significant effect on two phase (CO_2/brine) flow behavior in porous media, and that foam can control the CO_2 mobility favorably. The numerical modeling results suggest that foam exhibiting the SMR property can substantially increase the sweep efficiency and therefore improve oil recovery. The experimental and modeling results lead us to the following conclusions:

1. Experiments with composite core samples of known heterogeneity are a better alternative than the separate cores to investigate SMR and to examine the effect of heterogeneity on foam flow behavior. Experiments with composite core samples provide information which cannot be acquired from separate, individual cores of relatively uniform permeability.
2. SMR, in which the CO_2-foam reduces the mobility to a greater extent in high permeability zones than in low, occurred over a wide range of Darcy flow rates (from 0.44 ft/day to 9.4 ft/day) and permeabilities of core samples (from 30 md to 900 md). In many cases, it was observed that low surfactant concentrations were more effective than high, in causing SMR.
3. In experiments with parallel or series flow through higher and lower permeability zones of a composite core, in which the zones were in capillary contact, SMR was still observed.

4. In the same composite core, the presence of surfactant in brine injected with the CO_2 was observed to have a strong beneficial effect on the saturation difference that otherwise develop. This effect decreased the total mobility contrast between different permeability zones.
5. CO_2-foam floods, augmented by SMR, are promising for improved oil recovery. It will cause flow and displacement to be more uniform, thus increasing displacement efficiency.
6. The oil recovery efficiency depends on the extent of SMR and the permeability contrasts that are normally encountered in the reservoir.
7. The SMR effect on the oil recovery can be demonstrated with a simple simulation scheme which can be incorporated into existing reservoir simulators.

TASK 2: REDUCTION OF THE AMOUNT OF CO_2 REQUIRED IN CO_2 FLOODING

Introduction - Background

A multitude of successful gas injection projects throughout the world[13] have demonstrated that high pressure CO_2 injected into oil reservoirs improves oil recovery. It was recently stated[14] that "One of the most significant opportunities for expanding CO_2 could be the application of CO_2 flooding in reservoirs in which near miscible conditions exist." There is considerable economic and operational incentive to operate a gas injection project at the lowest possible pressure. Incentives include, purchasing smaller gas volumes and decreased gas compression costs. Also, the possibility of operating a gas project below the minimum miscibility pressure, MMP, means the reservoirs that might otherwise be excluded could be considered as candidates for gas injection. Some laboratory tests[15-18], simulation studies[19], and field tests [20,21] have indicated that floods at or below the MMP may be as efficient, if not more than at pressures well above the MMP. The unit cost of producing oil by CO_2 injection would decrease if the amount of CO_2 required per unit of oil produced is decreased. This can be achieved by decreasing the mass of CO_2 required to fill a unit reservoir volume by reduction in reservoir pressure or by increasing the sweep efficiency of the CO_2. Sweep efficiency can be increased using mobility control agents and/or horizontal wells.

Reduction in Operating Pressure for CO_2 Flooding

At a constant temperature the density of CO_2 decreases with decreasing pressure, thus increasing the reservoir fill volume with the same mass. It is common that the slope of density versus pressure (density change) is at the maximum near the MMP. The change of density can be substantial over a few hundred psi [22,23], see Fig 14. Also indicated on the appropriate isothermal curve in Fig. 14 are a number of MMP's[15,24-28]. Not taken into account in Fig. 14 is the effect of extracted oil components on the density of CO_2. Figure 15 shows an example of the effect extraction of a small percent of hydrocarbon will have on the density of CO_2[29]. Here the addition of a small amount of hydrocarbons decreased the pressure required to reach a specified density for the CO_2-rich phase. Thus the MMP shifted from that predicted by a temperature correlation for the MMP of CO_2[24,30]. Figure 16 compares the final results of two slim tube tests series (tests used to determine MMP's) at 100°F and 110°F, respectively. The MMP's are over 600 psi different as shown by points S and F in Fig. 14. If the two oils were of similar composition, only a 100 psi shift in pressure due to temperature would have been observed. The prediction of MMP is generally much better when at least a simple oil composition factor is included in the model[31-33]. Using predictive models that consider oil composition the MMP of the two fluids in Fig. 16 are predicted to be about 700-800 psi different, which is much closer to the experimental values.

Another parameter that has been considered to predict MMP's that takes into account the composition of each fluid is the Hildebrand solubility parameter[34], δ, originating from regular solution theory for mixtures of nonpolar liquids such as hydrocarbons. Recently, δ has been described[35] for pure CO_2 and a number of hydrocarbons. The δ increases with density for both CO_2 and crude oils. Since multi-contact miscibility is closely related to the abundance of oil components soluble in CO_2, δ can be used with some degree of accuracy in determining if miscibility will occur and at what rate. The δ of a crude oil is influenced by composition, molecular weight, and temperature. At a given temperature a good approximation of δ is a linear function of molecular weight or API gravity. For CO_2, density is directly related to pressure and temperature. Thus, while pressure has little effect on the oil δ, pressure has a profound effect on the CO_2 δ. By raising the pressure on a system, δ for CO_2 increases while δ for the oil remains essentially constant. Thus the MMP is equal to the point where δ for CO_2 and δ for the oil are close

enough to develop miscibility. As δ for CO_2 increases, more hydrocarbon components are evaporated into the CO_2-rich phase, thus raising δ for the CO_2-rich phase.

A final quantity that can be used to understand the development of miscibility and more important, fluid displacement is interfacial tension (IFT). This is a major focus of Task 3, but here it suffice to say, that theoretically good displacement can occur before complete miscibility, as the IFT is lowered sufficiently to overcome capillary forces[36,37].

Capillary forces imply that a porous structure is involved. A complete understanding of miscibility development must include the incorporation of each of the above concepts in a porous medium. Slim tube studies mentioned above are the simplest porous medium configuration, and have also been an industry standard for determining MMP for a number of years[38]. Slim tube[25,39] and micromodel studies[26] have demonstrated that on a microscopic scale, that the most efficient recovery conditions (mass of oil produced per mass of CO_2 injected) are reservoir pressures at or just below the MMP. Slim tube and micromodel systems are much more homogeneous than reservoir rock, do not contain water saturation, and are composed of glass or unconsolidated sand. Tests or simulations using reservoir rock[15-21] do not necessarily duplicate what has been seen in slim tube and micromodel tests. At least some rock studies indicate that the MMP is not a magic value and at times there is very little difference below and above the MMP in oil recovery. As an example, Shyeh-Yung[15] saw very little difference when comparing recovery in a core test at pressures below and above the MMP. In a more recent study Grigg *et al.* [27] observed the opposite behavior. Some of the results from these two studies are compared in Fig 17. The reduction in recovery below the MMP was as dramatic in core floods as it was in slim tube tests in Grigg's study[27] while Shyeh-Yung[15] observed only a gradual change. The second study[27] indicated that dropping below the MMP can be as critical in a reservoir if not more so as compared with a simple series of slim tube tests. The differences between these results have several possible explanations which include, but we are sure are not all inclusive of the following: reservoir fluid, rock type, experimental procedure, and data interpretation. Thus, it requires additional examination to answer the question of how low relative to the MMP the pressure can be with no loss in the efficiency of CO_2 .

The phase behavior experiments described in Task 2 are used to aid in understanding a number of concepts in increasing CO_2 efficiency. The slim tube tests identify the approximate MMP. The compositional, density and viscosity information obtained from Continuous Phase Equilibrium (CPE) tests are used in determining reservoir condition IFT and δ, and provide required CO_2 flood input data for reservoir simulation. PVT and swelling test data are required for reservoir simulation and should be valuable in IFT and δ developments.

Improvement in Mobility Control

In Task 1, the specific property of SMR in CO_2-foams is being studied. In Task 2, CO_2-foam is also considered, but as a general mobility reduction agent for CO_2. This is especially critical in regions where the microscopic displacement of oil by CO_2 is sufficient, but due to viscosity and/or density differences of the oil and CO_2-rich phases, the macroscopic displacement is adversely effected. In one visual micromodel study (Fig. 18), we have shown that as the pressure is reduced below the MMP the recovery with foam in the system is much better than without foam[26]. Because of favorable laboratory tests[3,26,40] and a successful CO_2-foam field pilot test[41,42], considerable effort has been spent developing CO_2-foam models that can be used in reservoir simulation. Many core tests have been performed to delineate the parameters required in reservoir foam predictions. These tests include foam quality (volume percent of gas injected), flow rates, and surfactant concentration. The foam model has been tested in two reservoir simulators, 1) a multi-

component pseudo-miscible reservoir simulator, MASTER (Miscible Applied Simulation Techniques for Energy Recovery), obtained from the Department of Energy and 2) UTCOMP, provided by the University of Texas at Austin.

Another method that can be used to inject and produce fluids with increased sweep efficiency is properly placed horizontal wells. In the previous annual report[39] a horizontal well subroutine was described. This has been tested further and is in place so we can compare results using foam and other methods of improved sweep efficiency in reservoir models.

Following in this report are more details on phase behavior, slim tube, and coreflood tests and reservoir models that have been developed and tested. Each test has been designed to improve our understanding of CO_2 flood processes and is intended to improve the efficiency of CO_2 flooding.

Experimental Tests

Phase Behavior Tests

Conventional PVT Study

Several types of phase behavior tests are used to develop our understanding of fluids in a reservoir. The first is the conventional PVT study. This is a standard test on a reservoir fluid at reservoir conditions. In general we obtain a separator oil or a weathered oil sample and recombine it with solution gas to the original or present oil reservoir composition. Standard formation volume, viscosity, compressibility, compositional etc. tests are performed to define standard reservoir fluid and produced fluid parameters. These parameters are required for reservoir simulation and as a base for understanding all phase behavior and fluid simulations. A conventional PVT was performed on Sulimar Queen oil during the last year as a preliminary for other studies. The full study is not reported here but will be released in a future PRRC report.

CO_2 Swelling Tests

The second type of test is the CO_2 swelling test. This test consist of injecting an oil into a high pressure windowed cell and incrementally adding CO_2 under reservoir conditions. For each incremental addition of CO_2 the saturation pressure of the system, compressibility above the saturation pressure, and multi-phase volumes below the saturation pressure are determined. Tables 1 and 2 and Figs. 19 through 24 summarize the results of CO_2 swelling tests on Sulimar Queen separator oil and Spraberry recombined reservoir oil.

A Sulimar Queen separator oil swelling test was performed at 70°F. The separator oil was essentially dead oil, therefore the oil bubble point was atmospheric pressure at 70°F. Listed in Table 1 after each incremental addition of CO_2 are the tests pressures, system volume, volume relative to the bubble point pressure volume, volume relative to the original oil, vapor phase volume below the saturation pressure, vapor volume as a percent of total volume, and the volume of the second liquid in and above the three phase region. This was done for nine incremental additions of CO_2. Figure 19 shows the bubble point and dew points along the saturation curves. In this system there is a three-phase region that is common in many low temperature (<120°F) reservoir oil/CO_2 systems[25,43]. The upper pressure boundary of the three phase region in a bubble point pressure curve for the upper liquid phase and the lower pressure boundary is a dew point curve for vapor phase. Through this region the total system volume can decrease to one half under the pressure increase about ten percent and the lower liquid volume changes very little. Thus the large change in volume (density) is in the upper phase(s) with the solvent properties increasing significantly over a small pressure range. Thus, the system at lower pressures goes from a relatively immiscible system to one that multi-contact miscibility develops quickly. In systems with a three phase region, it is conservative to call the MMP the

maximum pressure of the three phase region or for Sulimar Queen about 850 psig. In fact, multi-contact miscibility can and does occur in the three phase region, thus the lowest pressure for the multi-contact miscibility would be the lowest pressure where the three-phase region is found. In the Sulimar Queen that would be around 780 psig. An expanded view of the three phase region is shown in Fig. 20 and extrapolated above 90% CO_2. Figure 21 examines the two-phase liquid-liquid regions above the three-phase region. The phase volume constant contour lines were used to identify the critical point composition and pressure. In the Sulimar Queen system the critical point on the saturation curve was also the low CO_2 concentration apex for the three-phase region. This information will also be used during the next year to calibrate the phase behavior model developed earlier to simulate the phase behavior for this system.

The Spraberry recombined reservoir oil swelling test was conducted at the reservoir temperature of 138°F. The recombination was performed with separator oil and a gas mixture to a reservoir bubble point of about 822 psig at reservoir temperature. This was about 1000 psig under the system examined earlier[39] and closer to the present reservoir bubble point pressure. Listed in Table 2 after each incremental addition of CO_2 are a series of pressures with associated system volume, volume relative to the bubble point pressure volume, volume relative to the original oil, vapor phase volume below the saturation pressure, and vapor volume as a percent of total volume. These values were determined for nine incremental additions of CO_2 and the original oil. Figure 22 shows the bubble point (0% vapor volume contour) and dew points (100 % vapor volume contour) along the saturation curve. Plotted in Figure 22 are the constant vapor (CO_2-rich phase) volume percent contour curves. The contour curves are an aid in determining the critical point that was found to be 69 mole percent CO_2 and 3900 psig. This is within 50 psi of that determined for the higher solution gas Spraberry oil and about 5 mole percent more CO_2. The higher CO_2 concentration should not be surprising since the lower solution gas oil would require more CO_2 to reach the same gas-oil ratio.

As expected the temperature is too high to have a three-phase region in this system. There is not a distinct transitional region as found in the lower temperature systems where there is a transition between a low density vapor and high density liquid in the upper phase. In this system a more gradual change can be seen in Fig. 23.

At lower CO_2 concentrations the saturation pressure can be determined using a pressure-volume curve. In the cases at 0.0 and 31.3 mole percent CO_2, the saturation or bubble point can be determined from the distinct change in slope (compressibility) that occurs in the system when vapor begins to form. At higher CO_2 concentrations, the upper vapor phase has a high density and low compressibility. Thus, a pressure-volume curve cannot be used to determine the saturation pressure. In this case it was a dew point pressure, and as is shown in Fig. 23 there is no apparent slope change at a dew point. Between about 1500 and 2500 psig the compressibility of the upper phase goes from being vapor-like to liquid-like. In this system the CO_2 is at temperatures well about the critical temperature of CO_2, thus it is not surprising that the CO_2-rich phase behaves as a supercritical fluid.

A plot of pressure versus the vapor phase as percent of total volume, shown in Fig. 24, is another graphical method to see a very distinct difference of bubble point and dew point behavior. It can be seen that the composition at 67.7 mole percent CO_2 is nearing the critical point. This type of representation can be used to determine constant volume percent contour lines. Since most of the fluid properties change more gradually in the higher pressure system an estimate of the MMP is not obvious in high temperature phase diagrams.

From the information obtained from these two tests other factors can be determined such as an estimate of the swelling of the system oil and CO_2 content. For example if the pressure of the Spraberry system is 1835 psig the maximum solubility of CO_2 is 42.3 mole percent and the oil would swell 17.4 percent compared to the bubble point pressure value of 822 psig with no added CO_2. Also the amount of swelling would be 21.2 percent over what it would be at 0 percent CO_2 and 1835 psig. These values can be determined from the relative volumes listed in Tables 1 and 2 and the plots found in Figs. 19 and 22. All this information is used to calibrate the phase behavior model developed earlier to simulate the phase behavior for these system.

Continuous Phase Equilibrium Tests - Spraberry Recombined Reservoir Oil

PRRC's continuous phase equilibrium (CPE) apparatus was used to obtain compositions, densities, and viscosities for samples of Spraberry recombined reservoir oil at 138°F at two pressures, 2100 and 2450 psig. This is part of a series of tests from well above the MMP (estimated at 1550 psig) to below the MMP. In these tests high pressure CO_2 is injected continuously at a constant flow rate into a constant volume cell filled initially with the selected oil. The pressure in each test is maintained at a constant value. The constant pressure is maintained by controlling the production rate and alternating the production from the top and bottom of the constant volume cell. As fluid is removed alternately from the top and bottom of the cell densities and viscosities are recorded, at pressure and temperature for each stream. Also, the mass and composition of each stream is measured throughout the tests. For additional details of this process refer to earlier articles[44,45].

Figures 25 and 26 show the results of density and viscosity versus experimental time for both the upper and lower production for both tests, respectively. In both cases the first few hours consisted of injection of reservoir fluid. During this time calibration of the instruments is completed and a steady state is obtained. Upon initiation of CO_2 injection two observations are noted on the plots, the viscosity instantaneously starts dropping and the density of the system increases slightly. The viscosity decrease is the most apparent. This occurred at two hours for the 2100 psig test and three hours for the 2450 psig test. Another phenomenon that is easily observed in Figs. 25 and 26 is phase separation when the system becomes saturated with CO_2. Phase separation is sensitive to both the density and viscosity, showing significant difference in the two phases in both viscosity and density. The more accurate indicator on the time of occurrence is the density. The reason for this is that the viscosimeter is extremely sensitive to two phase flow and particles that might deposit on the quartz crystal such as asphaltenes. Deposition and two phases are common at about the time of phase split, thus erroneous values occur just before and just after phase split in the viscosity readings. The erroneous values are obvious because they are several orders of magnitude off the true value. They are removed for presentation. The density measurements do not have any significant problems in the readouts near the time of phase split and thus are considered the most accurate indicator of phase split.

Figures 27 through 30 show compositional shifts in the upper and lower phases during CPE tests. In each of these figures, CO_2 is excluded, thus normalizing the hydrocarbon fraction of the oil. In both cases the compositions produced from the bottom of the cell changed much less than those produced from the top of the cell. As would be expected the more significant changes occur in the top production after the phase split. The CO_2-rich upper phase had less liquid hydrocarbon dissolved in it than did the lower phase, but note that there was still significant amount of hydrocarbons being extracted by the CO_2-rich phase. The extent of hydrocarbons extracted by the CO_2-rich phase is used to understand the development of miscibility. The tests performed at 2100 and 2450 psig with tests that will be completed during the third year of this project

will aid in understanding miscibility development. These results will then be combined with lower temperature tests on Wasson crude previously[39].

Slim Tube Tests - Spraberry Oil at 138°F

We had some interest in running MMP tests on Spraberry oil that had been weathered at 138°F. Gravity drainage test were being conducted on this oil and required as estimation of miscibility. Tests were performed at 1700, 1900, and 2000 psig and as can be seen in Fig. 31, the systems were not near miscibility. The weathering removed essentially all the components of molecular weight less than decane. The change in MMP calculated due to weathering using compositional[31,32] correlations predicted increases from 2050 to 2175 psig to 4250 to 4500 psig. This compares to a measured value of 1550 psig for the unweathered sample at 138°F[39]. Even though the predictions are high by 500-600 psi for the unweathered sample, the predicted values do show an approximate effect on the MMP for the weathered sample that was void of all hydrocarbons with molecular weights below decane. These three tests will provide information to understand the effect of composition on the development of multi-contact miscibility.

CO_2 Foam Coreflood Test

Application of foam to a reservoir involves injecting a surfactant along with water and gas into the reservoir. To enable the selection of a suitable surfactant for a reservoir, laboratory test data have to be collected to characterize surfactant performance. One of the most important criteria used in surfactant selection is the effectiveness of the surfactant in reducing the mobility of CO_2. A commonly used expression to assess the magnitude of mobility reduction is the resistance factor.[41,46] The resistance factor is defined as the total mobility of CO_2/brine divided by the total mobility of CO_2/surfactant solution, where both mobility measurements are conducted at the same gas-liquid volumetric injection ratio. If foam is not generated, the resistance factor is unity. If foam is generated, the resistance factor quantifies the effect of the presence of foam. Therefore, once the surfactant selection process is complete, the resistance factor data of the selected surfactant generated from various foam tests should be readily available. The relations of surfactant concentration, injection flow rate, foam quality, and rock permeability with resistance factor have been elucidated by recent laboratory foam tests.[6,41,47] Based on these relations, a predictive foam model has been developed[12] and will be presented in the next section.

To provide input data for the foam model, quantitative information on foam-flow behavior at various foam-test conditions is required. Some of the information available in the literature is inclusive and some is not completed. For example, there are some discrepancies about foam mobility behavior with increasing foam quality and with increasing flow rate, and the foam-flow behavior in the lower range of foam quality (below 50%) has never been reported. Therefore, the objectives of this study are to further examine some of the inconsistent information on foam-flow behavior and to explore the information in the lower range of foam quality.

Experimental Descriptions

A schematic diagram of the test apparatus is shown in Fig. 32. Brine, surfactant solution (SS), and CO_2 are loaded into floating piston accumulators and then displaced into the system by using a pump filled with distilled water. The pressure drop across the core is measured by a Honeywell differential pressure transducer (DPT) and by two Sensotec pressure transducers (PT) located upstream and downstream to the core. System pressure is provided by a Temco back pressure regulator (BPR) controlled to the desired run pressure. The test apparatus is housed in an oven to maintain constant temperature. A wet test meter outside the oven is used to monitor gas production. Either CO_2 and brine or CO_2 and surfactant solution can be co-

injected into the system by turning their corresponding pumps on simultaneously. For the purpose of this study, foam was generated in-situ in the core and the foam generator upstream to the core was bypassed.

Foam tests were conducted on fired Berea sandstone cores at conditions of 101 °F and 2100 psig. As a standard procedure for the foam test, the core was first saturated with brine by injecting brine overnight at a flow rate of 5 cc/hr. Then the brine permeability was determined by using several brine injection rates between 5 to 40 cc/hr. Next, baseline experiments were performed by co-injecting CO_2 and brine into the core until a steady-state pressure drop across the core was achieved at various gas-liquid volumetric injection ratios (CO_2 fractions) and at various total flow rates. Note that a gas-liquid volumetric injection ratio of 4:1 corresponds to a CO_2 fraction of 0.8. The resulting mobility data of CO_2/brine for various CO_2 fractions were used to assess mobility reduction of foam. After baseline experiments, the core was flushed with brine to displace CO_2 and brine permeability was determined. Before the co-injection of CO_2 and surfactant solution (foam tests), the core was saturated with surfactant solution at a surfactant concentration of 2500 ppm to bring the adsorption level to a constant. Then, foam tests were run at various flow rates and CO_2 fractions. Each test was run until a steady-state pressure drop across the core was achieved. In the last step, the core was depressurized to ambient conditions and flushed with brine to displace CO_2 and surfactant solution completely. Then the core was pressurized and saturated with brine and permeability was determined. The brine permeability was used to determine whether the conditions of the core had been altered or not.

In all the tests, a synthetic brine with the composition shown in Table 3 was used. The surfactant used in this study was Chevron Chaser™ CD-1045. The surfactant solution was prepared by mixing CD-1045 in the synthetic brine. Information on the cores used in the tests is listed in Table 4.

Results and Discussion

Test Series I In this series of experiments, core A was used. The initial brine permeability of the core was 36.9 md. The results of the baseline experiments are summarized in Table 5. It is clear that flow rate has little effect on the total mobility of CO_2/brine for a fixed CO_2 fraction, as shown in Fig. 33. When the CO_2 fraction is higher than 0.5, the total mobility of CO_2/brine increases with CO_2 fraction; when the CO_2 fraction is lower than 0.5, the CO_2 fraction has little effect on the total mobility of CO_2/brine, as shown in Fig. 34. After baseline experiments, brine permeability was determined to be 45.6 md.

During the injection of surfactant solution into core A, a steady-state pressure drop across the core was never achieved for any tested flow rate. To check the conditions of the core, the core was depressurized, flushed with brine, pressurized, and flushed with brine. However, the initial brine permeability could not be restored (1/3 of initial value) and core A was abandoned. It appeared that the core was partially plugged and can not be recovered.

Test Series II In this series of experiments, core B was used. The initial brine permeability of the core was 195.6 md. CO_2 was then injected into the core and the mobility of CO_2 was determined to be 1148.8 md/cp. After the CO_2 mobility measurement, brine permeability was determined to be 172.6 md. The results of the baseline experiments are also summarized in Table 5. It is clear that the total mobility of CO_2/brine increases with CO_2 fraction when the CO_2 fraction is higher than 0.5, as shown in Fig. 35. The total mobility of CO_2/brine is slightly higher at 16.8 cc/hr than those at 4.2 and 8.4 cc/hr for a fixed CO_2 fraction, as shown in Fig. 36. After the baseline experiments, the brine permeability was determined to be 182.5 md.

During the injection of surfactant solution, a similar behavior to that was observed in core A also occurred. A steady-state pressure drop across the core was never achieved for any tested flow rate. It appears

the foam or surfactant altered the core structures decreasing the permeability with time. Foam tests were then conducted at 4.2 cc/hr for various CO_2 fractions (foam qualities). Note that a CO_2 fraction of 0.5 in a foam test corresponds to a foam quality of 50%. The results of the foam tests are summarized in Table 6. It is clear that the total mobility of CO_2/surfactant solution (foam mobility) decreases with increasing CO_2 fraction, as shown in Fig. 35. This implies that the resistance factor increases with increasing CO_2 fraction. It is interesting to note that, when the CO_2 fraction is less than 0.667, the pressure drop response of the foam test cycles up and down significantly with a peak-to-peak amplitude that varies from 50 psi (for the case of 0.5 CO_2 fraction) to 130 psi (for the case of 0.2 CO_2 fraction), as shown in Figs. 37-39, but the pressure drop response is very smooth with peak-to-peak amplitudes of about 5 to 10 psi for the cases of 0.667 and 0.8 CO_2 fraction, as shown in Figs. 40 and 41. This kind of pressure drop response was also observed for the baseline experiments with much smaller peak-to-peak amplitudes. This might be due to the formation and the breakthrough of a CO_2 bank when the CO_2 fraction is less than 0.667. In addition, the existence of foam can enhance the cycling interval as compared to the baseline experiments.

When the CO_2 fraction was decreased to a previously measured value, the pressure drop was greater than that obtained previously. This might be due to the effect of the strong foam generated at higher CO_2 fraction, such that it would not return to a foam state corresponding to a lower CO_2 fraction. This might be also due to the effects of surfactant and foam, such that the permeability of the core was reduced. The initial brine permeability of the core could not be restored (1/5 of initial value) after the foam tests, therefore, the core was abandoned. Even though the core could not be restored to the original permeability, the mobilities of CO_2/surfactant solution in the foam tests were always two orders of magnitude lower than that of the baseline experiments, as clearly shown in Fig. 35. Currently, a new core is being used. This new core was prepared by using a different firing method and should be able to eliminate the permeability changing behavior that was observed in cores A and B.

Summary and Conclusions

Based on experimental results from phase behavior tests and core flood tests the following summary and conclusions can be made:

1. PVT study on a low temperature medium grade oil has been completed.
2. Several types of CO_2- phase behavior studies have been completed or are in progress for two oils one at a low reservoir temperature (70°F) and one at a moderate reservoir temperature (138°F.). Completed are two continuous equilibrium tests, two swelling-phase behavior tests, and three slim tube tests.
3. Results are being used to analyze the effects of pressure, temperature, and oil composition on the fluid behavior under reservoir conditions during gas injection.
4. Total mobility of CO_2/surfactant solution or foam mobility decreases with increasing CO_2 fraction (foam quality).
5. Total mobility of CO_2/brine increases with increasing CO_2 fraction.
6. Foam resistance factor increases with increasing CO_2 fraction (foam quality).
7. Flow rate has little effect on the total mobility of CO_2/brine.

Modeling

Foam Simulations

Efficient application and evaluation of candidate reservoirs for CO_2-foam processes requires a predictive foam model. Accurate prediction is difficult because the mobility of CO_2 is complex, depending on bubble size or foam texture, and foam texture itself depends on many factors.[48] Despite the complexity

of foam behavior, several approaches for modeling foam displacement can be found in the literature. The first approach[49-53] uses a semi-empirical expression for gas mobility in the presence of foam as a function of flow rate, gas fraction, surfactant concentration, and other factors. The parameters associated with the expression can be obtained from various foam tests. Even though foam texture controls gas mobility,[54] there is no explicit reference to foam texture or foam bubble size in the semi-empirical expression. The second approach[47,48,55-59] uses a bubble population balance model[60] to allow the effect of foam texture to be directly incorporated into an expression for gas mobility in the presence of foam. The bubble population balance model accounts for changes in foam texture caused by mechanisms that create, destroy, or propagate foam in addition to foam trapping and mobilization. Nevertheless, the model parameters of the functional forms chosen for each mechanism need to be fitted to coreflood data from foam tests. The third approach[61,62] relies on the relation between capillary pressure, foam texture, and gas mobility. It is a local-equilibrium version of the bubble population balance model for strong foams under conditions where capillary pressure dominates foam texture and gas mobility. However, as a local equilibrium model, it does not describe some of the foam behavior that depend on flow rate, e.g., foam mobility increases with increasing gas rate.[6,47]

The foam resistance factor[41,46] is a commonly used expression to assess the magnitude of mobility reduction. If foam is not generated, the resistance factor is unity. If foam is generated, the value of the resistance factor quantifies the effect of the presence of foam. The objective of this study is to develop a predictive foam model that can make use of the resistance factor data available from the surfactant selection process. Recent laboratory foam tests[6,46,47] have elucidated the relations of surfactant concentration, injection flow rate, foam quality, and core permeability with the foam resistance factor. Based on these relations, a foam model has been developed and has been incorporated into two reservoir simulators. The first is a pseudo-miscible simulator, MASTER,[63] obtained from the Department of Energy, and the second is an equation-of-state, compositional simulator, UTCOMP,[64,65] provided by the University of Texas at Austin. Both simulators have been successfully modified to simulate CO_2-foam flooding processes where the foam resistance factor data are input as data tables.

Foam Model

A semi-empirical approach is used to calculate the gas mobility in the presence of foam instead of using a mechanistic, bubble-population-balance approach. The gas mobility in the presence of foam is modeled based on resistance factor data which are readily available once the surfactant selection process is done.

The following major assumptions were used in the foam model:

1. Foam affects only the gas mobility.
2. Foam cannot exist if any of the following foam existing conditions are not met:

$$\begin{array}{ll} S_g > S_g^{\lim} & S_o < S_o^{\lim} \\ C_s > C_s^{\lim} & S_w > S_w^{\lim} \end{array} \tag{2}$$

   where C_s is the surfactant concentration in the water phase, and S_g, S_o, and S_w are the gas,- oil-, and water-phase saturations, respectively. The variable with superscript *lim* corresponds to the limiting value of each variable.
3. Foam generation will occur only if (1) the gas-liquid volumetric ratio is greater than a limiting value, (2) the gas saturation is increasing, and (3) the foam existing conditions in 2 are satisfied.

4. Surfactant adsorption on the rock can be modeled with a Langmuir-type model and is unaffected by the presence of foam.

By definition, the resistance factor R_f can be written as

$$R_f = \frac{M_{CO_2+BR}}{M_{CO_2+SS}} \tag{3}$$

where, M_{CO2+BR} is the total mobility of CO_2/brine obtained from the experiment of simultaneous injection of CO_2 and surfactant-free brine, M_{CO2+SS} is the total mobility of CO_2/surfactant solution obtained from the experiment of simultaneous injection of CO_2 and surfactant solution, and both mobility measurements are conducted at the same gas-liquid volumetric injection ratio. The total mobility of CO_2/brine is a combination of the mobility of CO_2 (gas-phase) and the mobility of surfactant-free brine (water-phase), hence,

$$M_{CO_2+BR} = M_w + M_g \tag{4}$$

where M_w is the water mobility and M_g is the gas mobility. Similarly, the total mobility of CO_2/surfactant solution is equal to the sum of the mobility of surfactant solution (water-phase) and the mobility of CO_2 (gas-phase) in the presence of foam. Because the water mobility is not affected by the presence of foam, therefore, the gas mobility in the presence of foam is

$$M_g^{foam} = \frac{1}{R_f}\left(M_w + M_g\right) - M_w \tag{5}$$

If foam can be generated, the foam resistance factor is determined from the data tables, then the gas mobility in the presence of foam is calculated. The calculated value of gas mobility in the presence of foam will not be modified until foam ceases to exist. Gas mobility can be altered by changing either the gas relative permeability or viscosity or changing both together. For convenience, the effect of foam on gas mobility is represented by altering the gas relative permeability only.

Foam Simulators

Two reservoir simulators have been modified to include the foam model. The first is UTCOMP, described by Chang,[64] and the second is the MASTER, described by Ammer *et al.* [63] The resistance factor data, which depend on interstitial velocity, foam quality (gas-liquid volumetric injection ratio or gas fraction), surfactant concentration, and rock permeability, are input as lookup tables in the simulators. The routines that use the lookup tables in the simulators will first locate the intervals for interpolations by checking conditions in the order of permeability, foam quality, surfactant concentration, and interstitial velocity. Then the interpolations are done in the order of velocity, concentration, quality, and permeability. The resistance factor is assumed to be log-linear over velocity and permeability but linear over concentration and quality. At the edges of these tables, simple two-point extrapolation method is used.

Compositional Foam Simulator The basis of the compositional foam simulator is UTCOMP. By utilizing the tracer features in UTCOMP, the compositional foam simulator is developed without the addition of a

surfactant conservation equation into UTCOMP. The tracer adsorption model has been modified to account for the adsorption isotherm. The surfactant movement is tracked by treating the surfactant as the first aqueous tracer component. The major modifications that were made to UTCOMP include (1) the addition of lookup tables for the resistance factor data and (2) the addition of an algorithm to calculate the gas mobility in the presence of foam.

Pseudo-Miscible Foam Simulator MASTER is a pseudo-miscible simulator which is an extension of the so-called black-oil model and uses the mixing-rule approach to calculate effective fluid densities and viscosities. For the technical detail to the equations and miscible features included in MASTER, we refer the reader to the original report by Ammer *et al.* [63] The major modifications that were made to MASTER include (1) the addition of a conservation equation including the adsorption isotherm to permit the simulation of surfactant movement, (2) the addition of lookup tables for the resistance factor data, and (3) the addition of an algorithm to calculate the gas mobility in the presence of foam.

Results and Discussion

To assess the adequacy of the included foam features in UTCOMP and MASTER, several simulation tests on a three-dimensional, quarter five-spot pattern of a reservoir have been performed. Note that these tests did not necessarily represent a real field application. The reservoir is divided into five physical layers. The production and injection wells were located in opposite corners of the pattern and were completed in all five layers. A detailed description of the reservoir data is given in Table 7.

Test Problem I The initial conditions for this problem was established by simulating a 10-year water flood and then a 5-year CO_2 flood from an initial pressure of 1500 psia and an initial water saturation of 25%. The reservoir temperature was 90°F. The reservoir fluid description reported by Lim *et al.*[66] was used because the phase behavior and properties of the oil and CO_2 are typical of multiple-contact-miscible field conditions of West Texas. A modified Corey relative permeability model with water, oil, and gas endpoints of 0.21, 0.71, and 1, respectively, was used. The water injection rate was 129 STB/D (2500 lb-mole/day) during water injection period and the gas injection rate was 275 MSCF/D (800 lb-mole/day) during gas injection period. The production well was limited by a bottom-hole pressure of 1500 psia. The wellbore radius was 0.33 ft for both wells. The foam test was performed using the following injection schedule:

- Surfactant solution (2500 ppm active) injection for 122 days.
- Six rapid cycles of alternating injection of surfactant solution and gas/solvent (SAG) for a total of 90 days. Each SAG cycle consisted of 3 days of surfactant solution injection and 12 days of gas/solvent injection,
- Gas/solvent injection for 153 days.

This schedule was specifically selected to reflect the injection schedule used in a CO_2 foam pilot test at the East Vacuum Grayburg-San Andres Unit (EVGSAU).[67]

In order to evaluate the foam test, a base case was needed. The injection schedule of the base case was identical with that of the foam test except surfactant solution injection was replaced with water injection. Fig. 42 shows the oil rate history for the foam test and the base case. It can be observed that the significant increase in the oil rate at 250 days from about 10 STB/D to about 85 STB/D and then the oil rate dropped and leveled off at about 60 STB/D for the foam test compared to the base case. This kind of response is similar to that observed in the EVGSAU field pilot test as reported by Martin *et al.*[67] in their Fig. 7. Figures 43 and 44 show a corresponding decrease in the instantaneous gas-oil ratio (GOR) and water-oil ratio

(WOR), respectively. Figure 45 shows higher oil recovery for the foam test with an incremental oil of 5 MSTB. To understand the results better, the injection profile for the two cases at 263 days of simulation are shown in Fig. 46. Note that layer 4 is the most permeable layer with a permeability of 1000 md, while layers 2 and 5 are the least permeable layer at 70 md. Figure 46 shows that, for the base case, most of the injected CO_2 would be injected through the highest permeable layer, while the least amount of CO_2 would be injected through the least permeable layers. Consequently, the sweep was poor and the oil rate was low for the base case (Fig. 42). However, for the foam test, there was a significant increase in the amount of CO_2 injected through layers 2 and 5. At the same time, the amount of CO_2 injected through layer 4 was reduced significantly from 76.6% to 1.8% of the total moles injected. Therefore, the profile modification due to the presence of foam significantly improved the sweep and thus resulted in higher oil rate (Fig. 42). These results show that UTCOMP has been successfully modified to simulate foam flooding processes. Figures 47-49 show the resistance factor data used in the simulations, which have been modified from the experimental data reported by Chang and Grigg.[41] The effect of the magnitude of the foam resistance factor on the oil rate was examined by using a scaling parameter F. As shown in Fig. 50, the response to the foam for the oil rate to increase was delayed when the magnitude of the foam resistance factor data was scaled down by the parameter F from 1 to 0.35.

Test Problem II Because of extensive modifications and additions that were made to the code of MASTER, Problem II was designed to validate the capability of MASTER using the results from UTCOMP. In order to compare results from an equation-of-state compositional simulator and a pseudo-miscible simulator, the black-oil PVT properties used in the pseudo-miscible simulator should correspond with the equation-of-state characterization parameters used in the equation-of-state compositional simulator. To satisfy this condition, the reservoir fluid descriptions reported in the fifth Comparative Solution Project[68] were used. In this reservoir system, the oil contained the following mole percents: 50% C_1, 3% C_3, 7% C_6, 20% C_{10}, 15% C_{15}, and 5% C_{20} and the injection gas/solvent contained 77% C_1, 20% C_3, and 3% C_6. PVT properties were generated from the simulations of constant composition expansion and differential liberation expansion for both the oil and the injection gas/solvent. The minimum miscibility pressure is 3000 psia. For detailed reservoir fluid descriptions including PVT properties and characterization parameters, we refer the reader to the original paper by Killough and Kossack.[68]

Test problem II involved five cycles of alternating injection of water and gas/solvent (WAG) for a total of 5 years. Each WAG cycle consisted of 122 days of water injection and 243 days of gas/solvent injection. The water injection rate was 770 STB/D (15000 lb-mole/day) during water injection period and the gas injection rate was 1000 MSCF/D (2900 lb-mole/day) during gas injection period. The production well was constrained to a bottom-hole pressure of 3000 psia. The wellbore radius was 0.25 ft for both wells. The reservoir model is the same as that used in Problem I (Table 7). The reservoir had a temperature of 160°F, an initial water saturation of 20%, and an initial reservoir pressure of 4000 psia. The simulation results from MASTER and UTCOMP were in excellent agreement for the oil rate and the cumulative oil production as shown in Figs. 51 and 52. Besides the validation of MASTER, this problem also provided a check on the fluid descriptions taken from the fifth Comparative Solution Project such that the black-oil PVT properties used in MASTER did correspond with the equation-of-state characterization parameters used in UTCOMP.

Test Problem III To test the foam features in MASTER, the 5-year WAG injection schedule used in Problem II was modified by substituting the foam test schedule used in Problem I for the WAG schedule at the third year. Similarly, the injection schedule of the base case was identical with that of the foam test except surfactant solution injection was replaced with water injection. Figure 53 shows the oil rate history for the foam test and the base case. The oil rate for the foam test was above 100 STB/D for 300 more days

as compared to the base case. The corresponding reduction in GOR can be observed in Fig. 54. By the end of the 5-year injection, incremental oil produced was about 25 MSTB as shown in Fig. 55. These results show that MASTER has been successfully modified to simulate foam flooding processes. This is also confirmed by comparing the foam test results with that of UTCOMP. The foam test results from MASTER and UTCOMP were in good agreement for the oil rate and the cumulative oil production as shown in Figs. 56-57.

Horizontal Well Simulations

Important technological advances during the last decade have made it possible to drill and complete horizontal well economically[69]. Because of the better sweep efficiencies and higher injectivities possible with horizontal wells, all improved oil recovery (IOR) methods would seem to benefit by their use[70-74]. To successfully apply horizontal wells, reliable and accurate tools are needed to aid in the design. A reservoir simulator with horizontal well capabilities can provide guidance into the design of well lengths, locations, and other factors associated with horizontal wells. However, the pseudo-miscible reservoir simulator, MASTER (discussed in the previous section), was only able to handle vertical well simulations; that is, only the vertical well parallel to the z-axis was considered in MASTER. Therefore, the first objective of this research was to incorporate the horizontal well modeling capability into MASTER. The primary motivation of this study was to conduct a systematic investigation of CO_2 flooding using horizontal wells in conjunction with foam.

Well Model

We have implemented the equivalent wellblock radius formulation of Babu *et al.*[75] into the MASTER, because the equation is general and is valid for both vertical and horizontal wells, for any well locations and for any anisotropy. Furthermore, the equation is still accurate for anisotropic grids of high aspect ratio whereas other well model equations required modifications. However, this formulation is very sensitive to non-uniform grids. For a detailed description of the general analytical formula for the equivalent wellblock radius, we refer the reader to the original paper of Babu *et al.*[75].

Modifications to MASTER

In the original MASTER code, the well was represented only as a vertical well parallel to the z-axis. The wellblock productivity index were input from the users. Therefore, the first task was to modify the code to allow for flexible well orientation, that is, wells can be parallel to the x-, y-, or z-axis. Horizontal wells are parallel to the x- or y-axis, whereas vertical wells are parallel to the z-axis. The second major modification involved incorporating Babu *et al.*'s well model into the simulator.

Validation Results

Cases 3a and 3b of the problem given in the Seventh SPE Comparative Solution Project[76] were used to validate the horizontal well model implemented in MASTER. This problem deals with oil recovery by bottom water drive in a thin reservoir where coning is important. Fluids are produced from a horizontal well drilled in the top layer (layer 1), and a constant pressure line source is used to simulate the bottom water drive. The horizontal well produces at a constant liquid rate of 9000 STB/D. Cases 3a and 3b were designed to examine the effect of well length on the recovery. In case 3a, the length of the horizontal producer was 900 ft while it was 2100 ft in case 3b. The length of the constant pressure injector was kept constant at 2700 ft in both cases. For a detailed description of the problem, we refer the reader to the original paper of Nghiem et al.[76].

Figure 58 compares the oil rate history obtained from MASTER with those of the participants in the project for Case 3a. Since there were a total of fourteen participants in this project, we have only used the highest and the lowest results from the band of results produced by the participants indicated as SPE (High) and SPE (Low), respectively, in the legend. The corresponding water-oil ratio (WOR) obtained from MASTER is shown in Fig. 59 as compared to the results from the SPE project. For Case 3b, the results are shown in Figs. 60-61. It is clear that the results predicted by MASTER fall within the range of the results predicted by the fourteen participants in this project.

Conclusions - Modeling

Based on the results from the above simulation tests, the following conclusions are made:

1. A foam model based on the foam resistance factor has been developed.
2. Both UTCOMP and MASTER have been successfully modified to simulate foam flooding processes where the resistance factor data are input as lookup tables.
3. The simulation results show an increase in the oil production rate, attributed to the effects of foam, and are consistent with the observations from the EVGSAU field pilot.
4. The results also show successful profile modification because of the presence of foam, thus resulting in significant sweep improvement.
5. Agreement between MASTER and UTCOMP was good.
6. The horizontal-well feature has been successfully incorporated into MASTER based on the simulation results validated by the solutions of the Seventh SPE Comparative Solution Project.

TASK 3: LOW IFT MECHANISMS WITH APPLICATION TO MISCIBLE FLOODING IN FRACTURED RESERVOIRS

Introduction

Interfacial tension (IFT) provides a logical link between miscibility criteria such as MMP and the flow behavior of near-miscible CO_2/oil systems in heterogeneous reservoirs. The objective of Task 3 primarily concerns facilitating the determination of IFT of CO_2/oil systems and its application to CO_2 injection into reservoirs under a wide range of conditions. The accomplishment of Task 3 would provide reservoir engineers with a reliable method for estimating IFT of CO_2/oil under reservoir conditions.

Surface tension of CO_2 near the critical point has been investigated experimentally. A more accurate method for the determination of low IFT from pendant drop measurements has been developed. Low IFT CO_2 gravity drainage in naturally fractured reservoirs has been studied experimentally and theoretically. Promising experimental results have been matched by a newly developed mathematical model. The results of Task 3 address both fundamental research and research with direct applications to CO_2 flooding.

Studies on Low IFT Measurement

Background

Determination of IFT is of importance in various lines of chemistry, chemical engineering and petroleum engineering[77]. Many techniques of IFT measurements are currently used at different conditions. Detachment techniques, such as Du Nouy ring[78] and Wilhelmy slide[79], rely on the condition of perfect wetting of the withdrawing surface. Capillary rise[80], maximum bubble pressure[81], and drop weight[82] techniques require calibration with liquids of known IFT. They also involve a three phase contact which introduces systematic error. The spinning drop technique[83] is not easy to use for reservoir temperature and pressure applications. Although Laser-Light-Scattering[84] has been used successfully in IFT measurement, it involves systematic error with a high pressure cell where it is not practical for a diffraction grating to be located very close to the liquid surface. The traditional pendant/sessile drop technique, which is not affected by a three phase boundary, has been revived by advances in digital video and image analysis.

The principle of the pendant drop technique relies on measurement of the coordinates of an asymmetric shaped drop and its match to the solution of the Laplace equation. All the information on the value of the IFT is contained in the shape assumed by the drop. Our literature survey indicates that six calculation methods have been developed to extract IFT information from the drop shape in the past six decades: shape factor method, inflection plane method, regression method, direct method, spline-fitting method, and growing-drop method.

The shape factor method is also referred to as the selected plane method. It is essentially based on methodology proposed by Andreas *et al.*[85] who characterized the shape of a drop through the knowledge of various shape factors. Fordham[86] tabulated a parameter (β) relating to IFT with the shape factors proposed by Andreas. Girault *et al.*[87] fit a polynomial to Fordham's data, enabling solutions on the computer. Hansen and Rodsrud[88] solved the Laplace equation and derived a new polynomial for determination of β and IFT from shape of the drop. The shape factor method is easy to use. However, inherent in the method itself are sources of error that scatter the results. Huygens *et al.*[89] reported that the theoretical accuracy of the method is 0.5%, which, however, in practice may increase to 5%. Stauffer[90] concluded that the accuracy of the method was of 2 to 6% for usual size drops encountered in practice for a 1% error in the measurement of the drop dimensions.

The inflexion plane method was first proposed by Girault *et al.*[91] based on the location of the inflexion plane. It was applied to measurement of ultra-low IFT of oil/water systems. They claimed that this method is suitable for determination of IFT from pendant drops that do not have equators (and therefore, necks), although the equation for calculating IFT was derived for a sufficiently long pendant drop. Results from this method are very sensitive to the measured location of the inflexion, and it is difficult to determine accurately the inflexion plane[86].

The regression method was proposed by Girault *et al.*[87] and was used by several researchers[92–94]. This method involves solving the Laplace Equation to obtain a theoretical drop edge. The observed edge is matched to the theoretical edge by adjusting parameters in the theoretical drop. IFT is then extracted from the matching parameters. The main disadvantage of this method is that the solution is not unique due to strong interdependence of multiple parameters. Another disadvantage is the long computation time required due to the iterative nature of the method.

A direct method was proposed by Huygens *et al.*[89] Instead of solving the Laplace equation as done by previous investigators, Huygens *et al*[89] applied the equation on two points on the drop profile. They measured the variables that appear in the equation and substituted their values into the equation for two points. The IFT was determined from solving the two simple equations corresponding to the two points. This method is easy to use compared to other methods. However, Huygens *et al.*[89] reported that this method is not as accurate as the regression method of Rotenberg *et al.*[93]

The spline-fitting method was presented by Lopez de Ramos[96]. This method requires plot of mean curvature versus elevation using drop profile data. IFT is determined from the slope of the plotted line. The drawback of this method is that sometimes the measured data are so noisy that it is impossible to get a linear plot between mean curvature and elevation even if a high smoothing factor is used.

The growing-drop method was proposed by MacLeod and Radke[96] for measuring dynamic IFT. The method was developed on the basis of an assumption that the growing-drop is spherical, which is not always observed in practice. Another drawback of the method is that wetting behavior of the needle tip has a critical impact on the growing-drop measurement. MacLeod and Radke[96] found that with strongly wetting liquids against air in stainless-steel capillaries, they were unsuccessful in overcoming drop climbing.

As IFT gets lower, pendant drops tend to be small and flat.[93,97] In this case the shape factor method is difficult to apply because the diameter of the drop (D_s) at the elevation of equator diameter (D_e) from the apex is strongly affected by the presence of the tip (see Fig. 62). Also wetting behavior deforms the shape of the pendant drop.[96] We have observed that the IFT is erroneous if it is determined based on drop edge above the equator in low IFT systems. The objective of this study was to develop a simple method for low IFT determination using half of the drop profile, i.e., drop edge data below the equator. To avoid the difficulties involved in solving the second-order, non-linear differential (Laplace) equation, we developed a new method based on a static force balance on the lower half of the pendant drop. A simple equation relating the IFT, fluid densities, and drop geometry was formulated. With known profile data from the lower half of the pendant drop, IFT can be calculated quickly from the equation.

It is generally recognized[89,93,95] that the drop information at and near the apex is vitally important because it defines the origin of the drop curve and the curvature information is used to calculate IFT. Unfortunately, as the tangent line at the apex is horizontal, video digitization always gives considerable error in measured coordinates. Our new method requires high quality drop-profile data near the apex of the drop

to determine curvature of the drop surface at the apex. We confirmed the observation by a previous investigator[95] that the results can be completely distorted by experimental noise and noise introduced during digitizing the drop profile. We solved this problem by digitizing rotated drop images, fitting a smoothed spline to the drop profile data, and differentiating this smoothed spline in curvature calculations.

The result of IFT determined using this new method was compared with that given by other methods in the literature for water, normal decane, decyl alcohol, 2,2,4 trimethyl pentane, normal heptane, hexadecane and toluene under ambient conditions. This comparison shows very good consistency among the methods in the high IFT region (IFT > 10 mN/m). Using our pendant drop generating apparatus and image processing system, we tested the new method under various conditions for water, normal decane, ethane, and CO_2. We found that the new method is more accurate than the shape factor method, especially in the low IFT region (IFT < 1 mN/m). This is because the new method allows calculations of IFT from very small droplets as long as the droplets have equators developed. The lowest IFT that we have measured so far is 0.09 mN/m. We believe that by using more powerful lenses for magnifying drop images, even lower IFT can be measured.

Method Description

Figure 62 demonstrates geometry and forces acting on the lower half of a pendant drop. The forces are drop weight W, interfacial tension σ from the upper half of the drop, pressure P_{He} from the upper half of the drop, and buoyancy force P_o from the outer phase. At any equilibrium condition, applying Newton's second law of motion to the lower half of the drop yields:

$$-\frac{\pi}{4}D_e^2 P_{He} - W + \pi D_e \sigma + \int_{x=0}^{x=D_e/2} 2\pi x P_o \cos(a)\, dS = 0 \tag{6}$$

where D_e is equator diameter, P_{He} is pressure in the drop at equator elevation H_e from the apex, P_o is pressure in the outer phase at an elevation corresponding to radial distance x, a is inclination angle of the drop surface at the elevation corresponding to radial distance, and S is the arc length from the apex to the elevation corresponding to radial distance x. P_{He} can be expressed as

$$P_{He} = P_{ai} - \rho_i g H_e \tag{7}$$

where P_{ai}, ρ_i, and g are pressure immediately above the apex, density of the inner phase and gravitational acceleration, respectively. Since

$$P_{ai} = P_{ao} + P_{ca} \tag{8}$$

and

$$P_{ca} = \frac{2\sigma}{R_a} \tag{9}$$

where P_{ao}, P_{ca}, and R_a are pressure immediately below the apex, capillary pressure at the apex, and radius of curvature at the apex (two principal radii of curvature, r_1 and r_2, are the same and equal to R_a at the apex), respectively, Eq. (7) can be rearranged:

$$P_{He} = P_{ao} + \frac{2\sigma}{R_a} - \rho_i g H_e \tag{10}$$

The weight can be expressed as

$$W = \int_0^{He} \pi \rho_i g x^2 dy \tag{11}$$

The arc length is

$$dS = \frac{dx}{\cos(a)} \tag{12}$$

The outer pressure can be expressed as

$$P_o = P_{ao} - \rho_o g y \tag{13}$$

where ρ_o is the density of the outer phase. Substitutions of Eqs. (10), (11), (12) and (13) into Eq. (6) give

$$-\frac{\pi}{4} D_e^2 \left(P_{ao} + \frac{2\sigma}{R_a} - \rho_i g H_e \right) - \int_0^{H_e} \pi \rho_i g x^2 dy + \pi D_e \sigma + \int_0^{D_e/2} 2\pi x \left(P_{ao} - \rho_o g y \right) dx = 0 \tag{14}$$

Interfacial tension σ can be solved from this equation to yield:

$$\sigma = \frac{\frac{g}{D_e}\left(\int_0^{H_e} \rho_i x^2 dy + \int_0^{D_e/2} 2\rho_o x y dx \right) - \frac{1}{4} D_e \rho_i g H_e}{1 - \frac{D_e}{2R_a}} \tag{15}$$

If the drop profile $y = f(x)$ is measured, R_a and integral in Eq. (15) can be evaluated to determine interfacial tension σ.

Experimental Apparatus

Figure 63 shows a sketch of our experimental setup for pendant drop measurement. Up to 18 needles can be installed in a high pressure cell for forming pendant and sessile drops of different sizes. Fluids are circulated by a pump through the measuring cell, where pendant drops are formed, and a density meter to measure densities of the two phases. A circulating water bath is used to control the temperature of the measuring cell and the density meter. Pressure and temperature in are measured by a pressure indicator and a thermometer. The box indicated by the dotted line represents the air bath. The temperature in the water and air bath are regulated at measuring conditions. Pendant/sessile drops are imaged by a CCD video camera. Drop images are sent to the VCR, monitor and computer for data processing. IFT is calculated from the image profile by the computer. The density meter is a PAAR mPDS 2000. The Video camera is a SANYO VCB-3524 with a 1.5 Tele conversion lens, C-Mount Lens Adaptor, and a video monitor. The image processing software is EPIX SVIP version 7.0 for windows. The circulating pump is a high speed LDC analytical miniPump. Needle sizes range from 0.23 mm to 0.90 mm. For calibration uses, accurately cut metal collars are attached around the needles.

Results and Discussion

The new method was first tested using experimental data obtained under ambient conditions. Pendant drop profile data were taken from Lopez de Ramos.[95] Drop dimension parameters, D_e and H_e, were determined from the drop profiles. The radius of curvature at the apex R_a was numerically calculated using the profile data. Parameter values for 7 pure substances are shown in Table 8. Surface tensions of the 7 substances were calculated with Eq. (15) and are shown in the last column of Table 9. Table 9 also contains surface tension data reported in the literature for comparison. Jasper's[98] data was collected from the physical chemistry literature. Hansen and Rodsrud's[88] data was obtained using the shape factor method. Lopez de Ramos's[95] data was calculated from the spline method. Comparisons between literature reported surface tension data and that obtained using the new method indicate consistency in the high tension region. Also included in Tables 8 and 9 are experimental data obtained from our laboratory for water and decane under various conditions for comparison. The data indicate that the result given by the new method is lower than that given by the shape factor method at elevated pressure and temperature. Figure 64 shows experimental data obtained for the brine/heptane/iso-propanol system. This figure indicates that the IFT determined using the shape factor method begins to deviate from the theoretical trend (scaling law) at an IFT approximately equal to 0.2 mN/m. In order to assure that the deviation is a result of application of the method used for extracting IFT from pendant drops, rather than fluid properties, we also measured IFT of pure CO_2. The result is shown in Fig. 65 which indicates the divergence of calculated IFT by the shape factor method from the theoretical trend when IFT is below 0.5 mN/m.

Surface tension of ethane was also measured in our laboratory for comparison. Figure 66 presents measured density data for ethane. Figure 67 shows a plot of phase density difference versus reduced temperature. It can be seen from this plot that the measured data follow the theoretical trend defined by a theoretical slope of 0.325 on the log-log scale. Surface tensions determined by the shape factor method and the new method are plotted in Fig. 68 against reduced temperature. It is seen from the plot that the surface tensions calculated by the new method follow the theoretical trend with a slope of 1.26 on the log-log scale, while the surface tensions calculated by the shape factor method deviate from the theoretical slope when IFT is lower than 0.2 mN/m. Figure 69 demonstrates a log-log plot of surface tension versus phase density difference. Again, it indicates that the surface tensions given by the new method follow the theoretical trend

with a slope of 3.88, while the surface tensions by the shape factor method deviate from the theoretical slope in the low tension region.

In order to know what conditions the shape factor method fails to extract accurate IFT information from CO_2 drops, we conducted a second set of IFT measurements for pure CO_2. Figure 70 shows measured density data for CO_2 liquid and vapor phases along the vapor pressure curve. Phase density difference versus reduced temperatures are plotted in Fig.71. It is seen from this plot that the measured data honors the theoretical trend with a slope of 0.325. Surface tensions determined by the shape factor method and the new method are plotted in Fig.72 against reduced temperature. The plot demonstrates that the surface tensions calculated with the new method follow the theoretical trend with a slope of 1.26, while surface tensions calculated by the shape factor method deviate from the theoretical slope when IFT is below 0.5 mN/m. Figure 73 shows a plot of surface tension versus phase density difference. It also indicates that the surface tensions given by the new method follow the theoretical trend with a slope of 3.88, while surface tensions from the shape factor method deviate from the theoretical slope in low tension region.

The reason the shape factor method fails in the low IFT region is probably due to the effect of the needle tip for small pendant drops. This effect on the drop shape may be reflected by the value of the shape factor (D_s / D_e) of the drop. As IFT gets lower, pendant drop gets smaller, and the shape factor gets larger (approaching unity). Fordham[86] claimed that the shape factor method is accurate for β values between 0.25 and 0.6, which corresponds to shape factor values between 0.6 and 0.95 according to his two-term correlation between β and the shape factor. Hansen and Rodsrud [88] claimed that the shape factor method is accurate for β values between 0.1 and 0.5, which corresponds to shape factor values between 0.46 and 0.91 according to their four-term correlation between β and the shape factor. Figure 74 presents some actual drop images from which IFT of CO_2 was determined in our first CO_2 experiment. Listed below the drop images are corresponding shape factors and IFT. These drops were obtained using a needle size of 0.305 mm in outer diameter. Let us evaluate shape factor values corresponding to IFT values where calculated IFT deviates from theoretical trend. Comparison of shape factors for these CO_2 drops indicates that a surface tension of 0.5 mN/m corresponds to a shape factor of 0.85. Similar comparison of shape factors of drops obtained from our second CO_2 experiment using a 0.406 mm needle indicates that a surface tension of 0.5 mN/m for the system corresponds to a shape factor of 0.86. Comparison of shape factors of ethane drops obtained using a 0.254 mm needle indicates that a surface tension of 0.2 mN/m corresponds to a shape factor of 0.85. Experimental data obtained for the brine/heptane/iso-propanol using a 0.559 mm needle indicates that a surface tension of 0.2 mN/m for the system corresponds to a shape factor of 0.88. It appears evident from this analysis that the shape factor method should fail to extract accurate IFT information from pendant drops that have average shape factor greater than 0.86.

Summary

In the low IFT region, pendant drops tend to be small and flat. The upper portion of the pendant drop is strongly affected by the wetting behavior of the tip. In this case, calculation methods such as the traditional shape factor method are erroneous because drop edge information from the upper, distorted portion of the pendant drop is included in the calculation. A new method for determination of low IFT has been developed based on a static force balance on the lower half of the pendant drop. The result of surface tension determined using this new method was compared with that given by the shape factor method for water, normal decane, decyl alcohol, 2,2,4 trimethyl pentane, normal heptane, hexadecane and toluene under ambient conditions. This comparison shows consistency between the results given by the shape factor method and the new method in the high IFT region (IFT > 10 mN/m). Testing of the new method with IFT measured under various conditions for water, normal decane, ethane, and CO_2 indicates that the new method is more accurate than the shape factor method in the low IFT region (IFT < 1 mN/m).

Investigations on CO_2 Gravity Drainage

Background

Because fractures are highly conductive to injected gas and gas is the nonwetting phase in the rock matrix, gas injection into fractured reservoirs has been traditionally considered as an inefficient method for enhancing oil recovery from fractured reservoirs. However, the Midale Pilot[99] indicated that the efficiency of CO_2 injection into fractured reservoirs is not as low as expected. The only explanation is that when a non-equilibrium gas is injected into the fracture system at elevated pressure, compositional effects become active between the gas in the fractures and oil in the matrix. Due to the multi-contact mechanism, light hydrocarbons in the oil can be extracted from the virgin oil bank forming a "gas"-rich light liquid phase and an oil-rich heavy liquid phase. This kind of phase split has been reported by several investigators[44,45]. The interfacial tension (IFT) between phases is low compared to that between the virgin oil and gas phases. Therefore, the capillary pressure threshold may be overcome by gravity resulting in gravity drainage of oil from the matrix blocks. In order to understand the mechanism of gravity drainage and predict the response of fractured reservoirs to gas injection, a mathematical model of the process is desirable.

Equilibrium Gravity Drainage

Studies on gravity drainage were conducted a century ago when King investigated the principles and conditions of aquifer motion. Investigations of gravity drainage of oil in oil reservoirs were initiated in the early 40's. Leverett[101] and Katz[102] presented data and discussed the theory relating capillary and gravitational forces acting on liquids contained in a sand body. Stahl *et al.*[103] conducted experiments to investigate behavior of free-fall gravity drainage of water and oil in an unconsolidated sand. Elkins *et al.*[104] presented a simplified theory of regional drainage of oil from an upstructure to downstructure location due to gravity assuming zero capillary pressure gradient. Cardwell and Parsons[105] presented a governing equation for the free-fall gravity drainage process. They could not solve the equation because of its non-linearity. By neglecting the term involving the product of permeability and variation of capillary pressure with saturation, they derived a solution for simplified cases using the concept of a demarcator. Terwilliger *et al*[106] conducted experimental and theoretical investigations on gravity drainage performance under controlled flow rates. Their theory was based on the Buckley-Leverett[107] approach. Nenniger and Storrow[108] presented an approximate series solution for free-fall gravity drainage based on film flow theory. The results accurately matched experimental data obtained from a highly permeable pack of glass beads. Essley *et al.*[109] analyzed the gravity drainage process and final oil recovery in a steeply dipping reservoir. Templeton and Nielsen[110] experimentally investigated the counterflow segregation of fluids under the gravitational force field using glass beads. Dumore and Schols[111] performed experimental studies of free-fall gravity drainage of oil in the laboratory and developed a drainage capillary pressure function. Dykstra[112] generalized the approximate theory presented by Cardwell and Parsons[105]. His mathematical model matched some experimental data with assumed permeability values. Hagoort[113] theoretically analyzed vertical displacement efficiencies of forced and free-fall gravity drainage processes. He derived a governing equation for saturation in free-fall gravity drainage, which is identical to that given by Cardwell and Parsons[105] except that he used the Leverett J-function for expressing capillary pressure. He again did not solve the saturation equation because of its non-linearity. Haldorson *et al.*[114] evaluated the gravity drainage mechanism in an oil field using compensated neutron logs, centrifugal displacements and an analytical stochastic approach. Nectoux[115] investigated the velocity influence on sweep efficiency in oil drainage experiments. Compositional effects were also discussed in his paper.

Low IFT and Non-equilibrium Gravity Drainage

Jacquin *et al.*[116] investigated gravity drainage with fluids not in equilibrium. Their laboratory experiments show that the oil recovery by gravity drainage increases if the content of intermediate components in the gas or in the liquid phase increases. Pavone *et al.*[117] conducted experiments to investigate free-fall gravity drainage at low IFT. The IFT of the C_1/C_7 mixture utilized in their experiments was 0.53 dyne/cm. They found that the gravity drainage process can be divided into two time periods. During the first period, almost 50% of the oil in place was produced. The second period of slow drainage began suddenly at a breakpoint whereby the production rate was low but led to more than 20% additional oil recovery. They also presented a non-linear governing equation for gas saturation during drainage. Their governing equation is similar to the one given by Cardwell and Parsons[105]. The governing equation was linearized by assuming straight-line permeability and logarithmic capillary pressure curves. They solved the linearized governing equation analytically assuming that the minimum gas saturation is always at the outlet of the core (the demarcator is always at the bottom of the core). They matched some experimental data by dual use of the analytical solution, i.e., the analytical solution was used twice for early and later times, respectively, to match the same set of experimental data.

Stensen *et al.*[118] performed experiments for analyzing the effect of IFT on gravity drainage. They employed brine and a $C_1/n - C_7$ mixture having IFT ranging from 76 (reported in the paper) to 0.5 dyne/cm. Suffridge and Renner[119] investigated gravity drainage experimentally under constant and varying IFT in fractured and non-fractured cores. The varying IFT was obtained by first placing C_{32} in the core, and then letting C_1 to diffuse into the core. da Vilva and Meyer[120] presented a formulation for oil desaturation curves used for reservoir simulation. Schechter *et al.*[121] reported experimental results of investigations on low IFT imbibition and drainage. They utilized brine/isopropanol/ i–C_8 systems with IFT of 0.1, 1.07, and 38.1 dynes/cm and density differences of 0.11, 0.21, and 0.33 g/cc, respectively. They also presented analyses of imbibition and drainage mechanisms. It was concluded that gravity drainage of wetting phase from fully saturated vertical cores occurs for inverse bond numbers less than 1. Luan[122] discussed theoretical aspects of free-fall gravity drainage in naturally fractured reservoirs. He solved the governing equation given by Hagoort analytically and numerically. However, he used the same boundary condition as that utilized by Pavone et al. , that is, the demarcator is assumed to be always at the bottom of the core. Espie *et al.*[123] investigated gravity drainage/waterflood interaction in the laboratory. They found that injection of water into a gravity drained oil column with high gas saturation improves the mobilization of a dry oil bank. Catalan *et al.*[124] reported their results of investigations on the effects of wettability and heterogeneities on the recovery of waterflood residual oil with low pressure inert gas injection assisted by gravity drainage. Experiments on forced gravity drainage by gas injection under varying pressures were performed and analyzed. They concluded that tertiary gravity drainage in water-wet systems is most efficient when the oil spreads on the water phase in the presence of gas. Blunt *et al.*[125] presented a theoretical and experimental treatment of three phase flow in water-wet porous media from the molecular level upwards. They found that oil spontaneously spreads as a layer between water and gas in most three-phase systems. Their experimental data on gravity drainage in a capillary matched predictions by their theoretical model. Recently Øyno *et al.*[126] conducted laboratory experiments on composite cores at reservoir conditions using recombined reservoir fluids to investigate the potential of secondary and tertiary recovery using gas injection, where gravity drainage is regarded as an important recovery mechanism. Although they recognized that the time required to reach capillary/gravity equilibrium depends on oil/gas density difference, gas/oil IFT, and molecular diffusion in both gas and oil phases, they could not identify conditions whereby each factor dominates.

In summary, the literature reveals that three different gravity drainage processes in porous media have been investigated: (i) forced gravity drainage by gas injection and controlled flow rate, which occurs

when gas is injected into steeply dipping reservoirs, (ii) simulated gravity drainage by centrifuging, which exists only in laboratories, and (iii) free-fall gravity drainage, which takes place in naturally fractured reservoirs after depletion of oil in the fractures or after gas injection into the fractures. The free-fall gravity drainage, which is representative of gas injection into a depleted fractured reservoir, has been investigated by Leverett[101], Stahl *et al.*[103], Cardwell and Parsons[105], Nenniger and Storrow[108], Templeton and Nielsen[110], Dumore and Schols[111], Dykstra[112], Hagoort[113], Jacquin *et al.*[116], Pavone *et al.*[117], Stensen *et al.*[118], Suffridge and Renner[119], Schechter *et al.*[121], Luan[122], and Øyno *et al.*[126]

Unlike forced gravity drainage, free-fall gravity drainage cannot be modeled using a Buckley-Leverett approach because flow rate is not pre-specified. A survey of the literature reveals four mathematical models that have been developed for describing the process of free-fall gravity drainage of equilibrium fluids. They are the Cardwell-Parsons-Dykstra (C-P-D) model, the Nenniger-Storrow (N-S) model, the Pavone-Bruzzi-Verre (P-B-V) model, and the Luan Model. The accuracy of these models are found to be poor based on our comparisons with experimental data. Therefore, we have developed a new mathematical model to simulate equilibrium and non-equilibrium gravity drainage. Comparison of recovery data computed using the new model to experimental data found from both the literature and experiments conducted in our laboratory indicate that the new model can better describe the process of free-fall gravity drainage of both equilibrium and non-equilibrium fluids.

Laboratory Experiments

Laboratory experiments were conducted to simulate vertical free-fall gravity drainage from a matrix block in a naturally fractured reservoir. Core samples were first saturated with synthetic reservoir brine. The brine was then horizontally displaced by separator oil. The oil saturated core was transferred to a vertical core holder which has an inner diameter 0.2 cm greater than the core diameter. During the experiment, CO_2 was continuously injected into the 0.1-centimeter wide annulus (simulating a highly conductive fracture) between the core sample and core holder at reservoir pressure and temperature. Oil recovered from the core was collected at ambient conditions. The key parameter of interest is the oil recovery as a function of time.

Core Samples

One Berea core and one whole reservoir core from the Spraberry Trend Area in West Texas were tested. The Berea core is 61 cm long, is 10.16 cm in diameter, has a 18.7% porosity, has a 500 md absolute permeability, and has a 35% residual brine saturation after oil displacement. The Spraberry core is 55 cm long, is 10.16 cm in diameter, has a 10% porosity, has a 0.01 md vertical permeability to brine, and has a 38.6% residual brine saturation after oil displacement.

Oil

Separator oil produced from the Spraberry Trend Area was used in the experiments. Composition of the oil was obtained from GC analysis. Composition and average molecular weight of the oil are shown in Table 10. The oil sample was tested at 100°F and 1000 psig and at this condition the density was 0.8329 g/cc and the viscosity 2.956 cp. The MMP of the oil and CO_2 by slim tube was found to be 1550 psig at the reservoir temperature of 138°F.

Results

The experiment with the Berea core was carried out under pressure of 1450 psig and temperature of 138°F. The experiment was terminated at six days. The produced oil looks similar to original separator oil. Experimental oil recovery data is plotted in Fig.75. The experiment with the Spraberry reservoir core was

also performed at a temperature of 138°F. However, the pressure varied from 2000 psig to 1500 psig as shown in Fig. 76. The produced oils are yellow, light brown, and brown in color. Composition of the yellow and brown oils are also shown in Table 10. The variations in color and composition are possibly due to fluctuations in pressure and temperature. Density and viscosity of the yellow oil were measured at 60°C and atmospheric pressure. They are 0.82 g/cm^3 and 2.1 cp, respectively. Recovery data is plotted in Fig. 77.

Discussion

Figure 75 indicates fast drainage of oil from the Berea core during CO_2 injection into the annulus of the gravity drainage cell. This is expected because the capillary pressure is already low in the Berea core and a slight decrease in IFT can reduce the capillary pressure threshold to less than the gravity force. The black color of the produced oil confirms that the oil drained before much of CO_2 diffused into the oil bank. However, Fig.77 indicates a very slow process of oil recovery. This is again expected because of high capillary pressure in the tight core. The light color of the produced oil from the Spraberry core indicate the formation of a "gas"-rich liquid phase in the pore space of the core. Comparison of compositions of injected and produced oils clearly shows that the produced oil contains much less heavy hydrocarbons than separator oil does. This comparison also shows that some light hydrocarbons were lost during collection of the recovered oil. This is because the oil was collected under atmospheric pressure and, more importantly, at an elevated temperature that is close to reservoir temperature. Under this condition, some light components should escape with CO_2 in the gaseous state. Material balance calculations indicate that up to 70 volume percent of the oil was lost with the CO_2 gas. By considering the lost volume of the produced oil, recovery data is corrected and plotted in Fig. 78.

Mathematical Models

There is no mathematical model available in literature describing non-equilibrium gravity drainage after gas injection into a depleted fractured reservoir (free-fall gravity drainage). In this study, we simulate the process using mathematical models developed for equilibrium gravity drainage with modifications considering molecular diffusion during gravity drainage. We first tried to select one model among the four existing models: the Nenniger-Storrow (N-S) model, the Pavone-Bruzzi-Verre (P-B-V) model, the Cardwell-Parsons-Dykstra (C-P-D) model, and the Luan Model. Unfortunately, we found none of them accurate enough to be adopted, even for equilibrium gravity drainage. Comparisons of these models are presented elsewhere.[127] Then we decided to develop a new model to simulate equilibrium and non-equilibrium gravity drainage processes.

Model Description

Derivation of the new model is detailed in Appendix A. A summary of the resultant equations is presented in this section. Based on the fact that the volumetric drainage rate is equal to the derivative of draining-phase volume in porous media with respect to time, the following governing equation for the wetting/non-wetting phase demarcator has been formulated:

$$\phi\left[S_{wi}-S_{wr}-\sqrt{\frac{F_s\phi z_D}{5t_D}}\right]\frac{dz_D}{dt_D}+\frac{\phi z_D}{3t_D}\sqrt{\frac{F_s\phi z_D}{5t_D}}-\left[1-\frac{H_D}{1-z_D}\right]=0 \qquad (16)$$

where

$$z_D = \frac{z_d}{L} \tag{17}$$

$$H_D = \frac{H}{L} \tag{18}$$

where

$$t_D = \frac{k_e \Delta\rho g t}{\mu L} \tag{19}$$

where z_d = demarcator depth, L = length of porous medium column, H = capillary pressure threshold, ϕ = porosity, S_{wr} = residual wetting phase saturation, S_{wi} = water saturation, F_s = correction factor to Kozeny equation, t = time, k_e = effective permeability, g = gravitational acceleration, $\Delta\rho = \rho_i - \rho_o$, and μ = viscosity.

Equation (16) is non-linear and is difficult, if not impossible, to solve. Therefore, we solved the equation numerically by rearranging it into the following form:

$$\Delta z_D = \frac{-\frac{\phi z_D}{3t_D}\sqrt{\frac{F_s \phi z_D}{5t_D}} + \left[1 - \frac{H_D}{1 - z_D}\right]}{\phi\left[S_{wi} - S_{wr} - \sqrt{\frac{F_s \phi z_D}{5t_D}}\right]} \cdot \Delta t_D \tag{20}$$

Using initial condition of 0 for z_D at a very small time t_D (0.0001 for example) and a small time step Δt_D, the increment of demarcator (Δz_D) can be calculated from this equation. Then z_D and t_D can be updated by

$$z_{D_{new}} = z_{D_{old}} + \Delta z_D \tag{21}$$

and

$$t_{D_{new}} = t_{D_{old}} + \Delta t_D \tag{22}$$

Repeated use of Eqs. (20), (21) and (22) gives a numerical solution to Eq. (16). Based on the position of the demarcator and the volume distribution of the liquid above the demarcator, the draining-phase recovery R with time t is calculated utilizing Eq. (23).

$$R = \left(1 - \frac{S_{wr}}{S_{wi}}\right) z_D - \frac{2z_D}{3S_{wi}} \sqrt{\frac{F_s \phi z_D}{5t_D}} \tag{23}$$

Derivation of Eq. (23) is also detailed in Appendix A. Two typical solution curves are presented in Figs. 79 and 80 for $\phi = 0.1$, $S_{wr} = 0,1$, $H_D = 0.1$, and $F_s = 1$ and 0.5, respectively. It is clearly seen from Figs. 79 and 80 that the equilibrium gravity drainage process can be divided into two periods. During the first period, the demarcator drops and the total drainage rate is a combination of rate of full-pore flow and that of film flow. During the second period, the demarcator is stabilized and the total drainage rate is the rate of film flow only. It is interesting to note the effects of the parameter F_s on the shapes of demarcator and recovery curves indicated by the two figures. When F_s is greater (less homogeneous rock), as shown in Fig.79, the demarcator stabilizes gradually during bulk flow leaving more recoverable fluid behind for pure film flow to occur. When F_s is small (homogeneous rock), as shown in Fig.80, the demarcator stabilizes sharply at the end of bulk flow leaving less recoverable fluid behind for pure film flow.

Non-equilibrium gravity drainage occurs when a porous medium saturated with one phase is surrounded by another phase not in equilibrium, for instance, injected gas and resident oil. In this case, the surrounding phase migrates into the porous medium due to molecular diffusion causing the IFT of the fluid in the porous medium to change with time. For example, when an oil-saturated, vertically oriented core is surrounded by CO_2 during gravity drainage, the CO_2 diffuses into the core resulting in continuous reduction of IFT between the CO_2-rich phase and the oil phase as CO_2 moves toward the interior of the core. Thus the IFT at any point in the core is time dependent.

Although the new mathematical model is derived assuming that the wetting phase and non-wetting phase are in thermodynamic equilibrium, it is possible to apply the model to simulation of a non-equilibrium gravity drainage process if some modifications are made to account for the non-equilibrium effect due to diffusion. If we divide the core length into many elements along the direction of diffusion, then it is possible to apply the mathematical model to each individual element where uniform fluid properties are assumed. We have developed the following step-wise procedure to simulate the non-equilibrium gravity drainage processes:

1. Estimate the concentration of the gas phase in each element at a diffusion/drainage time;
2. Estimate the average fluid viscosity, density, IFT and capillary pressure in each element at that time based on the composition of the fluid mixture;
3 Apply the mathematical model to each element to estimate liquid recovery from the element at a given time;
4. Sum up the recoveries calculated from each element to get the total liquid recovery at a given time;
5. Update the time by adding a time step and repeat 1, 2, 3, and 4 until a desired ultimate drainage time is reached.

In order to estimate gas concentration in each element, it is necessary to solve the diffusion equation (Fick's second law). Different analytical solutions to the diffusion equation are available from literature such as Crank[128] and Carslaw and Jaeger[129]. It is not clear which of the solutions is more suitable for analyzing gas diffusion into reservoir matrix. To avoid difficulties involved in programming these solutions, a simple numerical solution to the diffusion equation is used in this study. It has been found that the numerical result matches the analytical solution given by Crank[128] when the time step is less than 0.5 day for $D_0 = 1 \times 10^{-7}$ cm^2/s. This comparison is shown in Fig.81. Numerical procedures for the solution are detailed in Appendix B.

Comparisons

Equilibrium Gravity Drainage

The new mathematical model is derived assuming constant capillary pressure at the demarcator, i.e., the wetting phase and non-wetting phase are in thermodynamic equilibrium. This model is compared with existing models and 20 sets of experimental drainage data obtained under thermodynamic equilibrium. In these experiments, IFT varies between 76 and 0.1 dynes/cm, density difference changes from 1.25 to 0.11 g/cc, the effective permeability to wetting phase covers a wide range from 6602 darcies to 6.1 mD, porosity from 42.72% to 18.4%, and connate water saturation from 0 to 15.8 . Fig. 82 shows comparisons of model calculated and observed C_1/C_7 recoveries from a Fontainebleau sandstone core[117]. Other comparisons similar to Fig.82 were previously presented[127] . These comparisons indicate that the new model yields better accuracy than other models. The Cardwell-Parsons-Dykstra model and the Nenniger-Storrow (N-S) model consider a moving demarcator, while the Pavone-Bruzzi-Verre (P-B-V) model and the Luan model assume a fixed demarcator at the bottom of the porous media, which is not a true physical representation of drainage behavior. The C-P-D model neglects an important capillary term that appears in the governing equation. The N-S model is an approximate series solution, and the accuracy depends on number of terms (Nenniger and Storrow[108] provide expressions for only three terms). The P-B-V model was obtained by assuming straight-line relative permeability and logarithmic capillary pressure curve, which also may not be representative of the true behavior. It is believed that these unrealistic assumptions used in model development cause inaccuracies of the models in describing the free-fall gravity drainage process.

Non-equilibrium Gravity Drainage

The concentration of CO_2 in the simulated fracture (annular space around core sample) is estimated based on an Equation of State (EOS):

$$c_f = \frac{p}{RzT} \tag{24}$$

The CO_2 concentration in each matrix element is obtained by multiplying c_f by dimensionless concentration calculated from the numerical solution to the diffusion equation presented in Appendix B. Then EOS was used again to determine volume of CO_2 in each element. Oil production due to horizontal diffusion was assumed to be equal to volume of CO_2 that had diffused into the rock.

Taking the viscosity and density data provided by Lansangan and Smith for CO_2/West Texas oil as a reference, we used the following correlations for CO_2/Spraberry stock tank oil:

$$\mu = 5.0 - 4.8 z_{co_2} \tag{25}$$

and

$$\Delta\rho = \left[\ 0.1873\log_{10}(\mu) + 0.88689\ \right](1.0 - z_{co_2}) \tag{26}$$

Although the IFT of oil/ CO_2 mixtures can be calculated using the parachor method and an EOS, they are not calculated in this way because of difficulties of convergence in flash calculations for the stock tank oil and CO_2 mixtures near MMP conditions. The following empirical correlation was utilized for estimating IFT of the mixtures at the experimental conditions:

$$\sigma = 0.18(1.0 - 0.5z_{co_2}) \tag{27}$$

Capillary pressure threshold was calculated using

$$H = \frac{0.2\sigma}{\Delta\rho g}\sqrt{\frac{\phi}{k_e}} \tag{28}$$

The equivalent diffusion coefficient in the porous media is estimated by

$$D = \frac{D_0}{F\phi} \tag{29}$$

where F is the formation factor.

Figure 83 demonstrates the comparison of our experiment #1 data with a recovery curve calculated by the mathematical model. In the model calculations, molecular diffusion coefficient for CO_2 in oil was tuned to be $6\text{x}10^{-7}$ cm^2/s.

Figure 84 demonstrates the comparison of our experiment #2 data recovery curve calculated by the mathematical model. The same molecular diffusion coefficient for CO_2 in oil was used.

Discussion

Figure 85 presents the calculated oil recovery components due to horizontal diffusion and vertical gravity drainage for experiment 1. Calculations indicate that gravity drainage dominates the recovery mechanism in high permeability reservoirs. Figure 86 demonstrates the calculated oil recovery components due to horizontal diffusion, vertical gravity drainage, and gas expansion for experiment 2. Calculations for experimental 2 indicates that molecular diffusion dominates recovery mechanism in low permeability reservoirs. These observations are not very conclusive because of so many tuned parameters, such as IFT, D_0, and S_{or} , in achieving a history match, but they are consistent with colors and compositions of produced oils from the two cores. However, more investigations are necessary to determine unknown parameters and verify the model proposed in this work.

Summary

1. A literature survey reveals that four mathematical models have been developed by previous investigators for describing free-fall gravity drainage of equilibrium fluid in porous media. Comparison of wetting phase recoveries calculated by these models with experimental data indicates a high degree of inaccuracy. Discrepancies are believed to be due to unrealistic assumptions made in formulation of these models.

2. Based on Darcy's law and film flow theory, a new mathematical model has been developed to describe free-fall gravity drainage with equilibrium fluids. Comparison of wetting phase recoveries given by the new model with 20 sets of experimental data obtained under thermodynamic equilibrium shows better accuracy of the model over existing models.

3. The diffusion equation has been solved numerically to estimate gas concentration in the porous media. A procedure has been developed to couple equilibrium gravity drainage with diffusion in order to describe non-equilibrium gravity drainage. Using this procedure and empirical correlations for fluid properties experimental data obtained under thermodynamic non-equilibrium conditions has been matched.

4. In order to estimate efficiency of gravity drainage in naturally fractured reservoirs, model analysis should be performed using reservoir geometry and conditions.

NOMENCLATURE

a	= inclination angle, degree
A	= cross sectional area, L^2, cm^2
A_i	= coefficient of term $C_{D_{i-1}}^{n+1}$ for grid i
b	= total breadth of film, L, cm.
B_i	= coefficient of term $C_{D_{i-1}}^{n+1}$ for grid block i
c	= concentration, mole/L^3, mole/cm^3
C_D	= dimensionless concentration
c_f	= fracture concentration, mol/L^3, mole/cm^3
c_i	= initial concentration, mole/L^3, mole/cm^3
C_i	= coefficient of term $C_{D_{i-1}}^{n+1}$ for grid i
C_s	= surfactant concentration ppm
D	= effective diffusion coefficient, L^2/t, cm^2/s
D_e	= pendant drop diameter at equator, cm
D_i	= coefficient for grid block i
D_s	= pendant drop diameter at elevation D_e, cm
D_0	= molecular diffusion coefficient, L^2/t, cm^2/s
F	= formation factor, dimensionless
F_s	= correction factor to Kozeny equation
g	= gravitational acceleration, L/t^2
H	= capillary pressure threshold, L, cm
H_D	= dimensionless caillary pressure threshold
H_d	= height of demarcator, L, cm
H_{dD}	= dimensionless height of demarcator
H_e	= elevation of the equator from apex, cm
i	= space index of grid block
k_e	= effective permeability, L^2, md
L	= length of porous medium column, L, cm
m	= the maximum number of grid blocks
M_{CO2+BR}	= total mobility of CO_2 /brine
M_{CO2+SS}	= total mobility of CO_2 /surfactant
M_g	= gas mobility
M_{w2}	= water mobility
n	= time step index
p	= pressure, m/Lt^2, atm
Δp	= pressure drop across a core
P_{ai}	= inner phase pressure above apex, dyne/cm^2
P_{ao}	= outer phase pressure below apex, dyne/cm^2
P_{ca}	= capillary pressure at the apex, dyne/cm^2
P_{He}	= inner phase pressure at H_e, dyne/cm^2
P_o	= outer phase pressure at elevation y, cm
Q	= flow rate

R	= dimensionless fluid recovery
R_a	= radius of curvature at the apex, cm
R_F	= resistance factor
S	= arc length from the apex to elevation y, cm
S_g	= gas saturation
S_o	= oil saturation
S_{wc}	= connate wetting phase saturation, fraction
S_{wi}	= water saturation
S_{wr}	= residual wetting phase saturation, fraction
T	= temperature, °K
t	= time, s
t_D	= dimensionless time
t_c	= critical temperature, °K
Δt	= time step size, s
v_s	= Darcy velocity in saturated zone, L/t, cm/s
V	= convection coefficient, L/t cm/s
V_f	= phase volume in the film, L^3, cm^3
V_r	= residual phase volume, L^3, cm^3
V_s	= phase volume in saturated zone, L^3, cm^3
V_t	= total phase volume, L^3, cm^3
V_{ti}	= initial total phase volume, L^3, cm^3
V_{us}	= phase volume in unsaturated zone, L^3, cm^3
W	= drop weight, dyne
x	= radial distance, cm
x_{max}	= maximum diffusion distance, L, cm
Δx	= length of grid block, L, cm
y	= elevation from apex, cm
z	= depth from the top of the core, L, cm
z_d	= demarcator depth, L, cm
z_D	= dimensionless demarcator depth
z_{CO2}	= mole fraction of CO_2
β	= $\Delta\rho\ g\ R^2_a / \sigma$, dimensionless
$\Delta\rho$	= $\rho_i - \rho_o$, g/cm^3
χ	= mobility
δ	= solubility parameter
μ	= viscosity, m/Lt, cp
ρ_i	= density of the inner phase, g/cm^3
ρ_o	= density of the outer phase, g/cm^3
σ	= interfacial tension, m/t^2, dyne/cm
ϕ	= porosity
lim	= limiting values of the associated variable

REFERENCES

1. S.H. Yang, and R.L. Reed, *Mobility Control Using CO_2 Foams,* paper SPE 19689 presented at the 64th Annual Technical Conference, San Antonio, Oct. 8-11, 1989.
2. H.O. Lee, J.P. Heller, and A.M.W. Hoefer, Change in Apparent Viscosity of CO_2 Foam with Rock Permeability, *SPERE*, (Nov. 1991) 421-428.
3. J.S. Tsau, and J.P. Heller, *Evaluation of Surfactants for CO_2-Foam Mobility Control*, paper SPE 24013 presented at the 1992 Permian Basin Oil and Gas Recovery Conference, Midland, March 18-20, 1992.
4. J.S. Tsau, J.P. Heller, A. Moradi-Araghi, D.R. Zornes, and D.L. Kuehne, *CO_2 Foam Field Verification Pilot Test at EVGSAU: Phase IIIA-Surfactant Performance Characterization and Quality Assurance*, paper SPE 27785 presented at SPE/DOE Ninth Symposium on Improved Oil Recovery, Tulsa, Apr. 17-20, 1994.
5. A. Dixit, J.S. Tsau, and J.P. Heller, *Laboratory Study on Surfactant-Based Selective Mobility Control*, paper SPE 27729 presented at the 1994 Permian Basin Oil and Gas Recovery Conference, Midland, March 16-18, 1994.
6. H. Yaghoobi, and J.P. Heller, *Laboratory Investigation of Parameters Affecting CO_2-Foam Mobility in Sandstone at Reservoir Conditions*, paper SPE 29168 presented at the 1994 SPE Eastern Regional Meeting, Charleston, Nov. 8-10, 1994.
7. J.S. Tsau, and J.P. Heller, *How Can Selective Mobility Reduction of CO_2-Foam Assist in Reservoir Floods?*, paper SPE 35168 presented at the 1996 Permian Basin Oil and Gas Recovery Conference, Midland, March 27-29, 1996.
8. H. Yaghoobi, and J.P. Heller, *CO_2-Foam Mobility Behavior in Heterogeneous System*, paper SPE 35169 presented at the 1996 Permian Basin Oil and Gas Recovery Conference, Midland, March 27-29, 1996.
9. H. Yaghoobi, J.S. Tsau, and J.P. Heller, *Improving CO_2 Floods in Heterogeneous Media*, paper SPE 35403 presented at SPE/DOE Tenth Symposium on Improved Oil Recovery, Tulsa, Apr. 21-24, 1996.
10. L. Lake, *Enhanced Oil Recovery*, Prentice Hall, Inc., Englewood Cliffs, New Jersey, 1989, 201-205.
11. J.R. Ammer, A.C. Brummert, and W.N. Sams, Miscible Applied Simulation Techniques for Energy Recovery-Version 2.0, *User's Guide and Technical Report*, DOE Contract No. DOE/BC-91/2/SP February 1991.
12. S.H. Chang, and R.B. Grigg, *Foam Displacement Modeling in CO_2 Flooding Precesses*, paper SPE 35401 presented at SPE/DOE Tenth Symposium on Improved Oil Recovery, Tulsa, Apr. 21-24, 1996.
13. F.D. Martin *Enhanced Oil Recovery for the Independent Producer*, paper SPE/DOE 24142 presented at the 8th Symposium on Enhanced Oil Recovery, Tulsa, April 22-24, 1992.
14. R.E. Hadlow, *Update of Industry Experience with CO_2 Flooding*, paper SPE 24928 presented at the 67th SPE Annual Technical Conference and Exhibition, Washington, D.C., October 4-7, 1992.
15. J-G.J. Shyeh-Yung, *Mechanisms of Miscible Oil Recovery: Effects of Pressure on Miscible and Near-Miscible Displacements of Oil by Carbon Dioxide*, paper SPE 22651 presented at the 1991 SPE Annual Technical Conference and Exhibition, Dallas, October 6-9.
16. J-G. J Shyeh-Yung, *et al.*, *Effect of Solvent Composition and Pressure on Displacement of Oil by Enriched Hydrocarbon Gases*, paper SPE 28264 presented at the 1994 SPE Annual Technical Conference & Exhibition, New Orleans, Sept. 25-28.
17. J.E. Burger, *et al*, Effect of Phase Behavior on Bypassing in Enriched Gasfloods, *SPERE* (May 1994) 112.

18. C. Bardon, *et al*, *Gas/Oil Relative Permeabilities and Residual Oil Saturations in a Field Case of a Very Light oil, in the Near-Miscibility Conditions*, paper SPE 28625 presented at the 1994 SPE Annual Technical Conference & Exhibition, New Orleans, Sept. 25-28.
19. K.K. Pande, *Effect of Gravity and Viscous Crossflow on Hydrocarbon Miscible Flood Performance in Heterogeneous Reservoirs*, paper SPE 24935 presented at the 67th SPE Annual Technical Conference and Exhibition, Washington, D.C., October 4-7, 1992.
20. G.J. Mizenko, *North Cross (Devonian) Unit CO_2 Flood: Status Report*, paper SPE/DOE 24210 presented at the 1992 SPE/DOE Symposium on Enhanced Oil Recovery, Tulsa, April 22-24.
21. E.C. Liu, *et al.*, *A Numerical Evaluation of the Effectiveness of Single Slug, WAG, and Hybrid CO_2 Injection Processes for the Dollarhide Devonian Unit, Andrew County, Texas*, paper SPE 20098 presented at the 1990 Permian Basin Oil and Gas Recovery Conference, Midland, March 8-9.
22. M.B. Vargaftik, *Tables on the Thermophysical Properties of Liquids and Gases*, Hemisphere Publishing Corp., Washington, D.C., 1975.
23. J.F. Ely, *et al.*, *NIST Thermophysical Properties of Hydrocarbon Mixtures Databases*, Version 1.0 National Institute of Standards and Technology, Standard Reference Data Program (1990).
24. W.F. Yellig, *et al.*, Determination and Prediction of CO_2 Minimum Miscibility Pressure, *JPT* (Jan. 1980) 160.
25. J.L. Creek, and J.M. Sheffield, Phase Behavior, Fluid Properties, and Displacement Characteristics of Permian Basin Reservoir Fluid.CO_2 Systems, *SPERE* (Feb. 1993) 34-42.
26. S-H. Chang, F.D. Martin, and R.B. Grigg, *Effect of Pressure on CO_2 Foam Displacement: A Micromodel Visualization Study*, paper 27784 presented at the 1994 SPE/DOE Ninth Symposium on Improved Oil Recovery, Tulsa, April 17-20.
27. R.B. Grigg, M.D. Gregory, and J.D. Purkaple, *The Effect of Pressure on Improved Oilflood Recovery from Tertiary Gas Injection*, paper 35426 presented at the 1996 SPE/DOE Tenth Symposium on Improved Oil Recovery, Tulsa, April 21-24.
28. L.W. Holm, *et al.*, Mechanisms of Oil Displacement by Carbon Dioxide, *JPT* (Dec. 1974) 1427.
29. R.A. Harmon, and R.B. Grigg, Vapor-Density Measurements for Estimating Minimum Miscibility Pressure, *SPERE* (Nov. 1988) 1215.
30. F.M. Orr, Jr., *et al.*, Interpretation of Pressure-Composition Phase Diagrams for CO_2/Crude-Oil Systems, *SPEJ* (Feb. 1984) 485.
31. L.W. Holm, *et al.*, Effect of Oil Composition on Miscible Type Displacement by Carbon Dioxide, *SPEJ* (Feb. 1982) 87.
32. F.M. Orr, Jr., *et al.*, Effect of Oil Composition on Minimum Miscibility - Part 2: Correlation, *SPERE* (Nov. 1987) 479.
33. K.D. Hagedorn, and F.M. Orr, Jr., *Component Partitioning in CO_2/Crude Oil Systems: Effects of Oil Composition on CO_2 Displacement Performance*, paper SPE 25169, presented at the SPE International Symposium on Oilfield Chemistry, New Orleans, March 2-5, 1993.
34. J.M. Prausnitz, *Molecular Thermodynamics of Fluid-Phase Equilibria*, Prentice-Hall, Englewood Cliffs (1969).
35. E.A. Lange, *Correlation and Prediction of Residual Oil Saturation for Gas Injection EOR Processes*, paper 35425 presented at the 1996 SPE/DOE Tenth Symposium on Improved Oil Recovery, Tulsa, April 21-24.
36. F.B. Thomas, *et al.*, *Miscible or Near-Miscible Gas Injection, Which Is Better?*, paper SPE/DOE 27811 presented at the 1994 SPE/DOE Ninth Symposium on Improved Oil Recovery, Tulsa, April 17-20.
37. D.S. Schechter, and B. Guo, *Parachors Based on Modern Physics and Their Uses in IFT Prediction of Reservoir Fluids*, paper SPE 30785 presented at the SPE Annual Technical Conference & Exhibition, Dallas, October 22-25, 1995.

38. R.S. Wu, *et al.*, Evaluation of Miscibility From Slim Tube Tests, *J. Canadian Pet. Tech.*, (Nov-Dec 1990) 63.
39. R.B. Grigg, J.P. Heller, and D.S. Schechter, Improved Efficiency of Miscible CO_2 Floods and Enhanced Prospects for CO_2 Flooding Heterogeneous Reservoirs, *Annual Report*, DOE Contract No. DE-FG22-94BC14977, April 1995.
40. J.E. Stevens, and F.D. Martin, *CO_2 Foam Field Verification Pilot Test at EVGSAU: Phase IIIB - Project Operations and Performance Review*, paper SPE/DOE 27786 presented at the 1994 SPE/DOE Ninth Symposium on Improved Oil Recovery, Tulsa, April 17-20.
41. S-H. Chang, and R.B. Grigg, *Laboratory Flow Tests Used to Determine Reservoir Simulator Foam Parameters for EVGSAU CO_2 Foam Pilot*, paper SPE 27675 presented at the 1994 Permian Basin Oil and Gas Recovery Conference, Midland, March 16-18.
42. F.D. Martin, *et al.*, Field Verification of CO_2 Foam, *Final Report,* DOE Contract No. DE-FG21-89MC26031, April 1995.
43. F.M. Orr, Jr., and C.L. Lien, Phase Behavior of CO_2 and Crude Oil in Low Temperature Reservoirs, *SPEJ* (Aug. 1981) 480-492.
44. R.M. Lansangan, and J.L. Smith, Viscosity, Density, and Composition Measurements of CO_2/West Texas Oil Systems, *SPERE* (Aug. 1993) 175-182.
45. R.B. Grigg, *Dynamic Phase Composition, Density, and Viscosity Measurements During CO_2 Displacement of Reservoir Oil*, paper SPE 28974 presented at the SPE International Symposium on Oilfield Chemistry held in San Antonio, 14-17 February 1995.
46. D.L. Kuehne, *et al.*, *Evaluation of Surfactant for the CO_2 Mobility Control in Dolomite Reservoirs*, paper SPE/DOE 24177 presented at the SPE/DOE Eighth Symposium on Enhanced Oil Recovery, Tulsa, OK, April 22-24, 1992.
47. A.R. Kovscek, and C.J. Radke, *A Comprehensive Description of Transient Foam Flow in Porous Media*, paper presented at the DOE/NIPER Symposium on Field Application of Foams for Oil Production, Bakersfield, CA, February 11-12, 1993.
48. A.H. Falls, G.J. Hirasaki, T.W. Patzek, D.A. Gauglitz, D.D. Miller, and T. Ratulowski, Development of a Mechanistic Foam Simulator: The Population Balance and Generation by Snap-Off, *SPERE* (Aug. 1988) 884-892.
49. C.H. Marfoe, H. Kazemi, and W.F. Ramirez, *Numerical Simulation of Foam Flow in Porous Media,* paper SPE 16709 presented at the 62th Annual Technical Conference and Exhibition, Dallas, TX, Sept. 27-30, 1987.
50. M.R. Islam, and S.M. Farouq Ali, Numerical Simulation of Foam Flow in Porous Media, *J. Can. Pet. Tech.* (July-Aug. 1990) 29, No. 4, 47-51.
51. A.W. Fisher, R.W.S. Foulser, and S.G. Goodyear, *Mathematical Modeling of Foam Flooding*, SPE/DOE 20195 presented at the SPE/DOE Seventh Symposium on Enhanced Oil Recovery, Tulsa, OK, April 22-25, 1990.
52. D. H-S Law, Z-M Yang, and T.W. Stone, Effect of the Presence of Oil on Foam Performance: A Field Simulation Study, *SPERE* (May 1992) 228-236.
53. S.S. Mohammadi, D.A. Coombe, and V.M. Stevenson, Test of Steam-Foam Process for Mobility Control in South Casper Creek Reservoir, *J. Can. Pet. Tech.* (Dec. 1993) 32, No. 10, 49-54.
54. G.J. Hirasaki, and L.B. Lawson, Mechanisms of Foam Flow in Porous Media: Apparent Viscosity in Smooth Capillaries, *SPEJ* (April 1985) 176-190.
55. S-H Chang, L.A. Owusu, S.B. French, and F.S. Kovarik, *The Effect of Microscopic Heterogeneity on CO_2-Foam Mobility: Part 2—Mechanistic Foam Simulation*, paper SPE/DOE 20191 presented at the SPE/DOE Seventh Symposium on Enhanced Oil Recovery, Tulsa, OK, April 22-25, 1990.
56. F. Friedmann, W.H. Chen, and P.A. Gauglitz, Experimental and Simulation Study of High-Temperature Foam Displacement in Porous Media, *SPERE* (Feb. 1991) 37-45.

57. R.A. Ettinger, and C.J. Radke, Influence of Texture on Steady Foam Flow in Berea Sandstone, *SPERE* (Feb. 1992) 83-90.
58. A.R. Kovscek, T.W. Patzek, and C.J. Radke, *Simulation of Foam Transport in Porous Media*, paper SPE 26402 presented at the 68th Annual Technical Conference and Exhibition, Houston, TX, Oct. 3-6, 1993.
59. A.R. Kovscek, T.W. Patzek, and C.J. Radke, *Mechanistic Prediction of Foam Displacement in Multidimensions: A Population Balance Approach*, paper SPE/DOE 27789 presented at the SPE/DOE Ninth Symposium on Improved Oil Recovery, Tulsa, OK, April 17-20, 1994.
60 T.W. Patzek, Description of Foam Flow in Porous Media by the Population Balance Method, *Surfactant-Based Mobility Control: Progress in Miscible-Flood Enhanced Oil Recovery*, D.H. Smith (ed.), ACS Symposium Series 373, Washington, D.C. (1988).
61. W.R. Rossen, Z.H. Zhou, and C.K. Mamun, *Modeling Foam Mobility at the 'Limiting Capillary Pressure'*, paper SPE 22627 presented at the 66th Annual Technical Conference and Exhibition, Dallas, TX, Oct. 6-9, 1991.
62. W.R. Rossen, S.C. Zeilinger, J-X. Shi, and M.T. Lim, *Mechanistic Simulation of Foam Processes in Porous Media*, paper SPE 28940 presented at the 69th Annual Technical Conference and Exhibition, New Orleans, LA, Sept. 26-28, 1994.
63. J.R. Ammer, A.C. Brummert, and W.N. Sams, Miscible Applied Simulation Techniques for Energy Recovery -- Version 2.0, *Quarterly Report,* DOE Contract No. DOE/BC-91/2/SP (February 1991).
64. Y. Chang, *Development and Application of an Equation of State Compositional Simulator*, Ph.D. dissertation, University of Texas, Austin, Texas, 1990.
65. Y. Chang, G.A. Pope, and K. Sepehrnoori, A Higher-Order Finite Difference Compositional Simulator, *J. Pet. Sci. Eng.* (Nov. 1990) 5, No. 1, 35-50.
66. M.T. Lim, S.A. Khan, K. Sepehrnoori, and G.A. Pope, *Simulation of Carbon Dioxide Flooding Using Horizontal Wells*, paper SPE 24929 presented at the 67th Annual Technical Conference and Exhibition, Washington, D.C., Oct. 4-7, 1992.
67. F.D. Martin, J.E. Stevens, and K.J. Harpole, CO_2-Foam Field Test at the East Vacuum Grayburg/San Andres Unit, *SPERE* (Nov. 1995) 266-272.
68. J.E. Killough, and C.A. Kossack, *Fifth Comparative Solution Project: Evaluation of Miscible Flood Simulators*, paper SPE 16000 presented at the 9th Symposium on Reservoir Simulation, San Antonio, TX, Feb. 1-4, 1987.
69. S.D. Joshi, *Horizontal Well Technology*, PennWell, Tulsa, OK, 1991.
70. J.J. Taber, and R.S. Seright, *Horizontal Injection and Production Wells for EOR or Waterflooding*, paper SPE 23952 presented at the SPE Permian Basin Oil and Gas Recovery Conference, Midland, TX, March 18-20, 1992.
71. Hallenbeck *et al.*, *Innovative Approach to CO_2 Project Development Holds Promise for Improving CO_2 Flood Economics in Smaller Fields Nearing Abandonment*, paper SPE 28334 presented at the SPE 69th Annual Technical Conference and Exhibition, New Orleans, LA, Sept. 25-28, 1994.
72. A.B. Speirs, and P.B. Warren, *Horizontal Well Experience in California Thermal Reservoirs*, paper HWC94-56 presented at the Canadian SPE/CIM/CANMET International Conference on Recent Advances in Horizontal Well Applications, Calgary, Canada, March 20-23, 1994.
73. N. Mungan, *Further Recovery from Mature Reservoirs with Horizontal Wells*, paper HWC94-07 Keynote Address presented at the Canadian SPE/CIM/CANMET International Conference on Recent Advances in Horizontal Well Applications, Calgary, Canada, March 20-23, 1994.
74. Dakhlia *et al.*, *Simulation of Surfactant Flooding Using Horizontal Wells*, paper 95-82 presented at the 46th Annual Technical Meeting of The Petroleum Society of CIM, Banff, Alberta, Canada, May 14-17, 1995.

75. Babu *et al.*, The Relation Between Wellblock and Wellbore Pressures in Numerical Simulation of Horizontal Wells, *SPERE* (August 1991), 324-328.
76. Nghiem *et al.*, *Seventh SPE Comparative Solution Project: Modeling of Horizontal Wells in Reservoir Simulation*, paper SPE 21221 presented at the 11th SPE Symposium on Reservoir Simulation, Anaheim, CA, Feb. 17-20, 1991.
77. O.R. Wagner, and R.O. Leach, *Effect of Interfacial Tension on Displacement Efficiency*, SPE Journal , December, 1966, 335-344.
78. P.L. de No *J. Gen. Physiol.*, 1 (1919) 521; 5 (1923) 429.
79. L. Wilhelmy,, *Ann. Phys.*, 119 (1863) 177.
80. S.J. Sudgen, *J. Chem. Soc.*, (1921) 1483.
81. S.J. Sudgen, *J. Chem. Soc.*, (1922) 858.
82. W.D. Harkins, and F.E. Brown, *J. Amer. Chem. Soc.*, 41 (1919) 499.
83. B. Vonnegut, *Rev. Sci. Instrum.*, 13 (1942) 6.
84. M.S. Hannif, and A.D. Pearce, *Measuring Interfacial Tensions in a Gas-Condensate System With a Laser-Light-Scattering Technique*, SPE Reservoir Engineering , (November 1990) 589-594.
85. J.M. Andreas, E.A. Hauser, and W.B. Trucker, Boundary Tension by Pendant Drops, *J. Phys. Chem.*, 42 (1938) 1001-1019.
86. S. Fordham, On the Calculation of Surface Tension from Measurements of Pendant Drops, *Proc. R. Soc.* A194 (1948) 1.
87. H.H. Girault, D.J. Schiffrin, and B.D.V. Smith, Drop Image Processing for Surface Tension and Interfacial Tension Measurements, *J. Electoanalytical Chemistry*, 137 (1982) 207-217.
88. F.K. Hansen, and G. Rodsrud, Surface Tension by Pendant Drop, *J. Colloid Interfacial Science*, 141 (1991) 1-9.
89. R.J. Huygens, H. Ronde, and J. Hagoort, *Pendant Drop Interfacial Tension Measurements Using Image Processing Techniques*, paper presented at the 6th European IOR-Symposium in Stavanger, Norway, May 21-23, 1991.
90. C.E. Stauffer, *J. Phys. Chem.*,69 (1965) 1933.
91. H.H. Girault, D.J. Schiffrin, and B.D.V. Smith, The Measurement of Interfacial Tension of Pendant Drops Using a Video Image Profile Digitizer, *J. Colloid Interfacial Science*, 101, No. 1, September 1984.
92. J.W. Jennings, and N.R. Pallas, An Efficient Method for the Determination of Interfacial Tension from Drop Profiles, *Langmuir*, 4 (1988) 959-967.
93. Y. Rotenberg, L. Boruvka, and A.W. Newmann, Determination of Surface Tension and Contact Angle from the shapes of Axisymmetric Fluid Interfaces, *J. Colloid Interfacial Science,* 93, No. 1 (1983), 169-183.
94. N.R. Pallas, and Y. Harrison, An Automated Drop Shape Apparatus and Surface Tension of Pure Water, *J. Colloid Surfaces*, 43, (1990) 169-195.
95. A.L. Lopez de Ramos, *Capillary-Enhanced Diffusion of CO_2 in Porous Media*, Ph.D. thesis, University of Tulsa, Tulsa, Oklahoma, 1993.
96. C.A. MacLeod, and C.J. Radke, A Growing-Drop Technique for Measuring Dynamic Interfacial Tension, *Topical report,* DOE/BC/94000102, 1993.
97. C. Huh, and R.L. Reed, A Method for Estimating Interfacial Tensions and Contact Angles from Sessile and Pendant Drop Shapes, *J. Colloid Interfacial Science*, 91, No. 2 (February 1983), 472-484.
98. J. Jasper, The Surface Tension of Pure Liquid Compounds, *J. Phys. Chem. Ref. Data*, 1, 1971, 841-1009.
99. D. Beliveau, D.A. Payne, and M. Mundry, Waterflood and Flood of the Fractured Midale Field, *Journal of Petroleum Engineering*, September 1993, 881.

100. F.H. King, Principles and Conditions of the Movements of Ground Water, *Annual Report*, USGS (1899), 19.
101. M.C. Leverett, Capillary Behavior in Porous Solids, *Trans. AIME* (1941), 142 , 152.
102. D.L. Katz, Possibilities of Secondary Recovery for the Oklahoma City Wilcox Sand, *Trans. AIME* (1942), 146 , 28.
103. R.F. Stahl, W.A. Martin, and R.L. Huntington, Gravitational Drainage of Liquids from Unconsolidated Wilcox Sand, *Petroleum Technology*, January 1943.
104. L.F. Elkins, R.W. French, and W.E. Glenn, Lance Creek Sundance Reservoir Performance — a Unitized Pressure-maintenance Project, *Petroleum Technology*, July 1948.
105. W.T. Cardwell, and R.L. Parsons, Gravity Drainage Theory, *Trans. AIME* (1949), 179 , 199.
106. P.L. Terwilliger, L.E. Wilsey, H.N. Hall, P.M. Bridges, and R.A. Morse, An Experimental and Theoretical Investigation of Gravity Drainage Performance, *Petroleum Transactions*, AIME (1951), 192 .
107. S.E. Buckley, and M.C. Leverett, Mechanism of Fluid Displacement in Sands, *Trans. AIME* (1942), 146 , 107.
108. E. Nenniger, and J.A. Storrow, Drainage of Packed Beads in Gravitational and Centrifugal-force Fields, *AIChE* (1958), 4 , No. 3, 305.
109. P.L. Essley, G.L. Hancock, and K.E. Jones, *Gravity Drainage Concepts in a Steeply Dipping Reservoir*, paper SPE 1029-G, 1958.
110. E.E. Templeton, and R.E. Nielsen, *A Study of Gravity Counterflow Segregation*, SPE Journal , June 1962.
111. J.M. Dumore, and R.S. Schols, *Drainage Capillary - Pressure Functions and the Influence of Connate Water*, SPE Journal , October 1974.
112. H. Dykstra, The Prediction of Oil Recovery by Gravity Drainage, *Journal of Petroleum Technology*, May 1978.
113. J. Hagoort, Oil Recovery by Gravity Drainage, *SPE Journal*, June 1980.
114. H.H. Haldorsen, C.A. Rego, D.M. Chang, H.J. Mayson, and D.M. Creveling, Jr., *An Evaluation of the Prudhoe Bay Gravity Drainage Mechanism by Complementary Techniques*, paper SPE 13651, presented at the SPE California Regional Meeting, held in Bakersfield, California, March 27-29, 1985.
115. A. Nectoux, *Equilibrium Gas Oil Drainage: Velocity, Gravitational and Compositional Effects*, paper presented at the 4th European Symposium on Enhanced Oil Recovery, held October 27-29, 1987 in Hamburg, 779.
116. Ch. Jacquin, B. Legait, J.M. Martin, A. Nectoux, F. Anterion, and M. Rioche, Gravity Drainage in a Fissured Reservoir with Fluids not in Equilibrium, *Journal of Petroleum Science and Engineering* (1989), 2 , 217.
117. D. Pavone, P. Bruzzi, and R. Verre, *Gravity Drainage at Low Interfacial Tension*, paper presented at the 5th European Symposium on Enhanced Oil Recovery, held October 27-29, 1989 in Budapest, 165.
118. J.A. Stensen, A. Skange, P. Monstad, and A. Graue, *The Effect of Interfacial Tension on Gas Gravity Drainage*, paper presented at the 2nd North Sea Chalk Symposium, held June 11-12, 1990 in Copenhagen, Denmark.
119. E.E. Suffridge, and T.A. Renner, *Diffusion and Gravity Drainage Tests to Support the Development of a Dual Porosity Simulator*, paper presented at the 6th European IOR-Symposium, held May 21-23, 1991 in Stavanger, Norway.
120. F.V. da Vilva, and B. Meyer, *Improved Formulation for Gravity Segregation in Naturally Fractured Reservoirs*, paper presented at the 6th European IOR-Symposium, held May 21-23, 1991 in Stavanger, Norway.

121. D.S. Schechter, D. Zhou, and F.M. Orr, Jr., Low IFT Gravity Drainage and Imbibition, *Journal of Petroleum Science and Engineering* (November 1994), 283.
122. Z. Luan, *Some Theoretical Aspects of Gravity Drainage in Naturally Fractured Reservoirs*, paper SPE 28641, presented at the 69th Annual Technical Conference and Exhibition of SPE, held September 25-28, 1994 in New Orleans, Louisiana.
123. A.A. Espie, C.E. Brown, K.R. Narayanan, and T.C. Wilcox, *A Laboratory Investigation of Gravity Drainage/Waterflood Interaction in Prudhoe Bay*, paper SPE 28614, presented at the 69th Annual Technical Conference and Exhibition of SPE, held September 25-28, 1994 in New Orleans, Louisiana.
124. L.J.J. Catalan, F.A.L. Dullien, and I. Chatzis, The Effects of Wettability and Heterogeneities on the Recovery of Waterflood Residual Oil with Low Pressure Inert Gas Injection Assisted by Gravity Drainage, *SPE Advanced Technology Series*, 2 , No. 2, 1994.
125. M. Blunt, D. Zhou, and D. Fenwick, *Three Phase Flow and Gravity Drainage in Porous Media*, paper submitted to Transport in Porous Media for publication, May 1994.
126. L. Øyno, K. Uleberg, and C.H. Whitson, *Dry Gas Injection Fractured Chalk Reservoirs -- An Experimental Approach*, paper SCA 9527 presented at the 1995 SCA Conference, San Francisco, California, August 20-22, 1995.
127. B. Guo, Modeling of Gravity Drainage Under Constant and Varying Capillary Pressure, *Natural Fractured Reservoir Forum Proceedings*, paper PRRC 95-40, New Mexico Institute of Mining and Technology, March 2, 1995.
128. J. Crank, *The Mathematics of Diffusion*, second edition, Oxford University Press, New York City (1975).
129. H.S. Carslaw, and J.C. Jaeger, *Conduction of Heat in Solids*, second edition, Oxford University Press, New York City (1959).
130. H. Jeffreys, *Proc. Cambridge Phil. Soc.*, 26 , 204 (1930).

Appendix A. Formulation of Free-fall Gravity Drainage

Assumptions

The following assumptions are made in this analysis:

1. The porous medium is homogeneous and isotropic
2. Draining phase flows only in the vertical direction.
3. The draining phase is incompressible.
4. Capillary pressure is constant at the moving demarcator.

Governing Equation

The total volume of draining phase (V_t) in the porous medium consists of phase volume in the saturated zone (full pore drainage zone) and phase volume in the unsaturated zone (above phase demarcator). That is

$$V_t = V_s + V_{us} \qquad \text{A-1}$$

The phase volume in the unsaturated zone (V_{us}) includes residual phase volume (V_r) and phase volume in the film (V_f):

$$V_{us} = V_r + V_f \qquad \text{A-2}$$

If the initial and residual saturations of the draining phase are S_{wi} and S_{wr}, respectively, we have

$$V_s = S_{wi}\phi A(L - z_d) \qquad \text{A-3}$$

and

$$V_r = S_{wr}\phi A z_d \qquad \text{A-4}$$

According to Nenniger and Storrow[108], the phase volume in the film can be estimated by integrating Jeffreys[130] equation:

$$V_f = \frac{2}{3} b \sqrt{\frac{\mu z_d^3}{\Delta\rho g t}} \qquad \text{A-5}$$

Substitutions of Eqs. (A-2) through (A-5) into Eq. (A-1) give

$$V_t = S_{wi}\phi A(L - z_d) + S_{wr}\phi A z_d + \frac{2}{3}b\sqrt{\frac{\mu z_d^3}{\Delta\rho g t}} \qquad \text{A-6}$$

Darcy velocity in the saturated zone can be expressed as

$$v_s = -\frac{1}{A}\frac{dV_t}{dt} \qquad \text{A-7}$$

The volumetric flow rate, dV_t/dt, in Eq. (A-7) can be determined by taking the derivative of Eq. (A-6) with respect to time:

$$\frac{dV_t}{dt} = -S_{wi}\phi A\frac{dz_d}{dt} + S_{wr}\phi A\frac{dz_d}{dt} + b\sqrt{\frac{\mu}{\Delta\rho g}}\left(\sqrt{\frac{z_d}{t}}\frac{dz_d}{dt} - \frac{1}{3}\sqrt{\frac{z_d^3}{t^3}}\right) \qquad \text{A-8}$$

Substituting Eq. (A-8) into Eq. (A-7) yields:

$$v_s = (S_{wi} - S_{wr})\phi\frac{dz_d}{dt} + \frac{b}{A}\sqrt{\frac{\mu}{\Delta\rho g}}\left(\frac{1}{3}\sqrt{\frac{z_d^3}{t^3}} - \sqrt{\frac{z_d}{t}}\frac{dz_d}{dt}\right) \qquad \text{A-9}$$

The Darcy velocity (v_s) can also be expressed using Darcy's law. This was done by Cardwell and Parsons[105]:

$$v_s = \frac{k_e\Delta\rho g}{\mu}\left(1 - \frac{H}{L - z_d}\right) \qquad \text{A-10}$$

Substituting Eq. (A-9) into Eq. (A-10) and rearranging the latter give:

$$\left[(S_{wi} - S_{wr})\phi - \frac{b}{A}\sqrt{\frac{\mu z_d}{\Delta\rho g t}}\right]\frac{dz_d}{dt} + \frac{b}{3A}\sqrt{\frac{\mu z_d^3}{\Delta\rho g t^3}} - \frac{k_e\Delta\rho g}{\mu}\left(1 - \frac{H}{L - z_d}\right) = 0 \qquad \text{A-11}$$

Now let us define the following dimensionless variables:

$$t_D = \frac{k_e \Delta\rho g t}{\mu L} \qquad \text{A-12}$$

$$z_D = \frac{z_d}{L} \qquad \text{A-13}$$

$$H_D = \frac{H}{L} \qquad \text{A-14}$$

and

$$H_{dD} = \frac{H_d}{L} \qquad \text{A-15}$$

Introducing Eqs. (A-12), (A-13) and (A-14) into Eq. (A-11) and rearranging the latter give:

$$\left[\left(S_{wi} - S_{wr}\right)\phi - \frac{b\sqrt{k_e}}{A}\sqrt{\frac{z_d}{t_D}}\right]\frac{dz_D}{dt_D} + \frac{b\sqrt{k_e}\,z_D}{3At_D}\sqrt{\frac{z_D}{t_D}} - \left(1 - \frac{H_D}{1 - z_D}\right) = 0 \qquad \text{A-16}$$

If the breadth of the film, b, is estimated using Kozeny equation, then

$$\frac{b\sqrt{k_e}}{A} = \sqrt{\frac{F_s \phi^3}{5}} \qquad \text{A-17}$$

Substituting Eq. (A-17) into Eq. (A-16) yields:

$$\phi\left[S_{wi} - S_{wr} - \sqrt{\frac{F_s \phi z_D}{5t_D}}\right]\frac{dz_D}{dt_D} + \frac{\phi z_D}{3t_D}\sqrt{\frac{F_s \phi z_D}{5t_D}} - \left(1 - \frac{H_D}{1 - z_D}\right) = 0 \qquad \text{A-18}$$

Eq. (A-18) is the governing equation for demarcator depth z_D.

Solution

Using initial condition at $z_D=0$ at $t_D=0$, Eq. (A-18) is solved numerically. Typical solution curves are presented in Figs. 79 and 80 for $\phi=0.1$, $S_{wr}=0.1$, $H_D=0.1$, and $F_s=1$ and 0.5, respectively.

Based on the position of the demarcator and the volume distribution of the liquid in the porous medium, the draining-phase recovery (R) with time can then be determined as follows:

$$R=\frac{V_{ti}-V_s-V_r-V_f}{V_{ti}} \qquad \text{A-19}$$

The initial phase volume is

$$V_{ti}=S_{wi}\phi AL \qquad \text{A-20}$$

Substituting Eqs. (A-20), (A-3), (A-4), and (A-5) into Eq. (A-19) and rearranging the latter give

$$R=\left(1-\frac{S_{wr}}{S_{wi}}\right)\frac{z_d}{L}-\frac{2b}{3S_{wi}\phi AL}\sqrt{\frac{\mu z_d^3}{\Delta\rho g t}} \qquad \text{A-21}$$

Introducing dimensionless variables and Eq. (A-17) into Eq. (A-21) results in

$$R=\left(1-\frac{S_{wr}}{S_{wi}}\right)z_D-\frac{2z_D}{3S_{wi}}\sqrt{\frac{F_s\phi z_D}{5t_D}} \qquad \text{A-22}$$

Typical recovery curves are also shown in Figs. 79 and 80 corresponding to the demarcator curves presented in the figure.

Appendix B. Numerical Solution of Diffusion Equation

Assumptions

Since the height of the porous medium under consideration is vertically exposed to a diffusing phase, we assume that (1) vertical diffusion is negligible, i.e., horizontal (one-dimensional) diffusion prevails in the porous medium, and (2) diffusion coefficient is constant during gravity drainage throughout the porous medium.

Governing Equation

The governing equation to the 1-D diffusion problem is the Fick's second law:

$$D\frac{\partial^2 c}{\partial x^2} = \frac{\partial c}{\partial t} \qquad \text{B-1}$$

Initial Condition

Initially the concentration of the diffusing phase in the porous medium is assumed to be a constant c_i. The initial condition may be expressed as

$$c|_{t=0,\,x>0} = c_i \qquad \text{B-2}$$

Boundary Conditions

The inner boundary is the lateral surface of the porous medium. The gas concentration at the boundary may be assumed to be the gas concentration in the fracture:

$$c|_{t>0,\,x=0} = c_f \qquad \text{B-3}$$

The outer boundary is at the center of the porous medium. Because of symmetry, the following boundary condition should be used:

$$\left[\frac{\partial c}{\partial x}\right]_{t\geq 0,\,x=x_{\max}} = 0 \qquad \text{B-4}$$

By introducing dimensionless concentration defined as

$$C_D = \frac{c - c_i}{c_f - c_i} \qquad \text{B-5}$$

Eqs. (B-1) through (B-4) can be, respectively, written as

$$D\frac{\partial^2 C_D}{\partial x^2}=\frac{\partial C_D}{\partial t} \qquad \text{B-6}$$

$$C_D|_{t=0,x>0}=0 \qquad \text{B-7}$$

$$C_D|_{t>0,x=0}=1 \qquad \text{B-8}$$

$$\left[\frac{\partial C_D}{\partial x}\right]_{t\geq 0,x=x_{\max}}=0 \qquad \text{B-9}$$

Numerical Solution

Using implicit differentiation scheme, Eq. (B-6) can be discretized at point and time step as:

$$D\left[\frac{C_{D_{i-1}}^{n+1}-2C_{D_i}^{n+1}+C_{D_{i+1}}^{n+1}}{\Delta x^2}\right]=\frac{C_{D_i}^{n+1}-C_{D_i}^{n}}{\Delta t} \qquad \text{B-10}$$

which can be rearranged to be:

$$A_i C_{D_{i-1}}^{n+1}+B_i C_{D_i}^{n+1}+C_i C_{D_{i+1}}^{n+1}=D_i \qquad \text{B-11}$$

where $A_i = C_i = 1$ and

$$B_i=-2-\frac{\Delta x^2}{D\Delta t} \qquad \text{B-12}$$

$$D_i=-\frac{\Delta x^2}{D\Delta t}C_{D_i}^{n} \qquad \text{B-13}$$

For i=1 (first cell), after applying boundary condition given by Eq. (B-8), Eq. (B-11) becomes

$$\left(A_1 + B_1\right)C_{D_1}^{n+1} + C_1 C_{D_2}^{n+1} = D_1 \qquad \text{B-14}$$

For i=2 (second cell), Eq. (B.11) becomes

$$A_2 C_{D_1}^{n+1} + B_2 C_{D_2}^{n+1} + C_2 C_{D_3}^{n+1} = D_2 \qquad \text{B-15}$$

If the length is descretized into m cells, for i=m (last cell), after applying boundary condition given by Eq. (B-9), Eq. (B-11) becomes

$$A_m C_{D_{m-1}}^{n+1} + \left(B_m + C_m\right)C_{D_m}^{n+1} = D_m \qquad \text{B-16}$$

Eqs. (B-14) through (B-16) are m equations with m unknowns $(C_{D_i}^{n+1}, i = 1,2,...,m)$, and can be written in the form of matrices. These unknowns can be easily solved using the matrix solver subroutine THOMAS. The numerical result is comparable to analytical result given by Crank[128] as shown in Fig. 81.

TABLE 1

Sulimar Queen separator oil - CO_2 swelling test @ 70°F

Press. (psig)	Total Vol, cc	Rel. Vol. (1)	Rel. Vol. (2)	Vapor (cc)	% Vol. Vapor	Upper Liq, cc
20.5 MOLE PERCENT CO_2						
1897	27.0	0.982	1.053			
1235	27.2	0.989	1.060			
800	27.3	0.993	1.064			
335	27.4	0.996	1.068			
201	27.5	1.000	1.072	0.0	0.0	
182	32.0	1.164	1.248	3.0	9.4	
168	36.0	1.309	1.404	7.0	19.4	
163	38.0	1.382	1.481	9.0	23.7	
149	43.0	1.564	1.676	13.5	31.4	
40.8 MOLE PERCENT CO_2						
2485	29.0	0.957	1.131			
1567	29.4	0.970	1.146			
911	29.7	0.980	1.158			
673	30.0	0.990	1.170			
437	30.3	1.000	1.181	0.0	0.0	
415	34.0	1.122	1.326	3.5	10.3	
393	38.0	1.254	1.481	7.5	19.7	
366	43.0	1.419	1.676	12.5	29.1	
60.8 MOLE PERCENT CO_2						
2632	33.5	0.957	1.306			
1843	34.0	0.971	1.326			
1201	34.5	0.986	1.345			
685	35.0	1.000	1.365	0.0	0.0	
667	38.0	1.086	1.481	4.0	10.5	
642	43.0	1.229	1.676	9.0	20.9	
614	48.0	1.371	1.871	15.0	31.3	
590	53.0	1.514	2.066	20.5	38.7	
568	58.0	1.657	2.261	25.5	44.0	
65.7 MOLE PERCENT CO_2						
1909	36.0	0.965	1.404			
1305	36.5	0.979	1.423			
998	36.7	0.984	1.431			
756	37.3	1.000	1.454	0.0	0.0	
747	40.0	1.072	1.559	4.0	10.0	
740	42.0	1.126	1.637	6.5	15.5	
723	47.0	1.260	1.832	11.5	24.5	
695	52.0	1.394	2.027	17.5	33.7	
70.7 MOLE PERCENT CO_2						
2586	38.0	0.950	1.382			
1381	39.0	0.975	1.418			
963	39.4	0.985	1.433			
785	40.0	1.000	1.455	0.0	0.0	
780	42.0	1.050	1.527	4.0	9.5	
768	47.0	1.175	1.709	11.0	23.4	
753	52.0	1.300	1.891	17.0	32.7	
733	57.0	1.425	2.073	22.0	38.6	

Press. (psig)	Total Vol, cc	Rel. Vol. (1)	Rel. Vol. (2)	Vapor (cc)	% Vol. Vapor	Upper Liq, cc
75.6 MOLE PERCENT CO_2						
2164	42.0	0.946	1.637			
1183	43.0	0.968	1.676			
820	44.4	1.000	1.731	0.0	0.0	
814	47.5	1.070	1.852	5.0	10.5	
808	53.0	1.194	2.066	10.5	19.8	
793	57.5	1.295	2.242	16.5	28.7	
779	62.0	1.396	2.417	22.5	36.3	
80.5 MOLE PERCENT CO_2						
1890	47.7		1.860			47.7
1386	48.2		1.879			48.2
1172	48.4		1.887			39.5
1037	48.6		1.895			34.0
919	48.8		1.903			32.0
828	49.0		1.910	0.0	0.0	30.5
825	51.0		1.988	4.0	7.8	28.0
824	53.0		2.066	7.0	13.2	27.0
820	57.0		2.222	11.5	20.2	26.5
812	62.0		2.417	17.0	27.4	26.0
85.4 MOLE PERCENT CO_2						
3235	54.9		2.140			45.4
2514	55.9		2.179			45.0
1796	56.9		2.218			42.5
1251	57.9		2.257			41.0
842	59.5		2.320	0.0	0.0	39.4
836	66.9		2.608	11.0	16.4	35.5
835	71.9		2.803	16.5	22.9	35.0
833	76.9		2.998	23.5	30.6	33.0
827	86.9		3.388	35.5	40.9	31.0
805	96.9		3.778	47.0	48.5	29.5
803	101.9		3.973	53.5	52.5	28.0
791	111.9		4.363	65.5	58.5	26.0
90.2 MOLE PERCENT CO_2						
5075	69.5		2.710			57.5
3695	71.5		2.788			59.0
2031	75.0		2.924			59.5
1547	77.0		3.002			60.0
846	80.0		3.119	0.0	0.0	60.8
845	82.0		3.197	3.5	4.3	58.5
841	92.0		3.587	16.5	17.9	55.0
836	102.0		3.977	29.0	28.4	51.5
830	112.0		4.366	42.0	37.5	48.5

(1) Volume relative to the volume at the saturation pressure of the indicated mixture.

(2) Volume relative to the volume at the saturation pressure of the original fluid (atmospheric pressure and 70°F for this system).

TABLE 2

Spraberry recombined reservoir oil - CO_2 swelling test @ 75°F

Press. (psig)	Total Vol.cc	Rel. Vol. (1)	Rel. Vol. (2)	Vapor (cc)	% Vol. Vapor
0 MOLE PERCENT CO_2					
3698	51.6	0.943	0.943		
2583	52.4	0.957	0.957		
1680	53.2	0.972	0.972		
1151	53.8	0.983	0.983		
875	54.5	0.996	0.996		
822	54.8	1.000	1.000	0.0	0.0
731	57.7	1.054	1.054	3.0	5.2
660	60.7	1.109	1.109	6.0	9.9
546	67.7	1.237	1.237	13.0	19.2
506	70.7	1.291	1.291	16.0	22.6
14.9 MOLE PERCENT CO_2					
3302	54.0	0.960	0.986		
2636	54.6	0.971	0.997		
2031	55.2	0.982	1.008		
1371	56.0	0.996	1.023		
1225	56.3	1.001	1.028	0.0	0.0
1190	57.3	1.019	1.046	1.4	2.4
1074	61.0	1.085	1.114	6.0	9.8
932	67.0	1.191	1.224	12.5	18.7
870	70.0	1.245	1.278	15.0	21.4
736	80.0	1.422	1.461	25.0	31.3
633	90.0	1.600	1.644	35.0	38.9
31.3 MOLE PERCENT CO_2					
3135	58.0	0.943	1.059		
2501	58.6	0.953	1.070		
2029	59.2	0.963	1.081		
1751	59.6	0.969	1.088		
1562	61.5	1.000	1.123	0.0	0.0
1390	66.0	1.073	1.205	6.5	9.8
1247	73.0	1.187	1.333	14.0	19.2
1086	83.0	1.350	1.516	24.0	28.9
1002	88.0	1.431	1.607	29.0	33.0
888	98.0	1.594	1.790	39.0	39.8
42.3 MOLE PERCENT CO_2					
4671	61.0	0.949	1.114		
3524	62.2	0.968	1.136		
2599	63.2	0.983	1.154		
2055	64.0	0.996	1.169		
1835	64.3	1.000	1.174	0.0	0.0
1785	65.0	1.011	1.187	1.5	2.3
1652	68.0	1.058	1.242	6.0	8.8
1587	70.0	1.089	1.278	9.5	13.6
1483	74.0	1.151	1.351	14.0	18.9
1438	76.0	1.183	1.388	16.5	21.7
1310	83.0	1.291	1.516	25.0	30.1
1171	93.0	1.447	1.698	36.0	38.7

Press. (psig)	Total Vol.cc	Rel. Vol. (1)	Rel. Vol. (2)	Vapor (cc)	% Vol. Vapor
51.1 MOLE PERCENT CO_2					
4773	66.0	0.940	1.205		
4300	66.6	0.948	1.216		
3257	68.0	0.968	1.242		
2104	69.8	0.994	1.275		
2025	70.3	1.000	1.283	0.0	0.0
1867	73.0	1.039	1.333	7.0	9.6
1701	78.0	1.110	1.424	15.5	19.9
1500	88.0	1.253	1.607	28.0	31.8
1357	98.0	1.395	1.790	39.5	40.3
1153	118.0	1.680	2.155	61.0	51.7
1012	138.0	1.964	2.520	82.0	59.4
56.5 MOLE PERCENT CO_2					
4534	70.5	0.953	1.287		
3868	71.4	0.965	1.304		
3303	72.2	0.976	1.318		
2811	73.0	0.987	1.333		
2377	73.8	0.998	1.348		
2309	74.0	1.000	1.351	0.0	0.0
2100	75.5	1.021	1.379	7.5	9.9
1857	80.0	1.081	1.461	15.0	18.8
1794	82.0	1.108	1.497	17.5	21.3
1480	98.0	1.325	1.790	37.0	37.8
1382	108.0	1.460	1.972	48.0	44.4
1285	118.0	1.595	2.155	59.0	50.0
1145	138.0	1.865	2.520	80.5	58.3
61.9 MOLE PERCENT CO_2					
4784	75.0	0.952	1.370		
4329	75.8	0.963	1.384		
3383	77.5	0.984	1.415		
2781	78.8	1.000	1.438	0.0	0.0
2706	79.0	1.003	1.443	4.5	5.7
2572	79.5	1.010	1.452	10.0	12.6
2224	81.5	1.035	1.488	16.5	20.2
1829	89.0	1.130	1.625	25.0	28.1
1725	94.0	1.194	1.717	30.5	32.4
1648	99.0	1.257	1.808	36.0	36.4
1520	109.0	1.384	1.991	47.5	43.6
1418	119.0	1.511	2.173	58.5	49.2
1258	139.0	1.765	2.538	80.0	57.6

Table 2 - Continued					
Press. (psig)	Total Vol.cc	Rel. Vol. (1)	Rel. Vol. (2)	Vapor (cc)	% Vol. Vapor
67.7 MOLE PERCENT CO_2					
4750	83.0	0.979	1.516		
4091	83.8	0.988	1.530		
3715	84.6	0.998	1.545		
3621	84.8	1.000	1.549	0.0	0.0
3536	85.0	1.002	1.552	10.0	11.8
3448	85.2	1.005	1.556	20.0	23.5
3389	85.4	1.007	1.560	25.0	29.3
3327	85.6	1.009	1.563	29.0	33.9
2649	88.0	1.038	1.607	29.5	33.5
2118	92.0	1.085	1.680	30.5	33.2
1781	103.0	1.215	1.881	40.0	38.8
1710	108.0	1.274	1.972	45.0	41.7
1503	128.0	1.509	2.337	65.5	51.2
1351	148.0	1.745	2.703	86.0	58.1
73.6 MOLE PERCENT CO_2					
5292	92.0	0.991	1.680		
5030	92.6	0.998	1.691		
4949	92.8	1.000	1.695	92.8	100.0
4862	93.0	1.002	1.698	85.7	92.2
4732	93.4	1.006	1.706	79.9	85.5
4560	93.8	1.011	1.713	74.1	79.0
4259	94.5	1.018	1.726	66.5	70.4
4069	95.0	1.024	1.735	62.5	65.8
3717	96.0	1.034	1.753	55.5	57.8
3154	98.0	1.056	1.790	49.5	50.5
2587	101.0	1.088	1.844	46.5	46.0
2122	106.0	1.142	1.936	47.0	44.3
1883	113.0	1.218	2.064	50.5	44.7
1738	123.0	1.325	2.246	58.5	47.6
1643	133.0	1.433	2.429	68.5	51.5
1493	153.0	1.649	2.794	88.5	57.8
79.7 MOLE PERCENT CO_2					
5070	111.4	1.174	2.034	82.1	73.7
4999	112.0	1.180	2.045	81.8	73.0
4457	114.0	1.201	2.082	79.0	69.3
3520	118.0	1.243	2.155	75.5	64.0
2775	123.0	1.296	2.246	74.0	60.2
2192	131.0	1.380	2.392	76.0	58.0
1792	151.0	1.591	2.757	89.0	58.9

(1) Volume relative to the volume at the saturation pressure of the indicated mixture.
(2) Volume relative to the volume at the saturation pressure of the original fluid.

TABLE 3
Composition of synthetic brine

Component	in 2000 g solution (g)
NaCl	61.26
KCl	0.58
$CaCl_2$ $2H_2O$	10.86
$MgCl_2$ $6H_2O$	5.19
Na_2SO_4	5.91
H_2O	1916.20

TABLE 4
Berea core properties

Property	Core A	Core B
Length (cm)	5.21	6.25
Diameter (cm)	1.27	1.27
Porosity	0.20	0.20
Pore Volume (cm^3)	1.32	1.58
Initial Brine Permeability (md)	36.90	195.60

TABLE 5

Summary of baseline experiments

Core #	Total Flow Rate (cc/hr)	Gas Fraction	Press. Drop (psid)	Total Mobility (md/cp)	Total Interstitial Velocity (ft/day)
A	16.8	0.200	41.84	6.74	52.21
	8.4	0.200	19.37	7.28	26.11
	4.2	0.200	9.97	7.07	13.05
	4.2	0.200	9.85	7.15	13.05
	16.8	0.333	33.78	8.35	52.21
	16.8	0.333	44.68	6.31	52.21
	8.4	0.333	19.48	7.24	26.11
	4.2	0.333	11.69	6.03	13.05
	4.2	0.333	9.49	7.43	13.05
	16.8	0.500	38.9	7.25	52.21
	8.4	0.500	16.79	8.39	26.11
	4.2	0.500	9.49	7.43	13.05
	16.8	0.667	28.37	9.94	52.21
	8.4	0.667	15.87	8.88	26.11
	4.2	0.667	7.97	8.84	13.05
	4.2	0.667	7.58	9.30	13.05
	16.8	0.800	24.85	11.34	52.21
	8.4	0.800	11.61	12.14	26.11
	4.2	0.800	5.99	11.77	13.05
	4.2	0.800	6.46	10.91	13.05
B	16.8	0.200	14.25	23.74	51.39
	8.4	0.200	11.15	15.17	25.70
	4.2	0.200	5.6	15.10	12.85
	16.8	0.333	17.44	19.40	51.39
	8.4	0.333	9.86	17.15	25.70
	4.2	0.333	4.97	17.02	12.85
	16.8	0.500	15.55	21.75	51.39
	8.4	0.500	8.23	20.55	25.70
	4.2	0.500	4.55	18.59	12.85
	16.8	0.667	11.3	29.94	51.39
	8.4	0.667	7.03	24.06	25.70
	4.2	0.667	3.71	22.80	12.85
	16.8	0.800	7.71	43.88	51.39
	8.4	0.800	5.41	31.26	25.70
	4.2	0.800	2.97	28.47	12.85

TABLE 6

Summary of foam tests

Core #	Total Flow Rate (cc/hr)	Gas Fraction	Press. Drop (psid)	Total Mobility (md/cp)	Total Interstitial Velocity (ft/day)	WAG Mobility (md/cp)	Resistance Factor
B	4.2	0.200	127	0.666	12.85	20.0	30.0
	4.2	0.333	145	0.583	12.85	18.8	32.1
	4.2	0.500	172	0.492	12.85	21.3	43.3
	4.2	0.667	216	0.392	12.85	27.9	71.3
	4.2	0.200	171	0.495	12.85	20.0	40.5
	4.2	0.800	253	0.334	12.85	38.7	115.8
	4.2	0.667	254	0.333	12.85	27.9	83.8

TABLE 7

Reservoir data

Reservoir size	660 ft by 660 ft by 160 ft
Mesh dimension	8 by 8 by 5
Grid size in the X direction	82.5 ft
Grid size in the Y direction	82.5 ft
Grid size in the Z direction	27, 40, 35,18,40 ft
Porosity of each layer	0.1, 0.06, 0.08, 0.15, 0.07
X-direction permeability of each layer	150, 70, 112, 1000, 70 md
Y-direction permeability of each layer	150, 70, 112, 1000, 70 md
Z-direction permeability of each layer	15, 7, 11.2, 100, 7 md

TABLE 8

Pendant drop parameters for 7 pure substances

Liquid	ρ_l (g/cc)	ρ_v (g/cc)	D_e (cm)	H_e (cm)	R_a (cm)	Condition
Water	0.998	5.2E-3	0.336	0.182	0.156	25°C, 1 Atm
	0.997	6.6E-3	0.227	0.127	0.107	22°C, 1 Atm
	0.996	6.7E-3	0.211	0.109	0.106	23°C, 1 Atm
	0.985	7.6E-3	0.196	0.095	0.096	28°C, 1 Atm
Decane	0.730	4.1E-3	0.256	0.138	0.116	25°C, 1 Atm
	0.763	0.104	0.244	0.197	0.120	50°C, 22 At
	0.761	0.126	0.239	0.195	0.114	65°C, 23 At
Decyl alcohol	0.829	4.6E-3	0.256	0.135	0.115	25°C, 1 Atm
2-2-4 trimethyl pentane	0.692	3.9E-3	0.248	0.138	0.111	25°C, 1 Atm
Heptane	0.684	2.9E-3	0.253	0.132	0.114	25°C, 1 Atm
Hexadecane	0.773	6.5E-3	0.264	0.145	0.119	25°C, 1 Atm
Toluene	0.865	2.7E-3	0.254	0.132	0.115	25°C, 1 Atm

TABLE 9

Surface tension values in mN/m from pendant drop measurements

Liquid	Jasper[98]	Hansen & Rodsrud[88]	Lopez de Ramos[95]	Present	Condition
Water			(72.03)	72.10	25°C, 1 Atm
			71.23	71.50	22°C, 1 Atm
			72.05	70.36	23°C, 1 Atm
			71.23	70.29	28°C, 1 Atm
Decane	23.5	22.3	22.2	23.03	25°C, 1 Atm
			20.02	15.67	50°C, 22 Atm
			17.79	14.06	65°C, 23 Atm
Decyl alcohol	28.6	25.3	25.7	26.59	25°C, 1 Atm
2-2-4 trimethyl pentante	18.4	18.1	18.1	18.73	25°C, 1 Atm
Heptane	19.7	27.1	23.7	24.3	25°C, 1 Atm
Hexadecane	27.1	23.7	24.3	25.3	25°C, 1 Atm
Toluene	28.1	25.6	25.5	27.1	25°C, 1 Atm

TABLE 10

Composition of oil produced by gravity drainage

Hydrocarbon Number	STO	Mole Fraction Yellow Oil	Brown Oil
5	0.09114	0.00122	0.00143
6	0.06631	0.00058	0.00103
7	0.14649	0.00190	0.00612
8	0.10466	0.00585	0.01799
9	0.06115	0.01425	0.03063
10	0.05053	0.03841	0.05731
11	0.03736	0.06110	0.07372
12	0.03561	0.08715	0.09773
13	0.03313	0.10453	0.11466
14	0.02572	0.08705	0.09355
15	0.02151	0.07932	0.08366
16	0.02020	0.07220	0.07295
17	0.02088	0.07893	0.07774
18	0.01485	0.05368	0.05020
19	0.01609	0.05446	0.04840
20	0.01142	0.03545	0.03029
21	0.01068	0.03057	0.02560
22	0.01016	0.02579	0.02109
23	0.00957	0.02142	0.01730
24	0.00898	0.01721	0.01382
25	0.00599	0.01051	0.00853
26	0.00846	0.01187	0.00952
27	0.00574	0.00682	0.00551
28	0.00852	0.00867	0.00711
29	0.00583	0.00488	0.00406
30	0.00566	0.00414	0.00354
31	0.00569	0.00363	0.00320
32	0.00555	0.00320	0.00293
33	0.00536	0.00291	0.00280
34	0.00540	0.00283	0.00283
35	0.00550	0.00285	0.00296
36	0.00822	0.00439	0.00472
37+	0.12763	0.06224	0.00709
Total	1.00000	1.00000	1.00000
MW	219.39	251.80	222.34

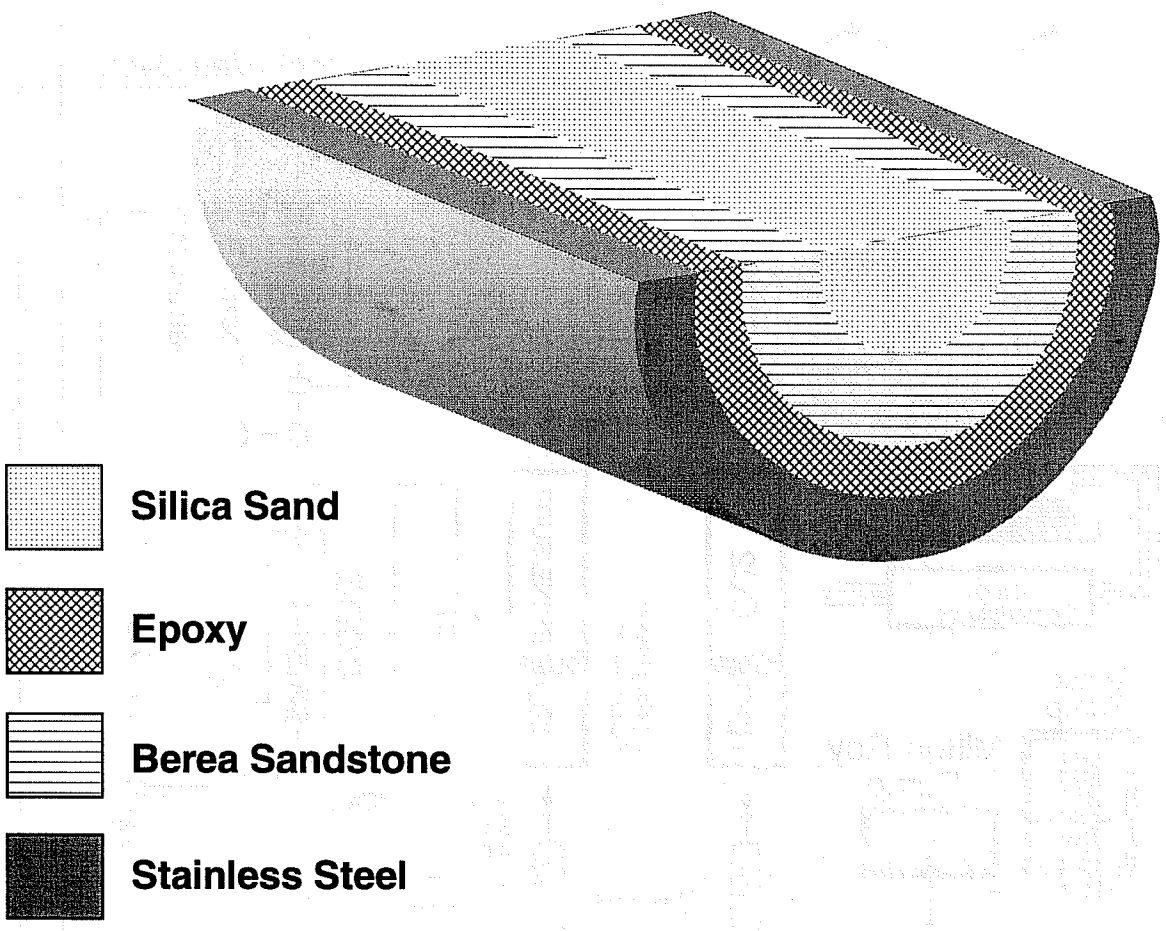

Figure 1. Schematic diagram of the axial sectional area of a composite parallel core.

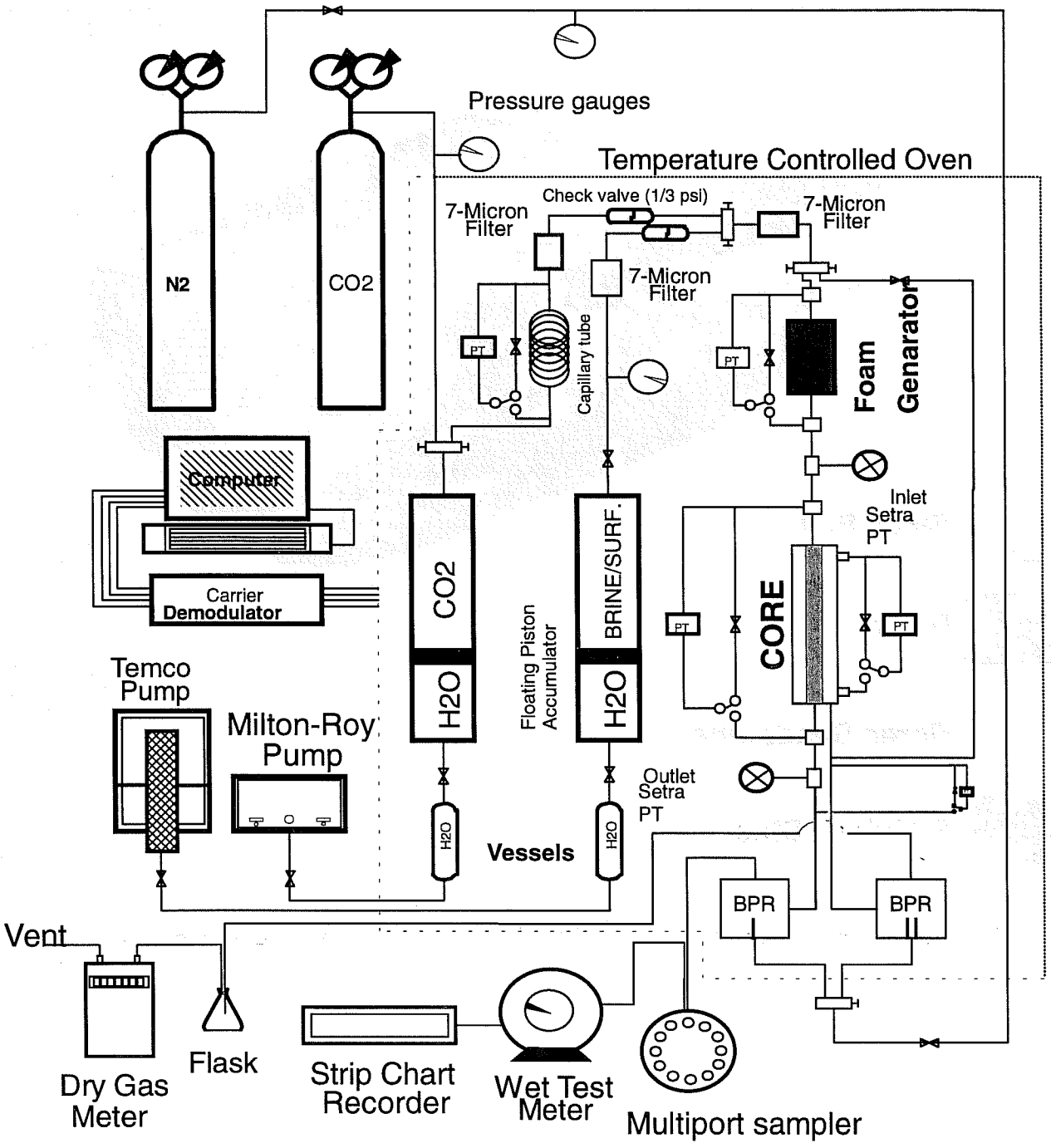

Figure 2. Schematic diagram of the high pressure experimental apparatus for a parallel composite core.

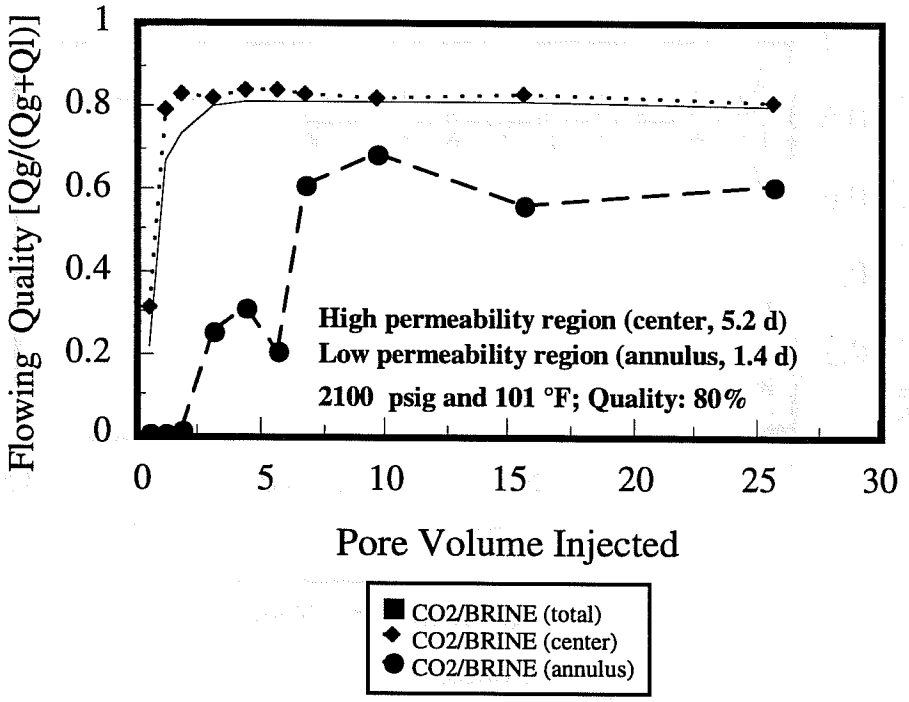

Figure 3. Flowing quality behavior of CO_2/brine in a parallel Core (I).

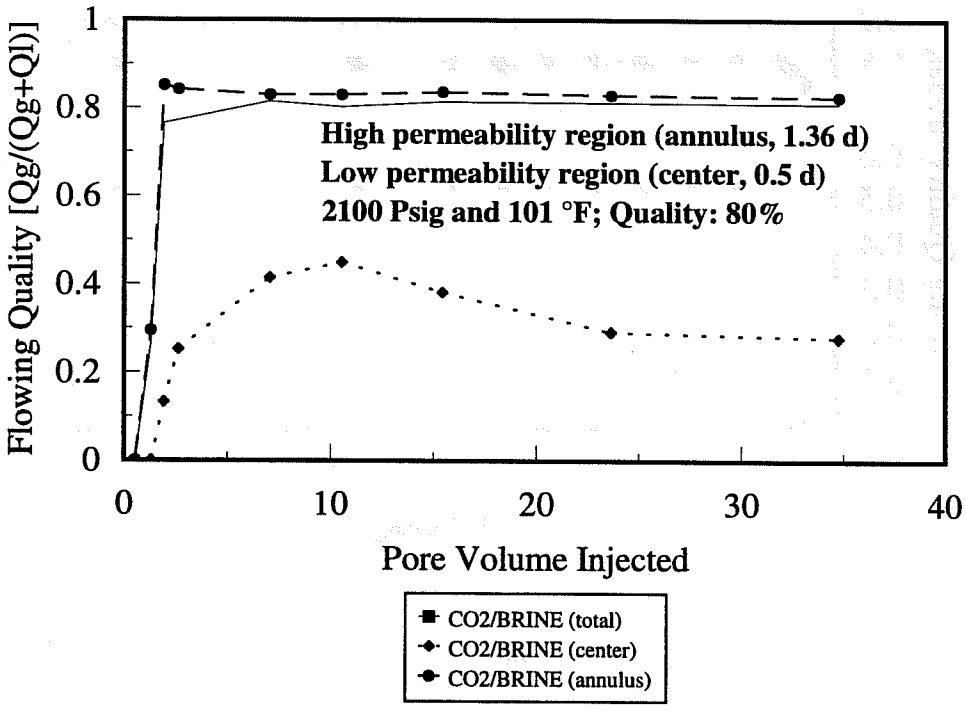

Figure 4. Flowing quality behavior of CO_2/brine in a parallel Core (II).

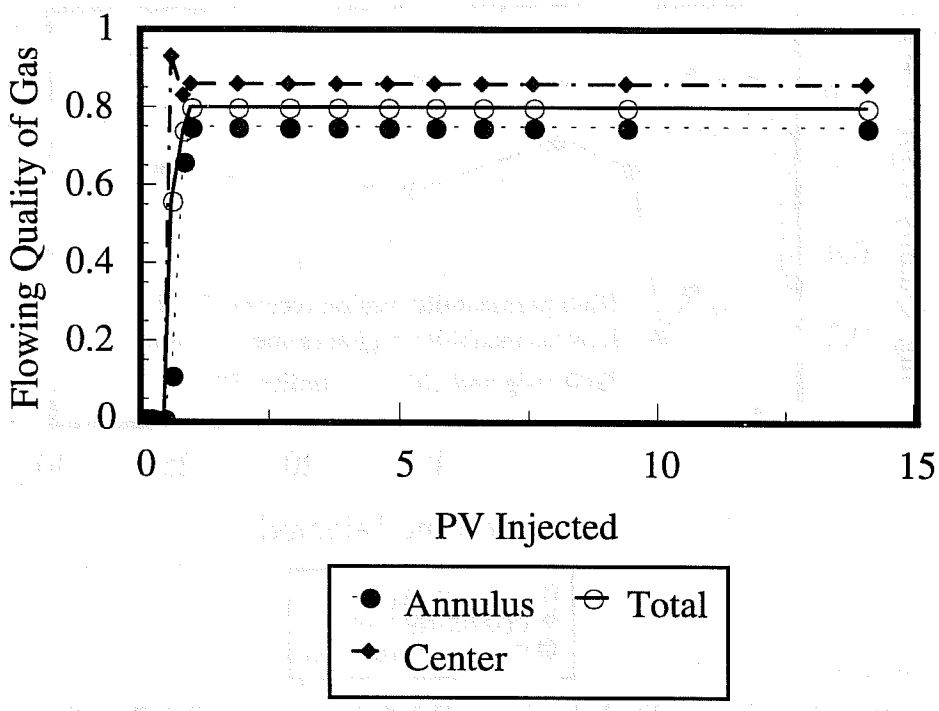

Figure 5. Effluent profiles in a simulated parallel core with higher permeability region in the center.

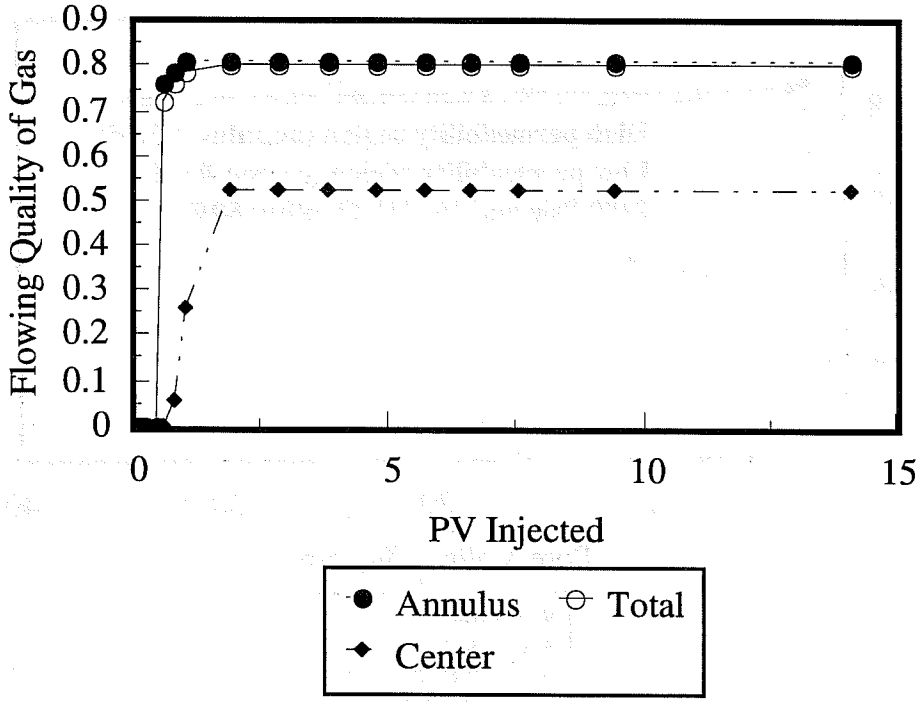

Figure 6. Effluent profiles in a simulated parallel core with lower permeability region in the center.

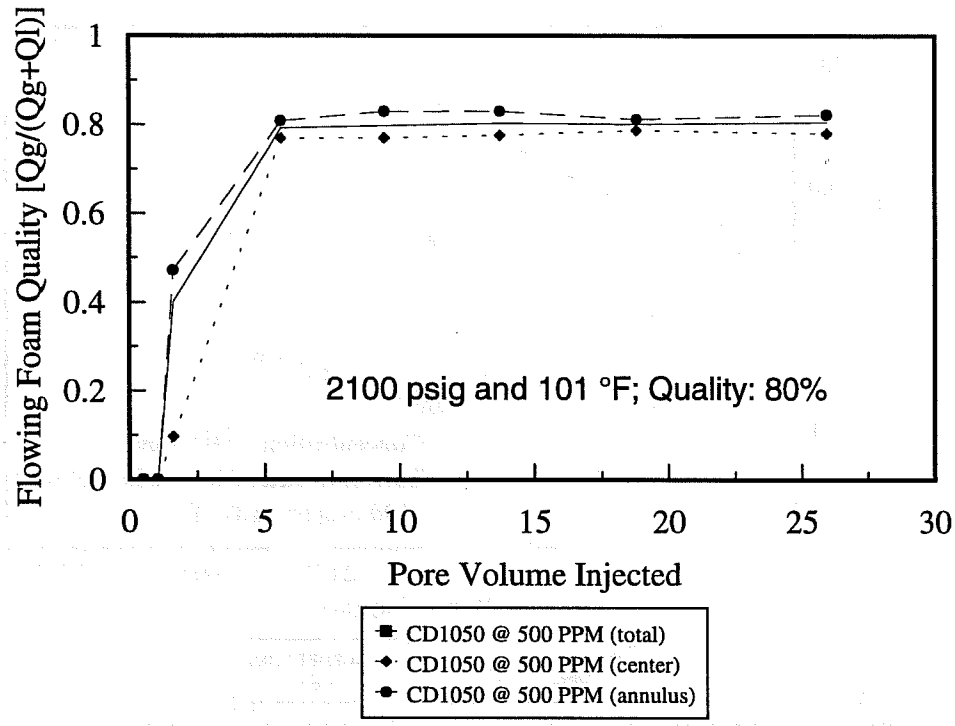

Figure 7. Foam flowing quality behavior in a parallel core (II).

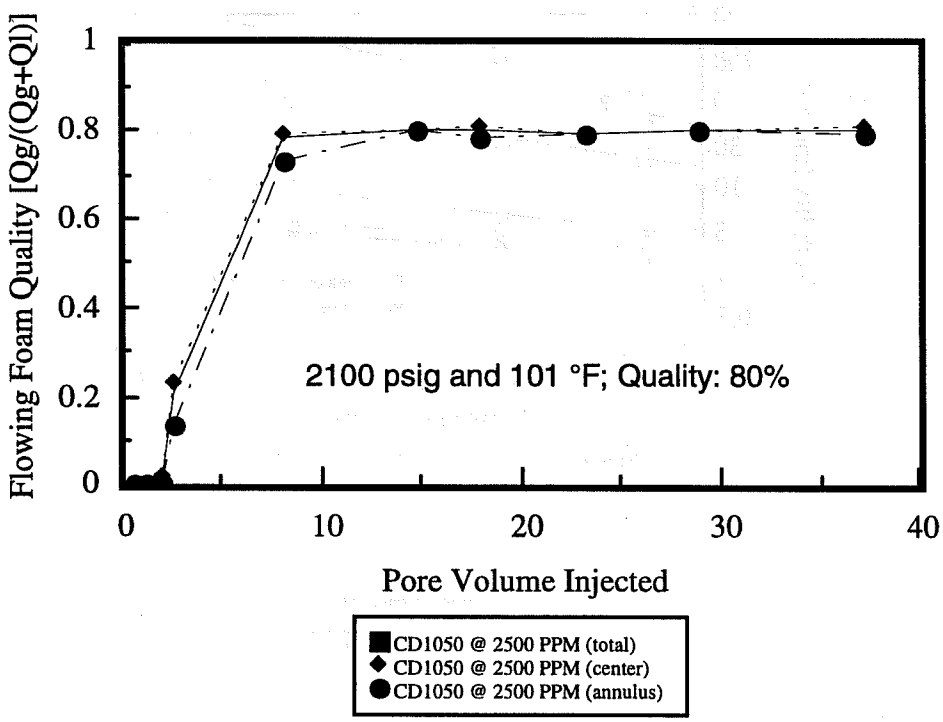

Figure 8. Foam flowing quality behavior in a parallel core (I).

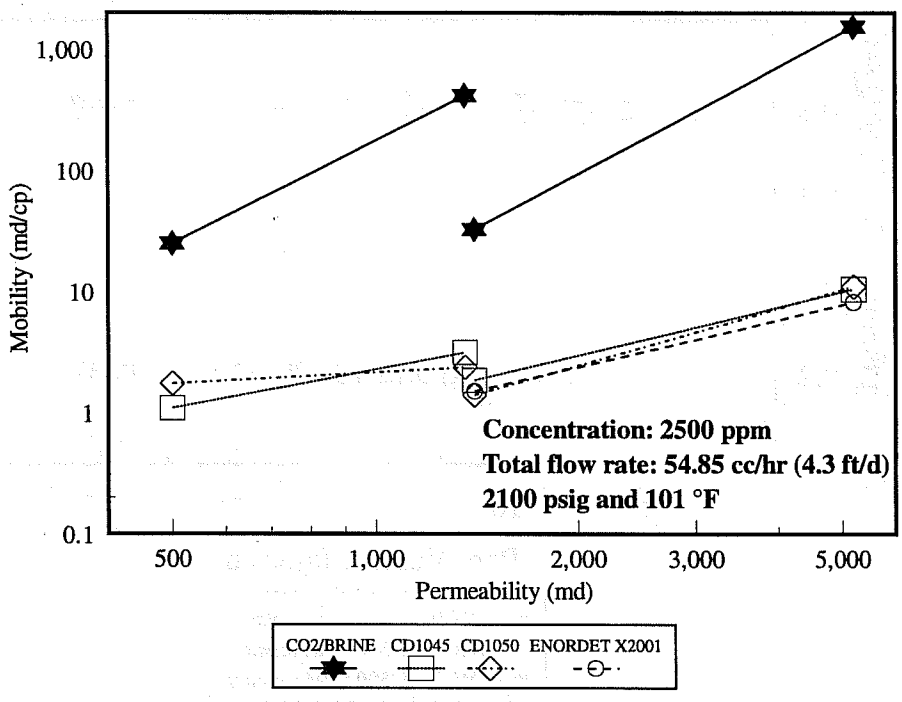

Figure 9. Mobility dependence on permeability in parallel composite cores at darcy flow velocity of 4.3 ft/day.

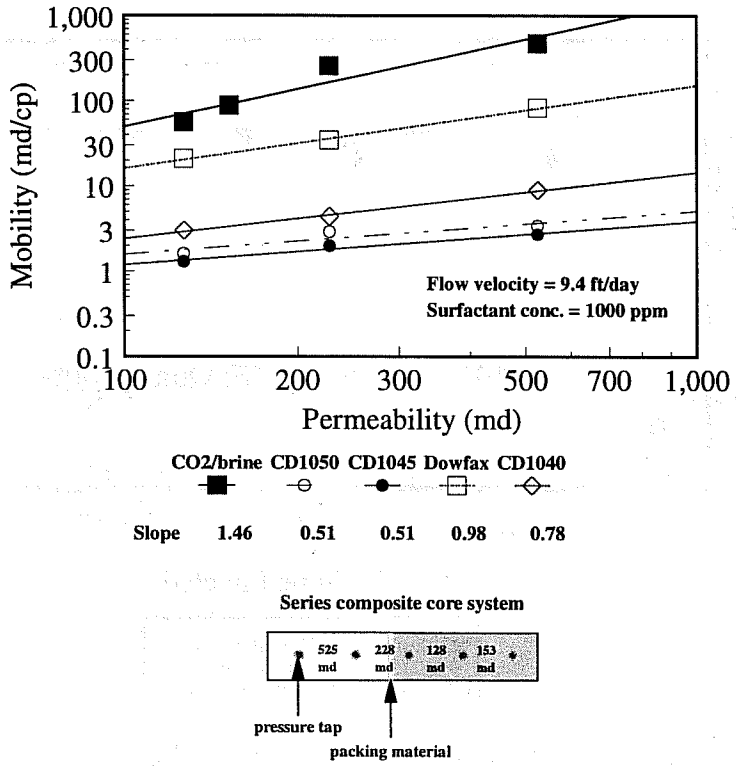

Figure 10. Mobility dependence on permeability in a series composite core.

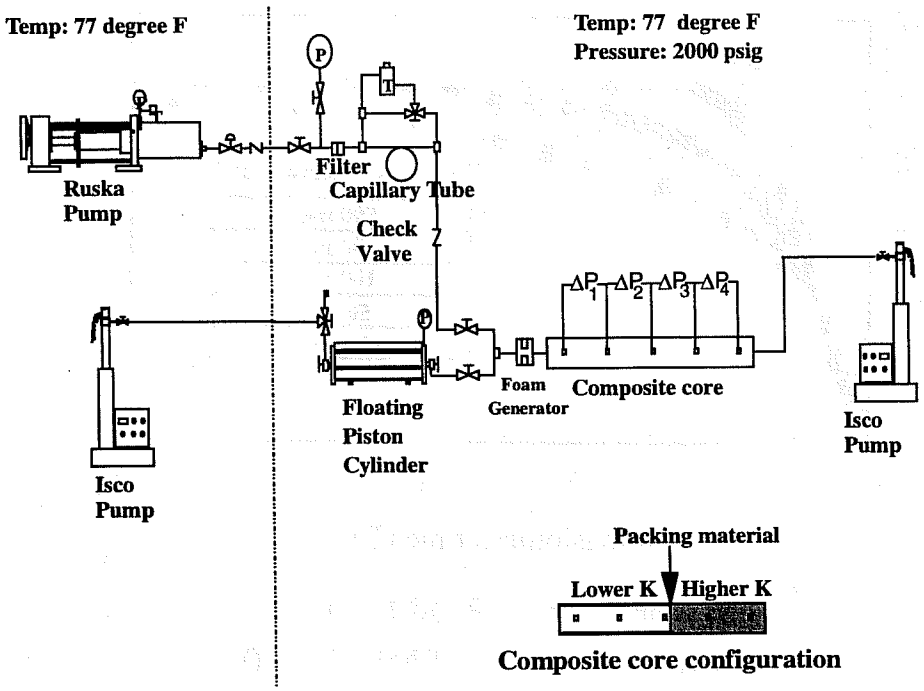

Figure 11. Schematic of the mobility measurement experimental setup for a series composite core.

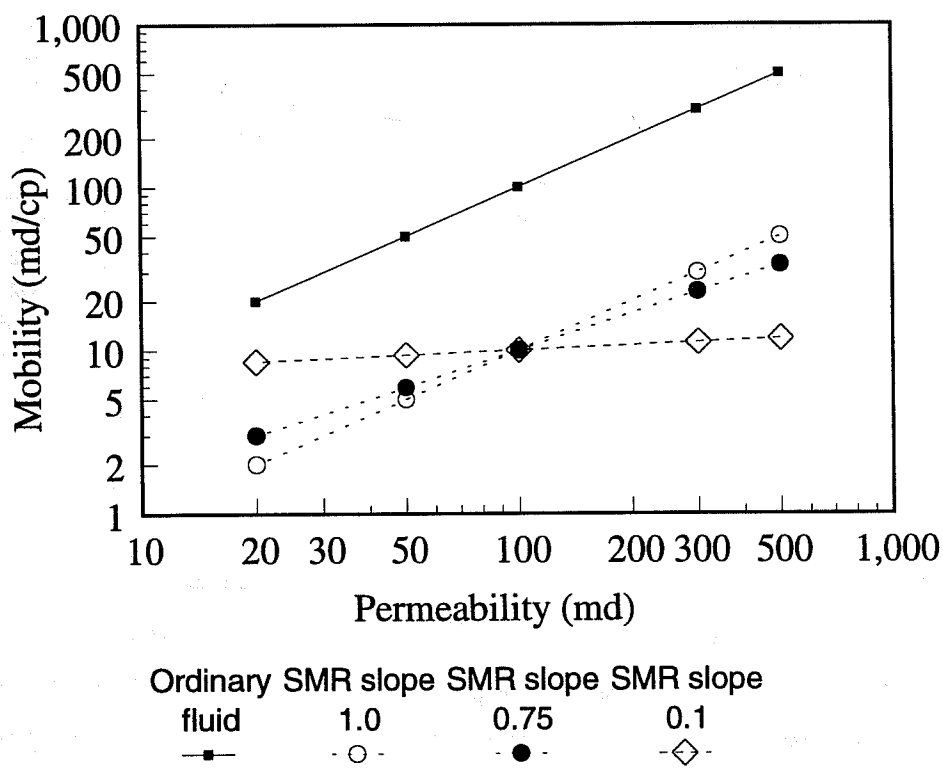

Figure 12. Mobility dependence on displacing fluid on permeability.

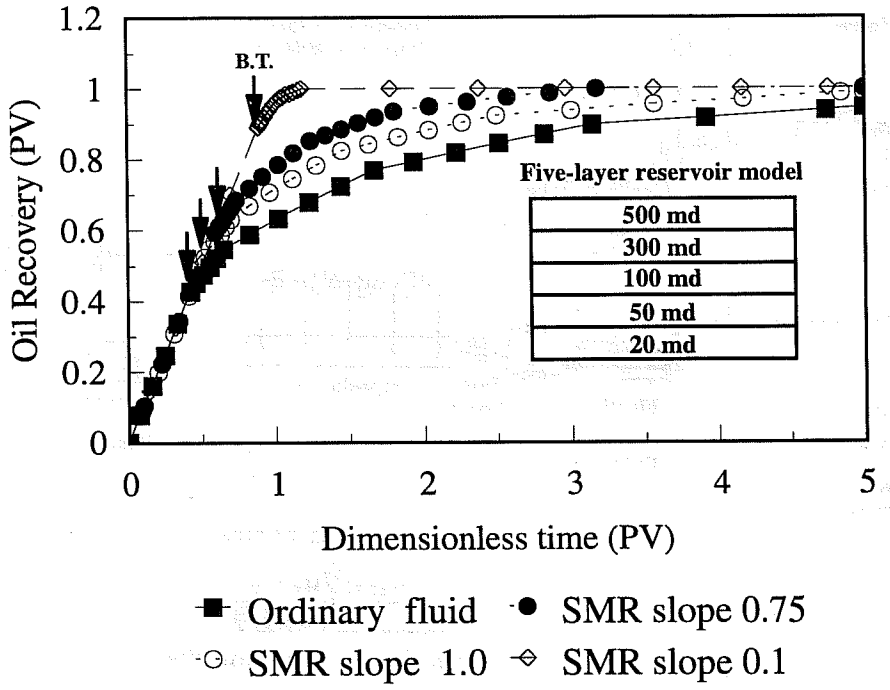

Figure 13. Oil recovery or vertical sweep efficiency for a five-layer reservoir model.

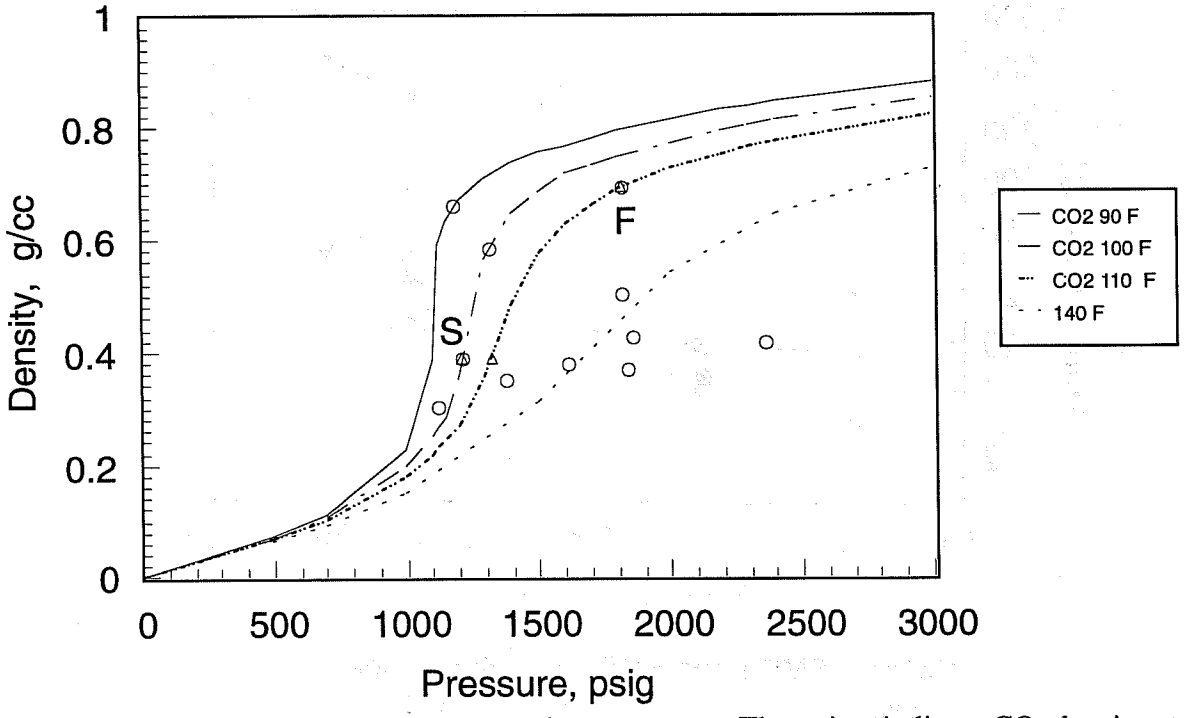

Figure 14. CO_2 density versus pressure and temperature. The points indicate CO_2 density at a number of system MMP's.

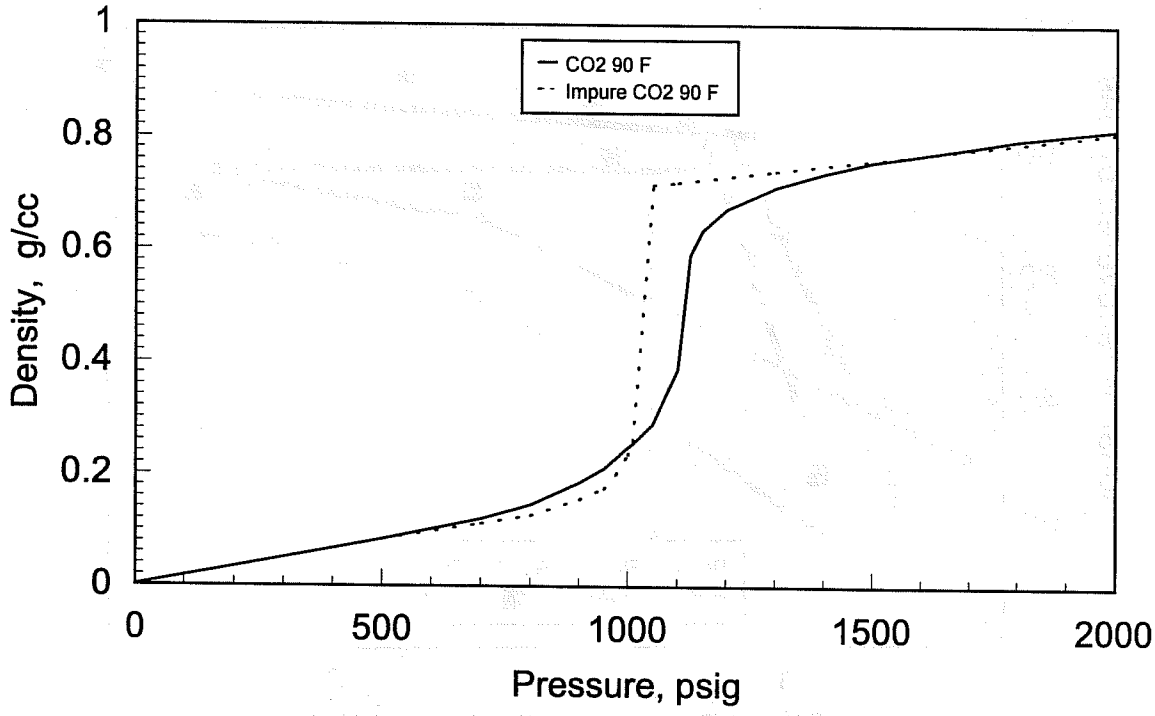

Figure 15. Density versus temperature comparison for pure CO_2 and CO_2 with extracted hydrocarbon content.

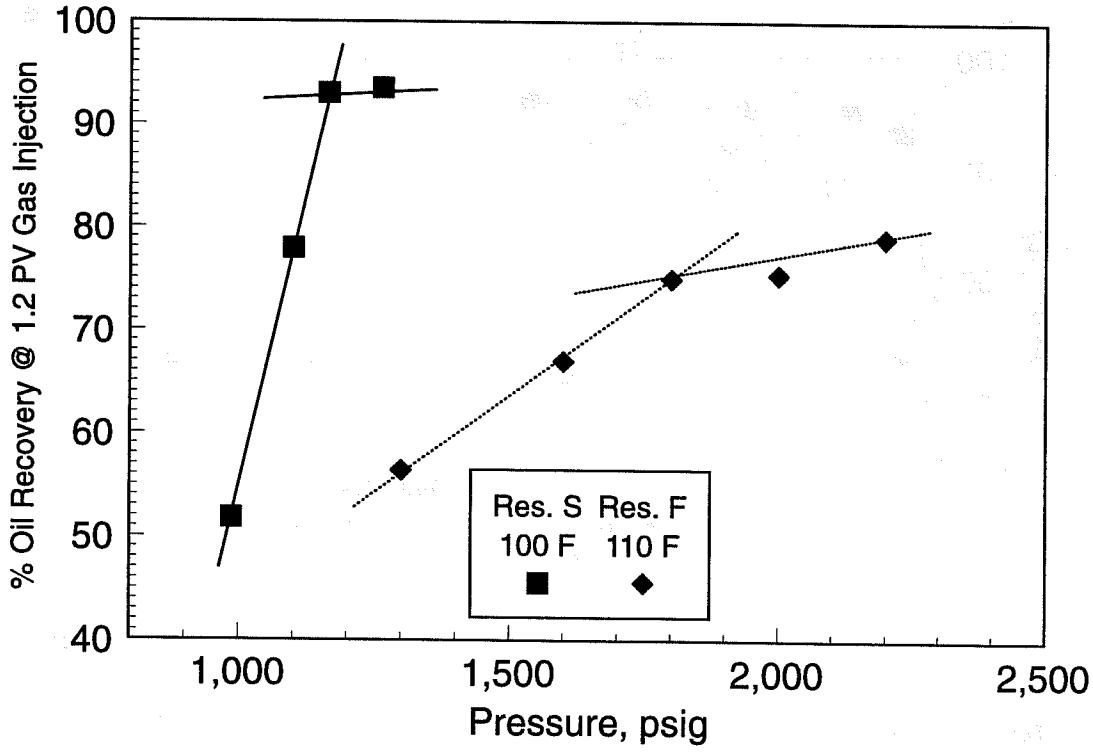

Figure 16. Slim tube recovery versus pressure for reservoir oils S and F[27].

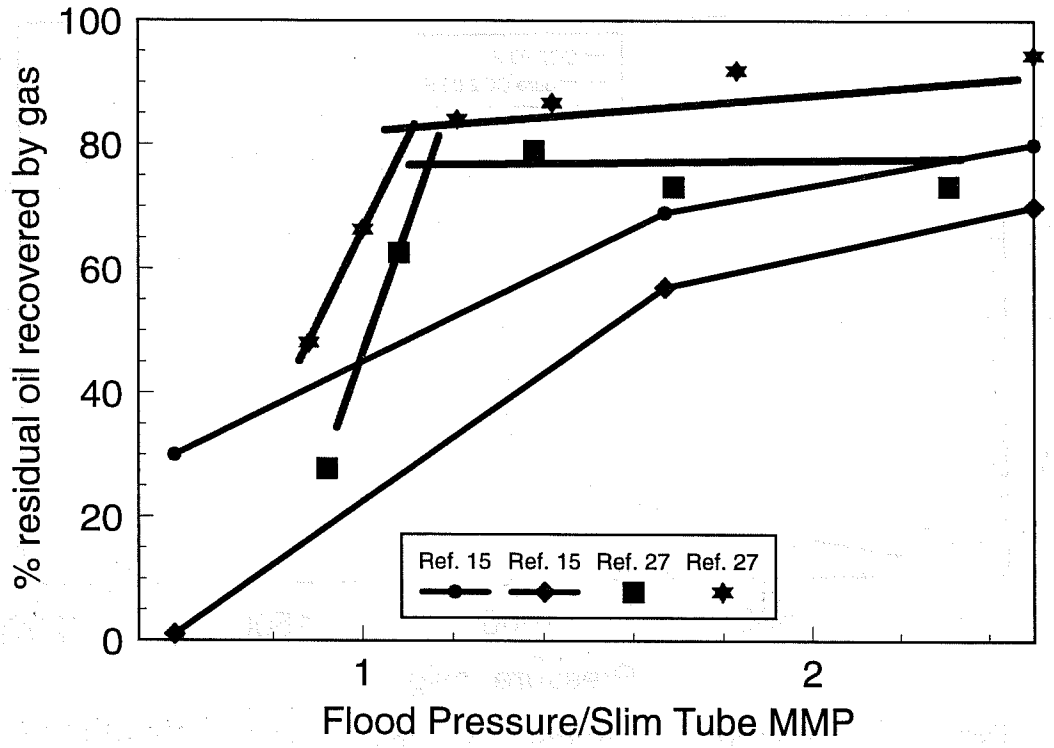

Figure 17. Comparison of core-tertiary CO_2 floods from references 15 and 27.

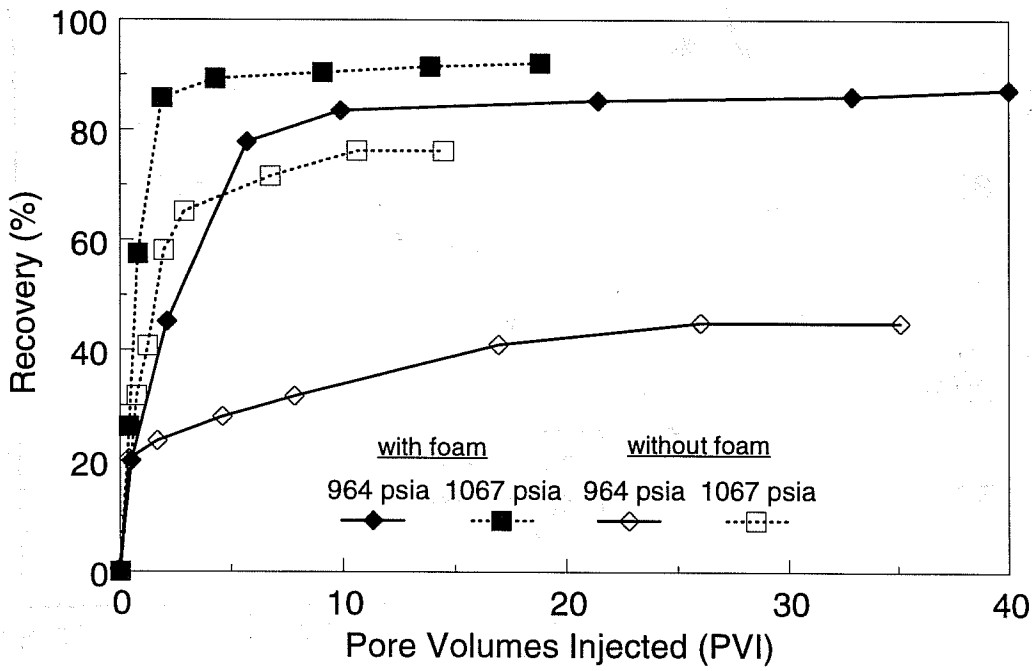

Figure 18. Comparison of CO_2 Floods in a visual micromodel with and without foam just above and below the MMP of about 1000 psig.

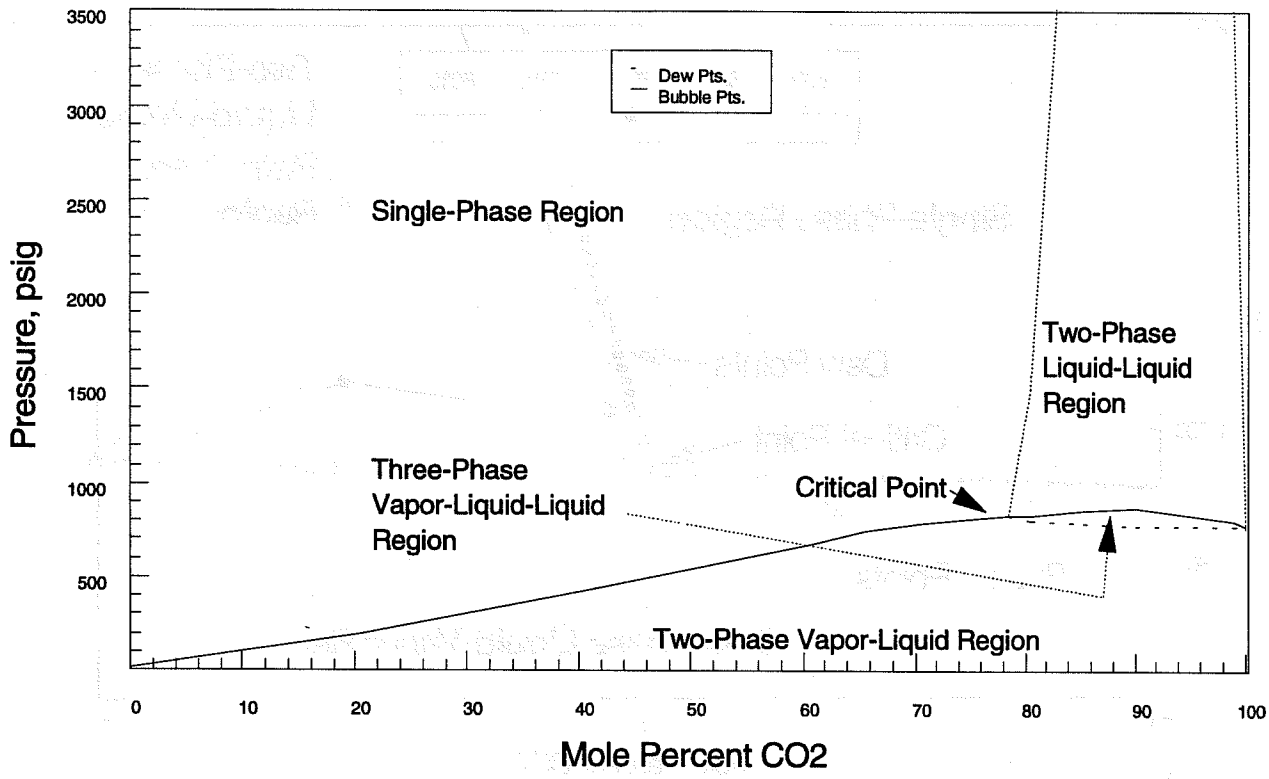

Figure 19. Sulimar Queen Phase Behavior Diagram using separator oil and CO_2.

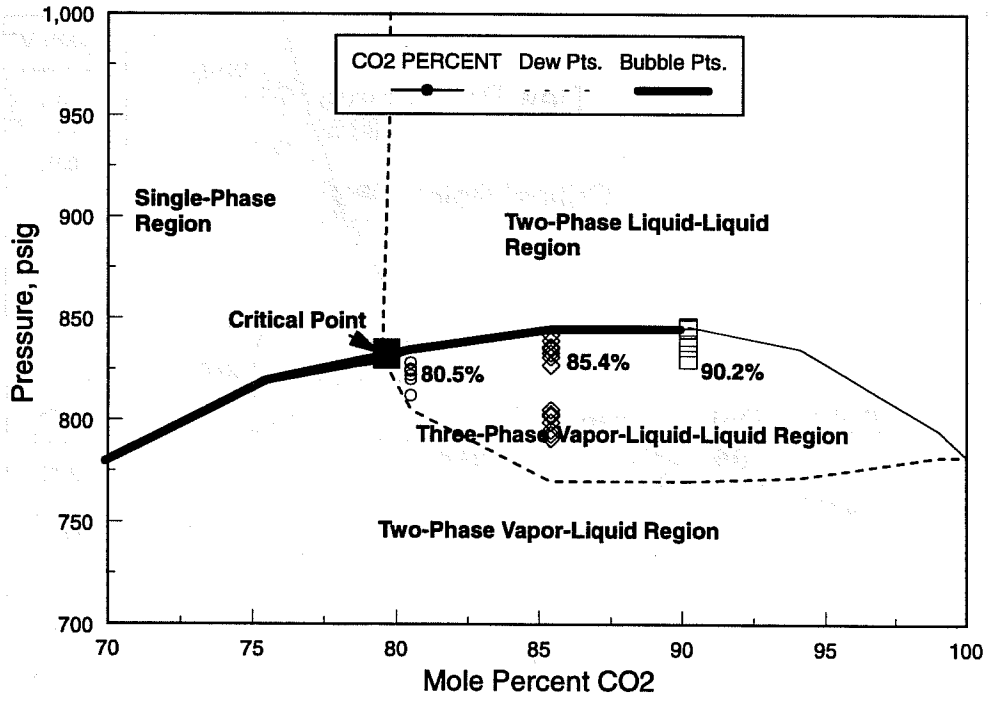

Figure 20. Sulimar Queen phase behavior diagram expanded in the three-phase region for separator oil and CO_2.

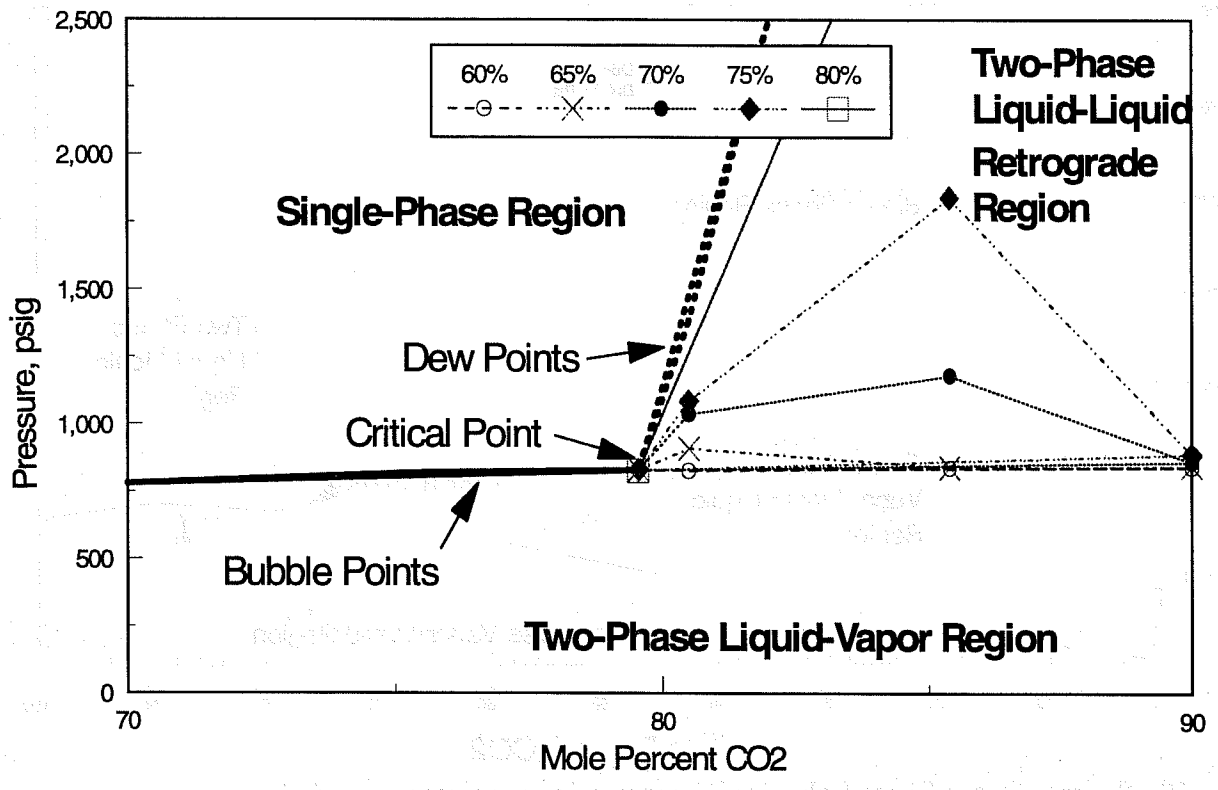

Figure 21. Sulimar Queen Phase Diagram expanded in the Liquid-Liquid region. Constant upper phase contours shown.

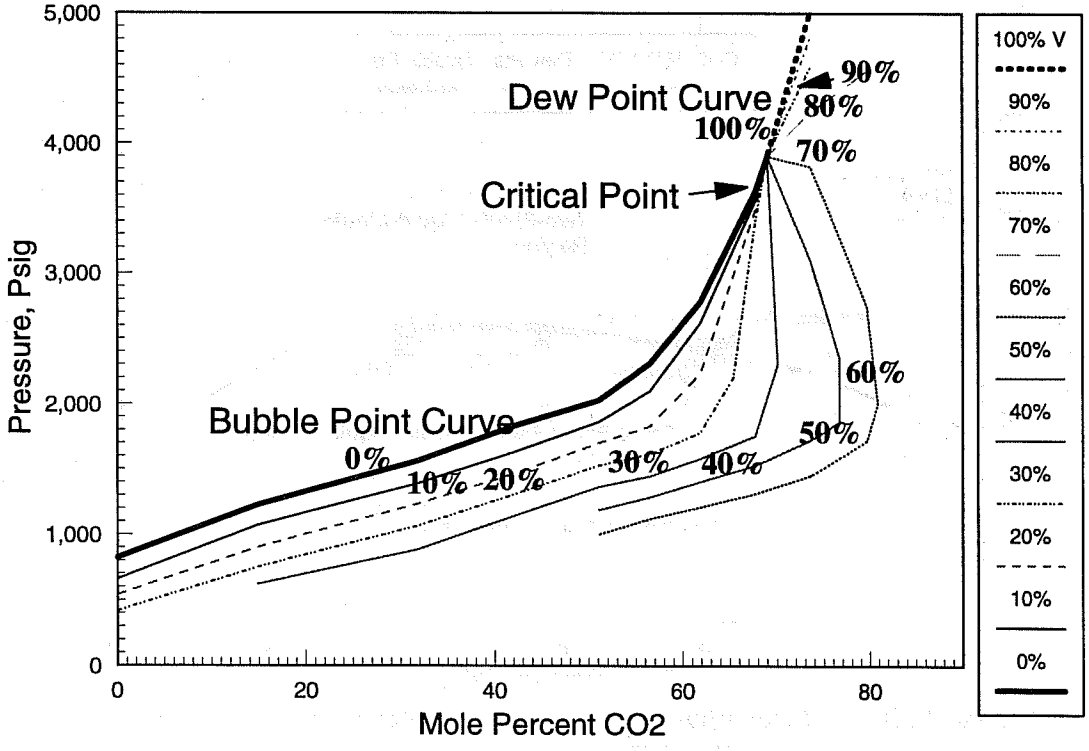

Figure 22. Spraberry Recombined Reservoir Oil with CO_2 constant volume % vapor contour lines.

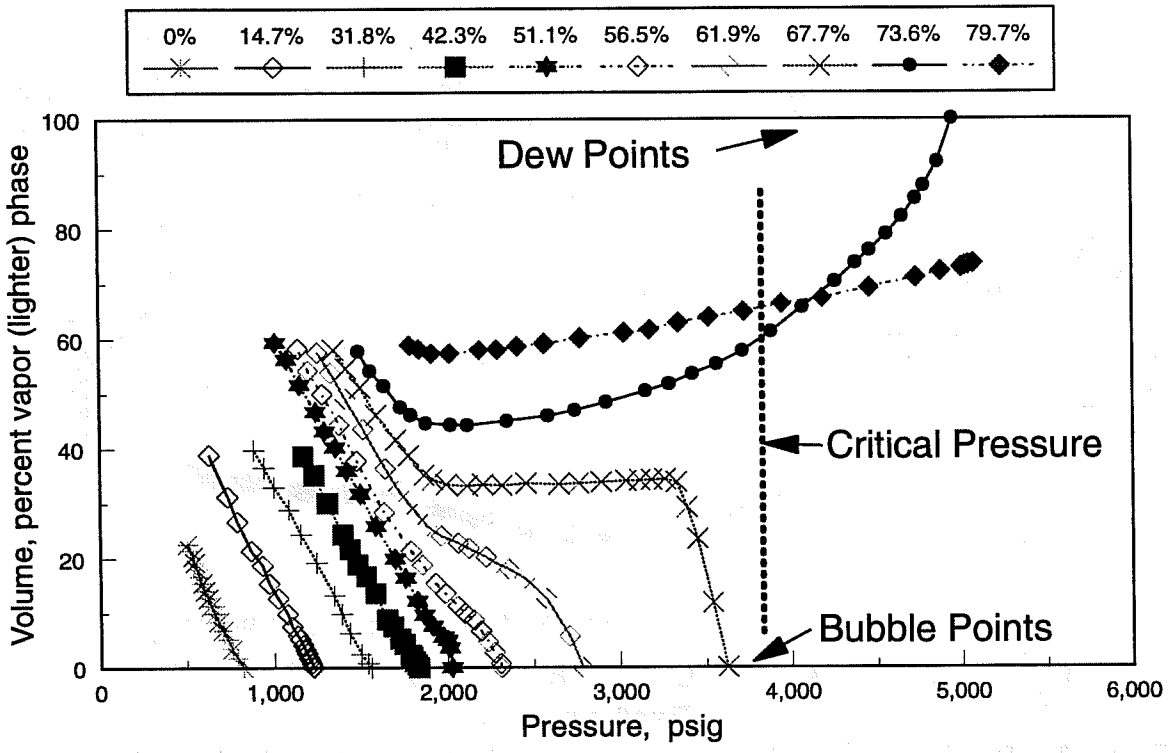

Figure 23. Gas volume percent versus pressure for each CO_2 concentration with Spraberry recombined reservoir oil.

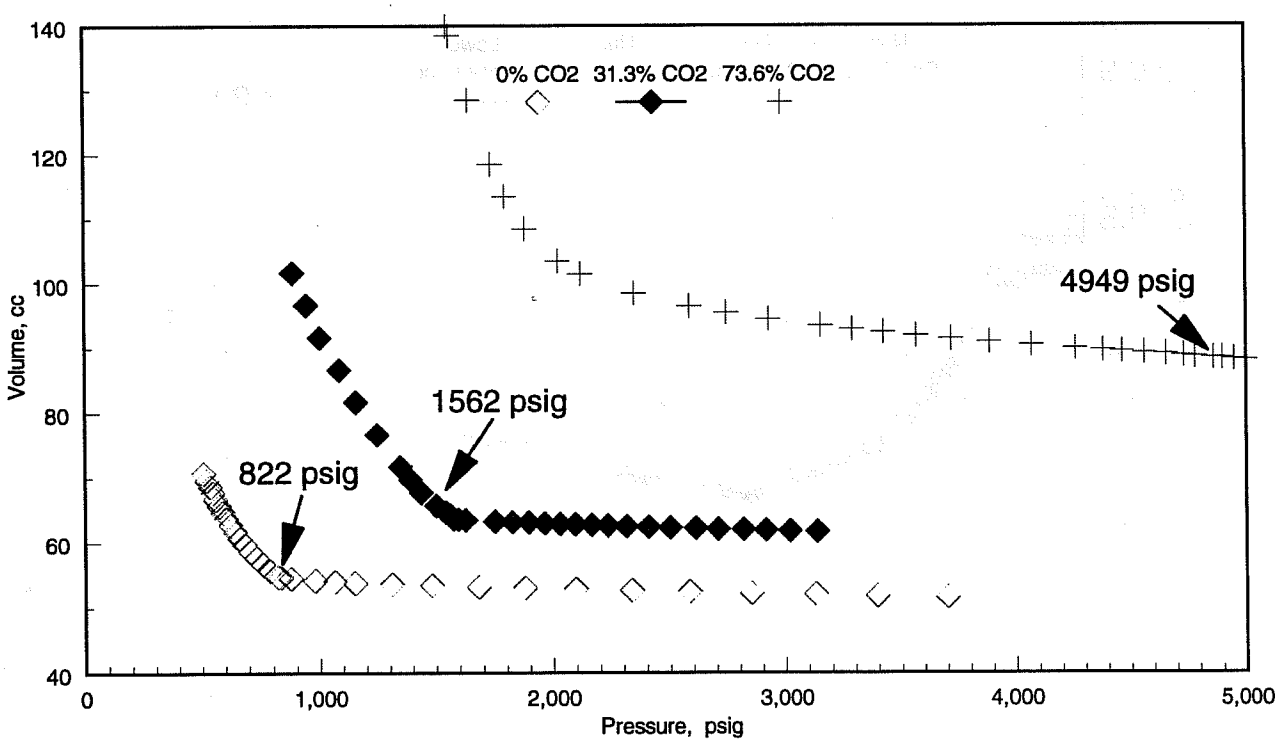

Figure 24. PV (pressure-volume) curves from three Spraberry Recombined Reservoir Oil with added CO_2.

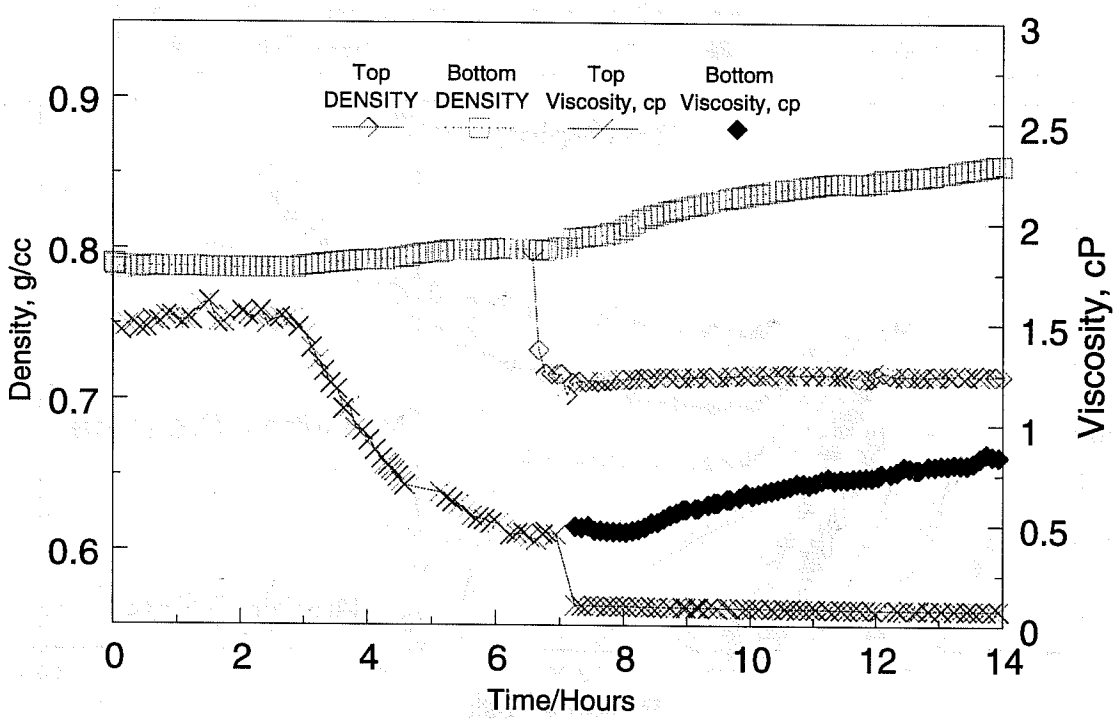

Figure 25. Density and viscosity measurements versus time for both the top and bottom production. Spraberry recombined reservoir fluid with CO_2 at 2450 psig and 138°F.

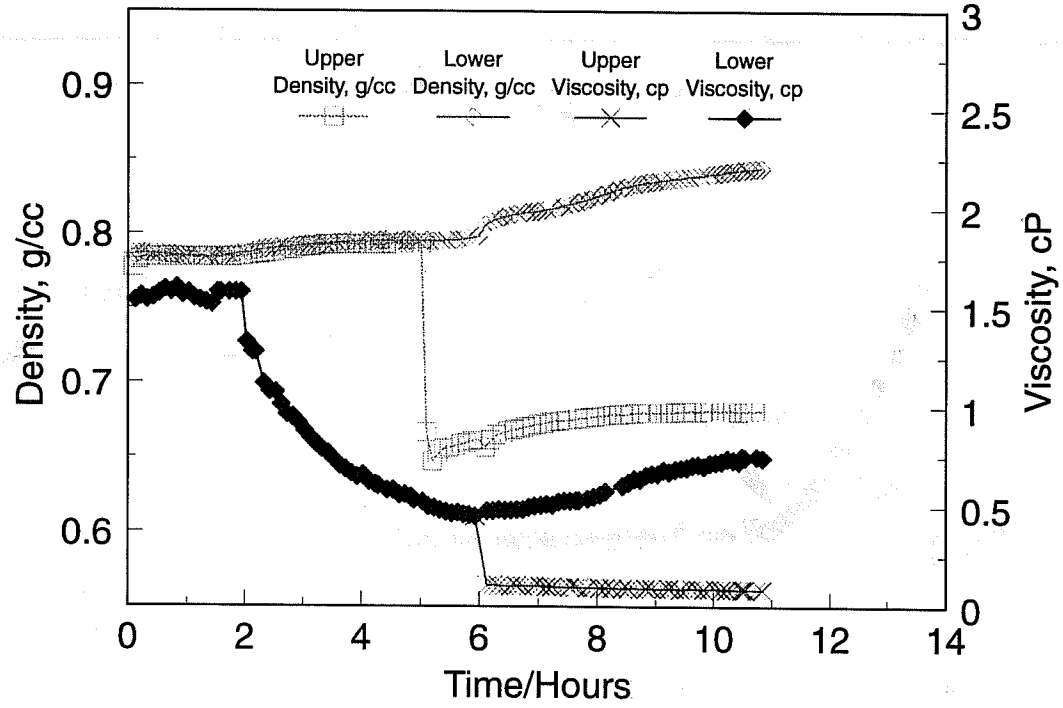

Figure 26. Density and viscosity measurements versus time for both the top and bottom production. Spraberry recombined reservoir fluid with CO_2 at 2100 psig and 138°F.

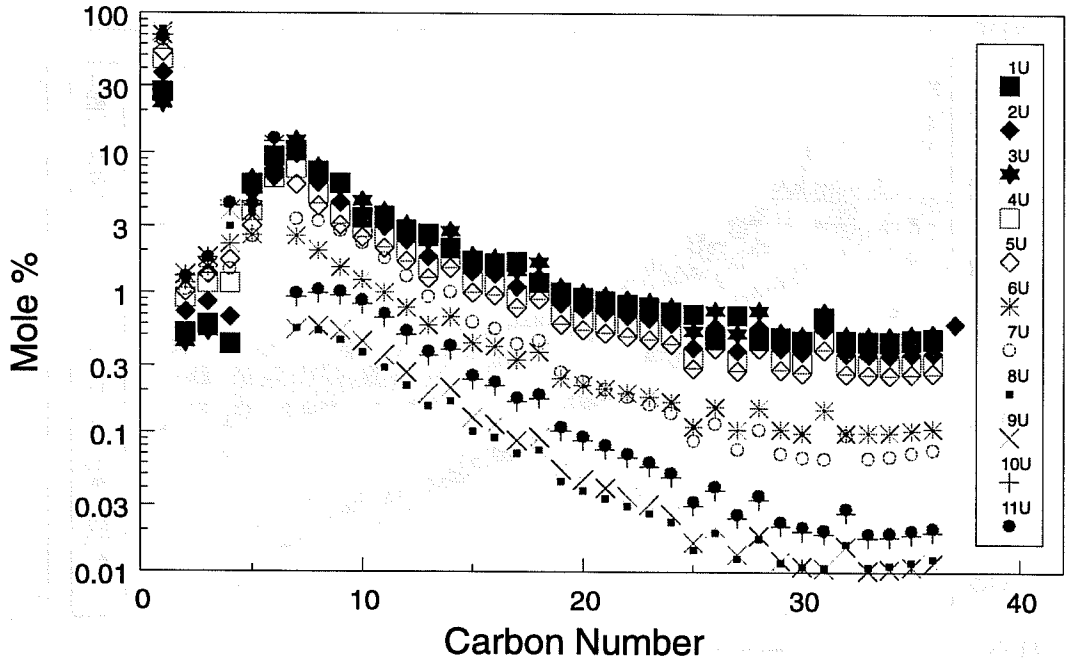

Figure 27. Spraberry Recombined Reservoir Oil: Composition versus time in the CPE for the top production at 2100 psig and 138°F.

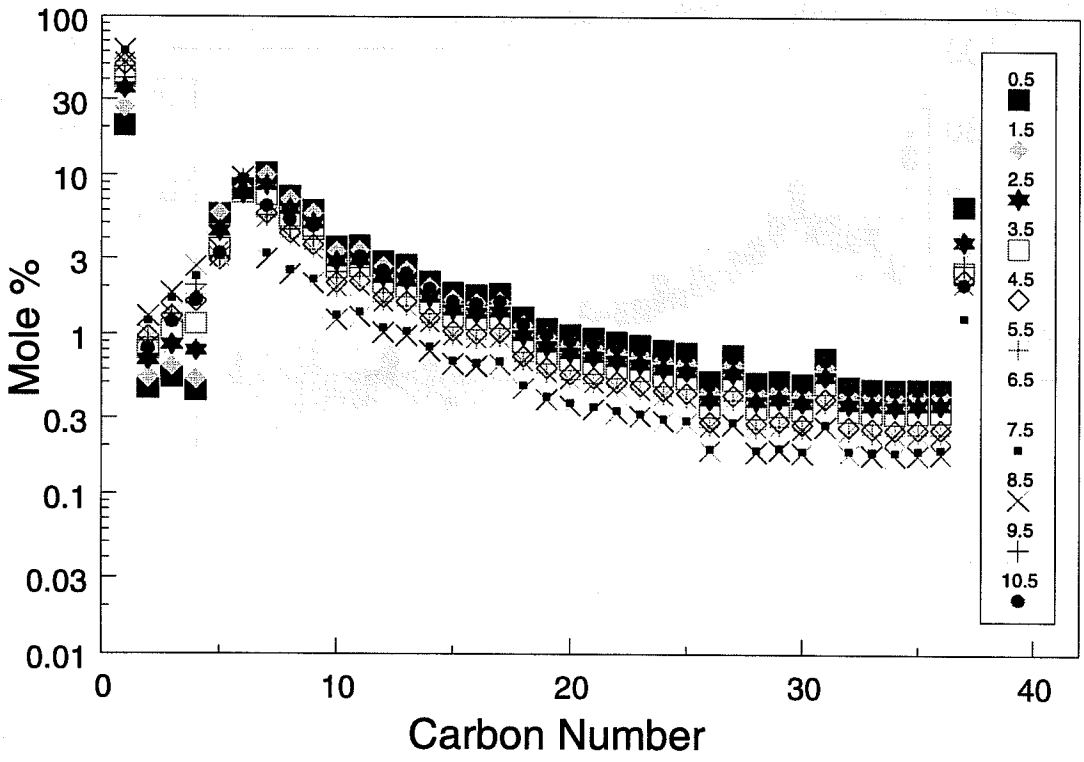

Figure 28. Spraberry recombined reservoir oil: composition versus time in the CPE for the bottom production at 2100 psig and 138°F.

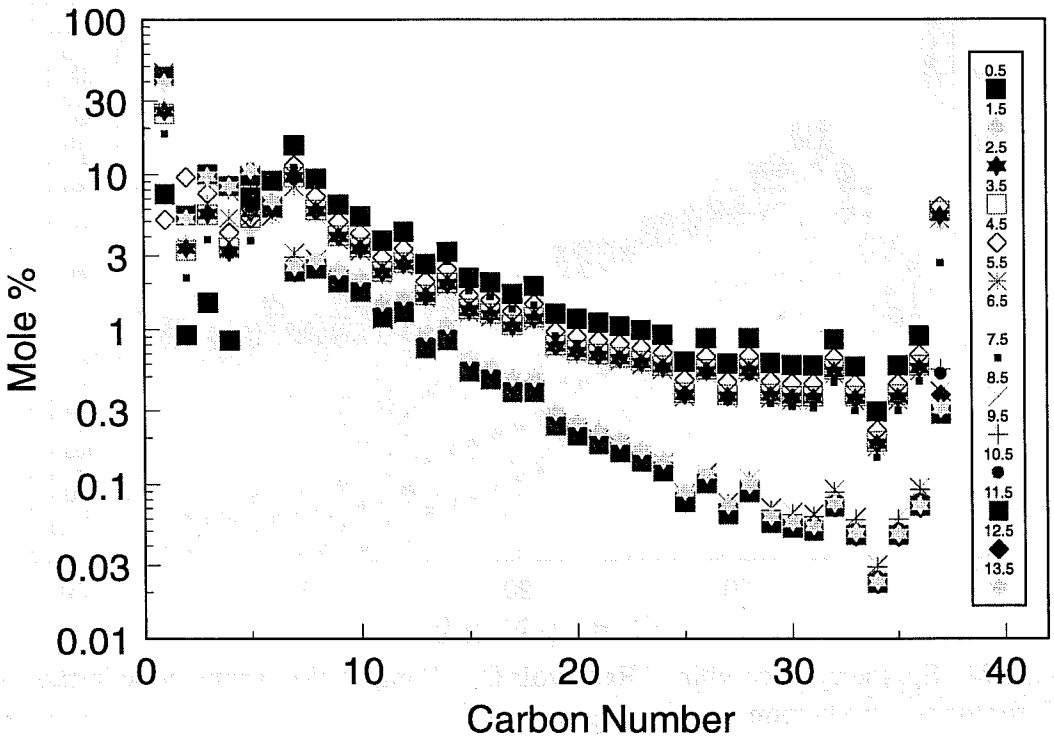

Figure 29. Spraberry Recombined Reservoir Oil: Composition versus time in the CPE for the top production at 2450 psig and 138°F.

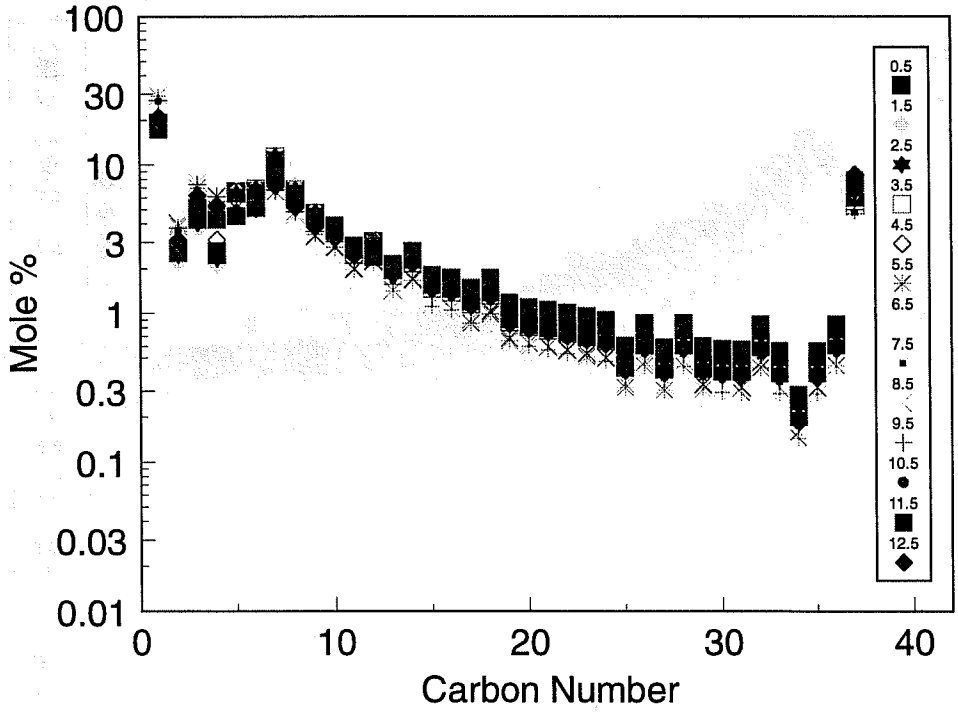

Figure 30. Spraberry Recombined Reservoir Oil: Composition versus time in the CPE for the bottom production at 2450 psig and 138°F.

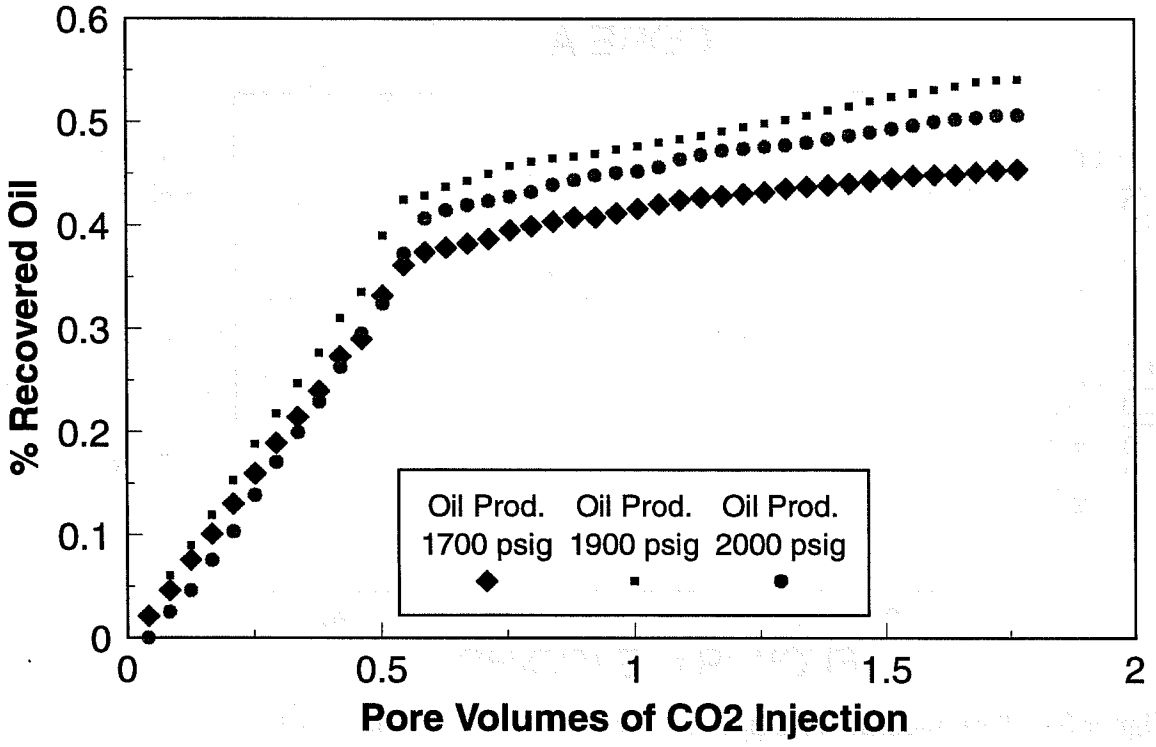

Figure 31. Slim Tube production comparisons versus pore volumes of CO_2 injected for three tests, 1700, 1900, and 2000 psig.

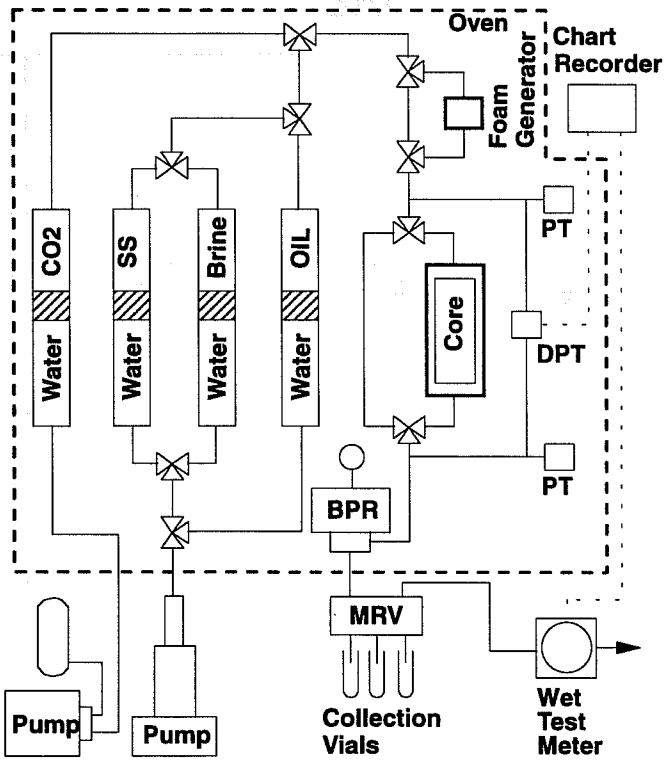

Figure 32. Schematic of the coreflood test apparatus.

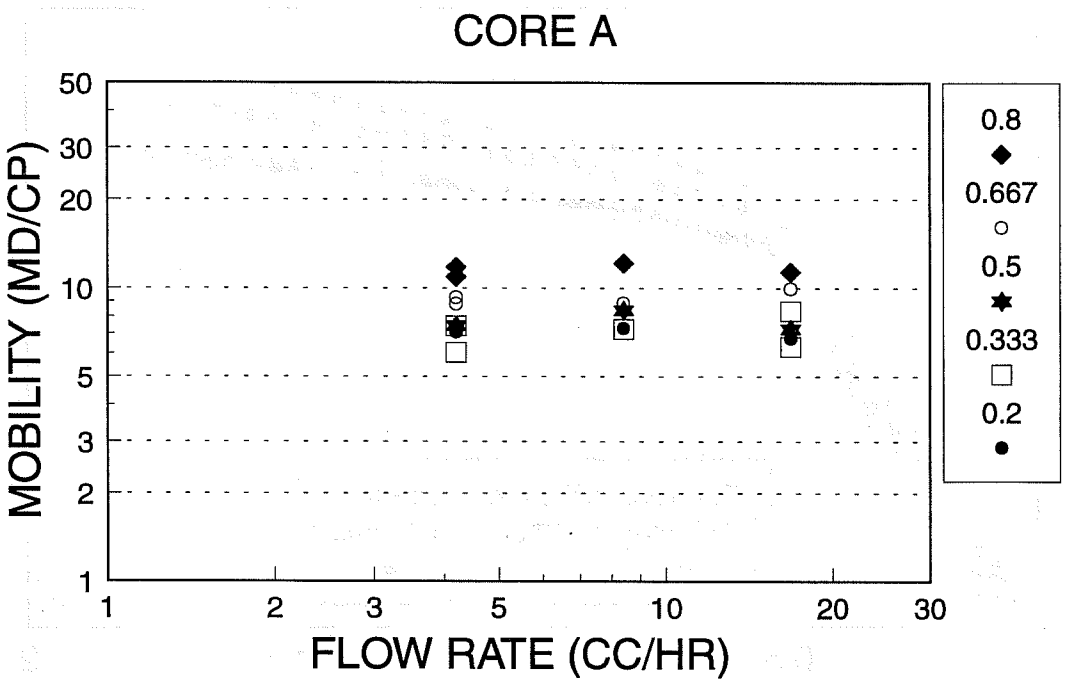

Figure 33. Total mobility of CO_2/brine versus total flowrate for gas fractions of 0.8, 0.667, 0.5, 0.333, and 0.2 (Core A).

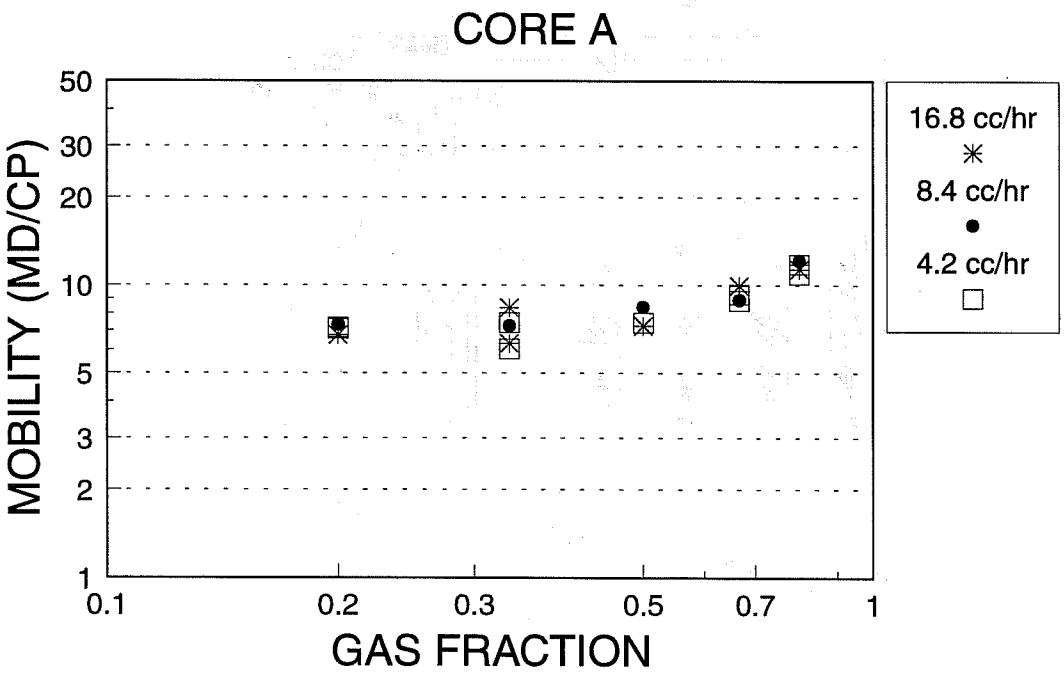

Figure 34. Total mobility of CO_2/brine versus total flow rate for flow rates of 16.8, 8.4, and 4.2 cc/hr (Core A).

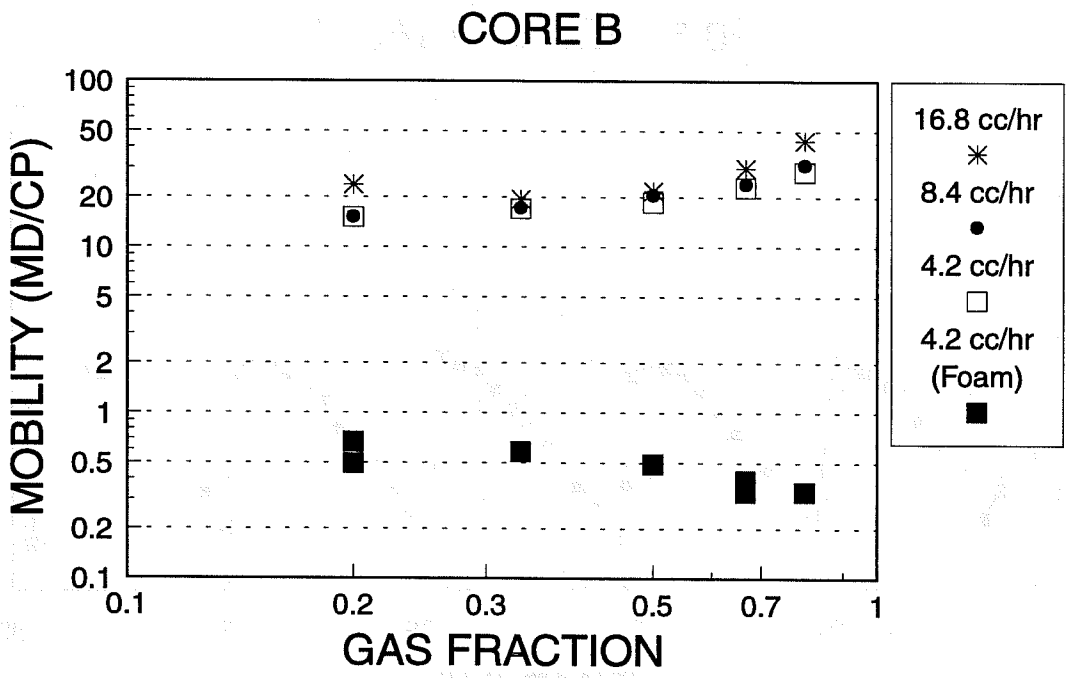

Figure 35. Total mobility of CO_2/brine versus gas fraction for total flow rates of 16.8, 8.4, and 4.2 cc/hr and foam mobility versus gas fraction at a total flow rate of 4.2 cc/hr (Core B).

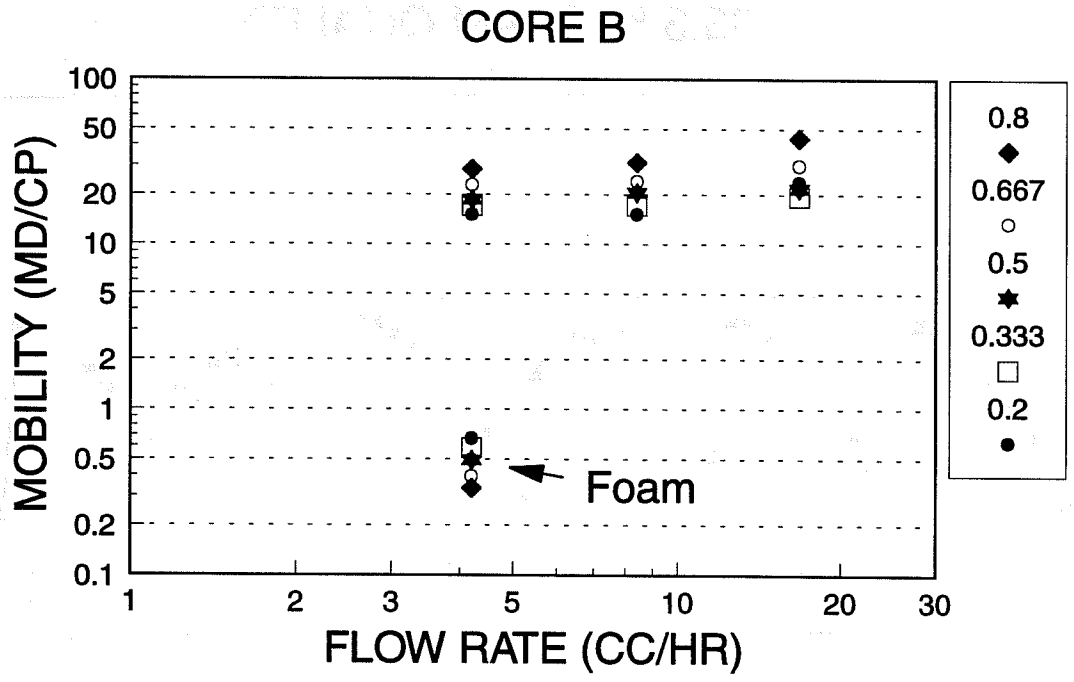

Figure 36. Total mobility of CO_2/brine versus total flow rate for gas fractions of 0.8, 0.667, 0.5, 0.333, and 0.2 and foam mobilities at a total flow rate of 4.2 cc/hr (Core B).

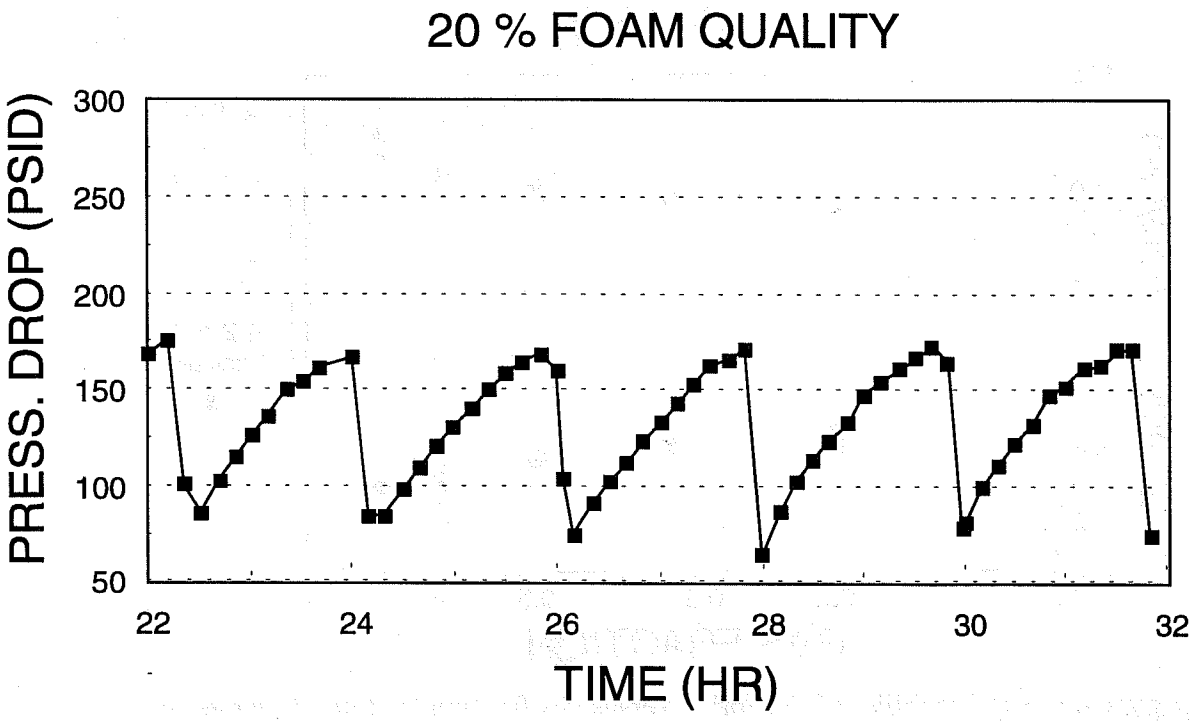

Figure 37. Pressure drop response of the foam test with 20% foam quality.

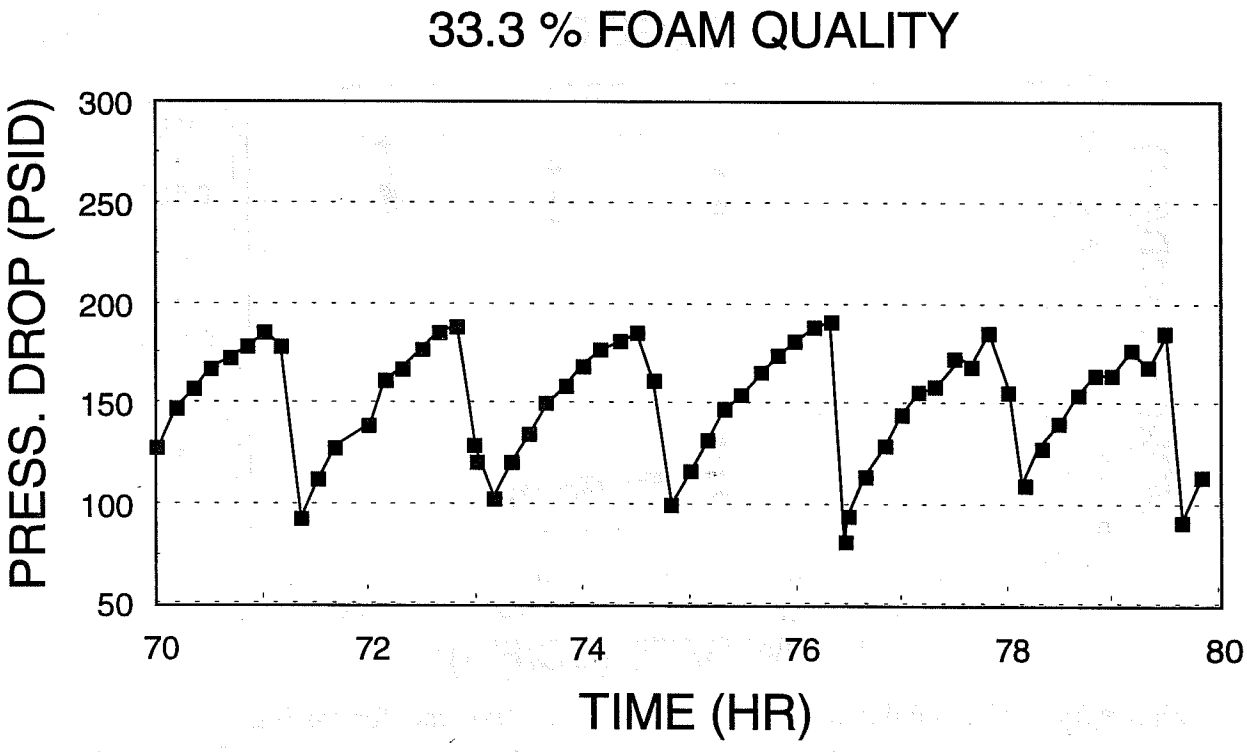

Figure 38. Pressure drop response of the foam test with 33.3% foam quality.

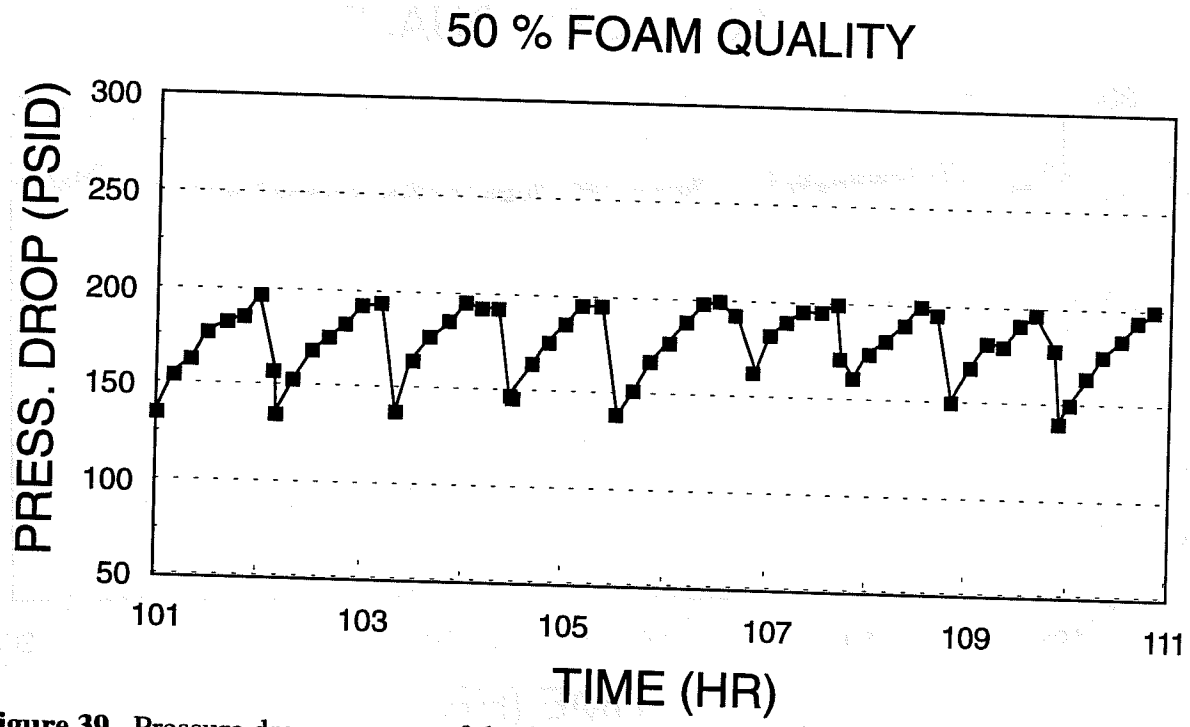

Figure 39. Pressure drop response of the foam test with 50% form quality.

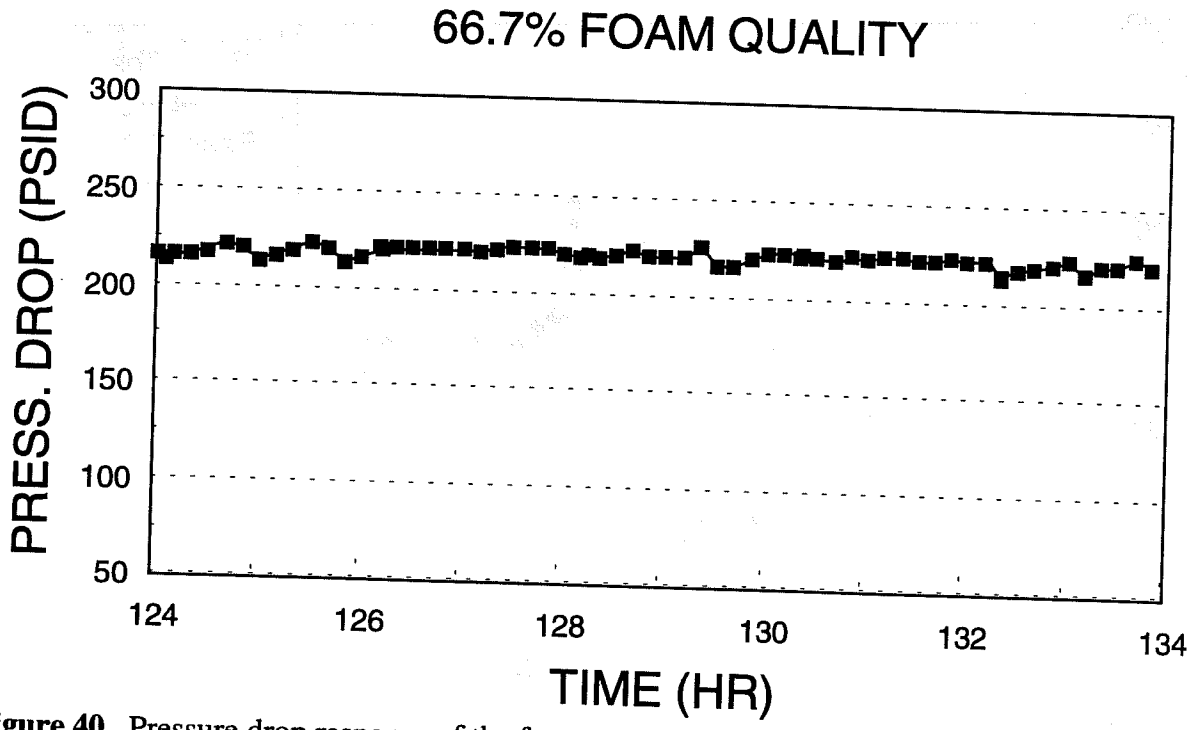

Figure 40. Pressure drop response of the foam test with 66.7% foam quality.

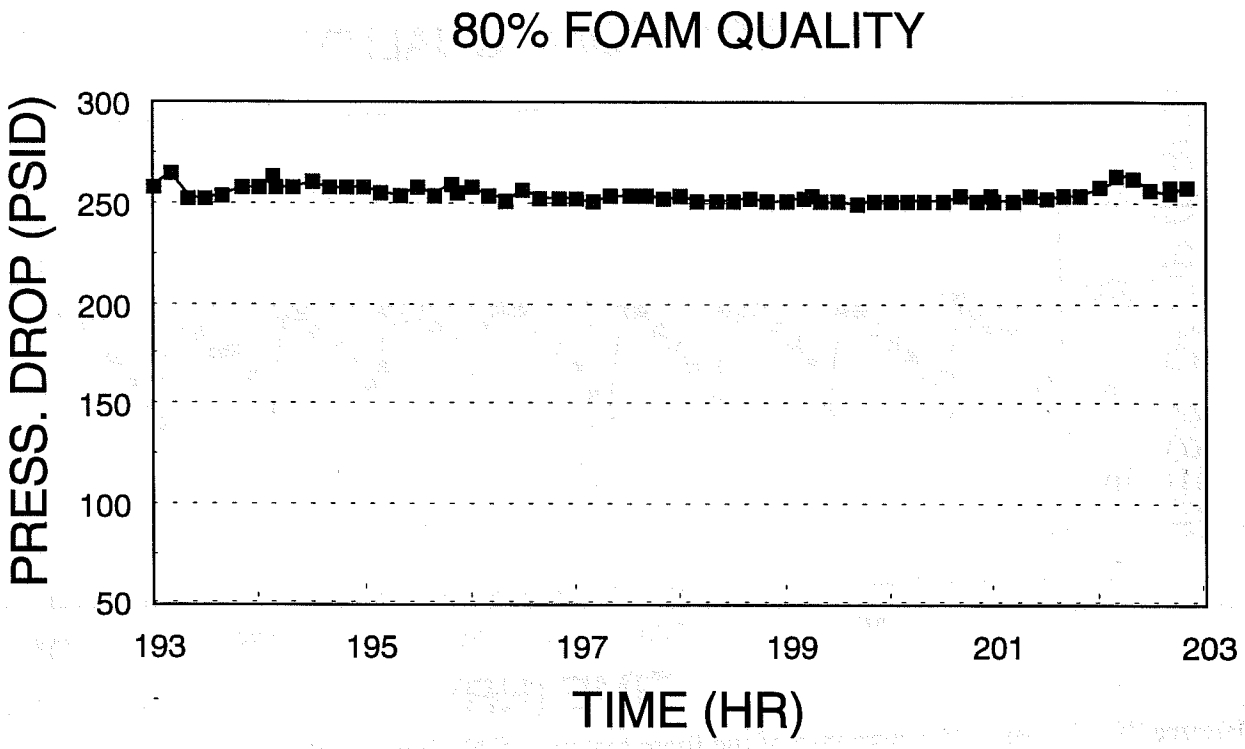

Figure 41. Pressure drop response of the foam test with 80% foam quality.

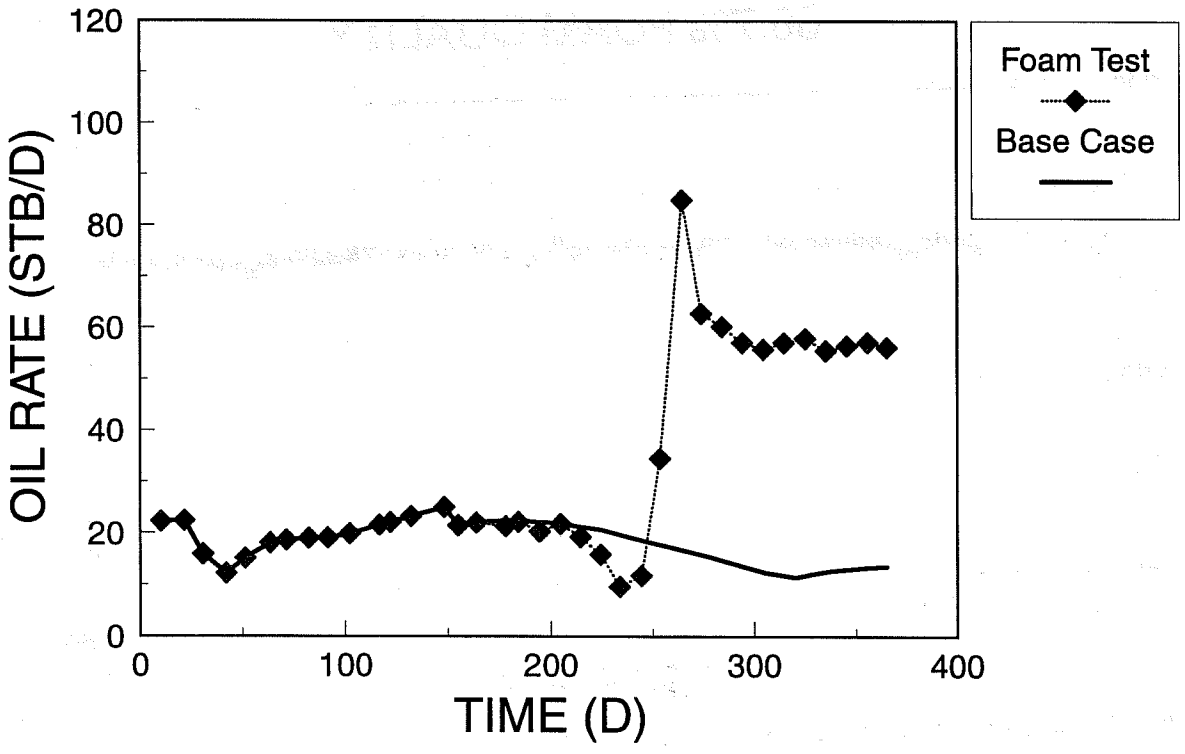

Figure 42. Comparison of oil rate history for problem I.

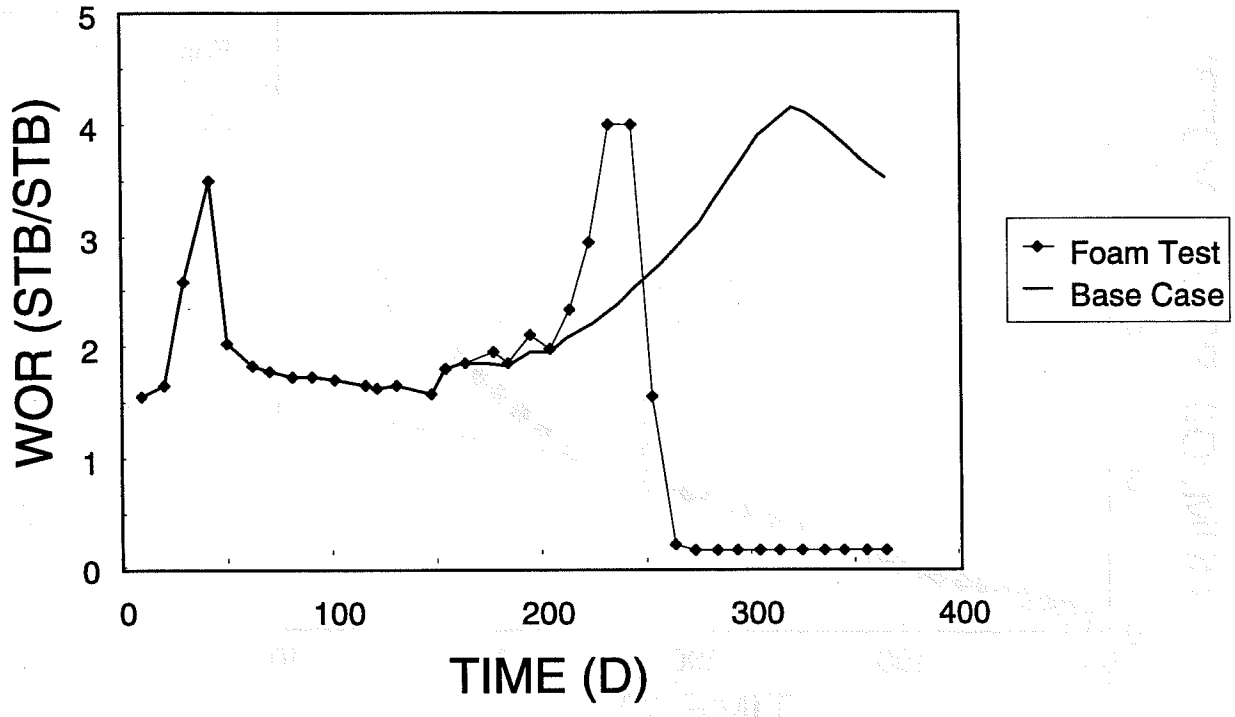

Figure 43. Comparison of gas-oil ratio for problem I.

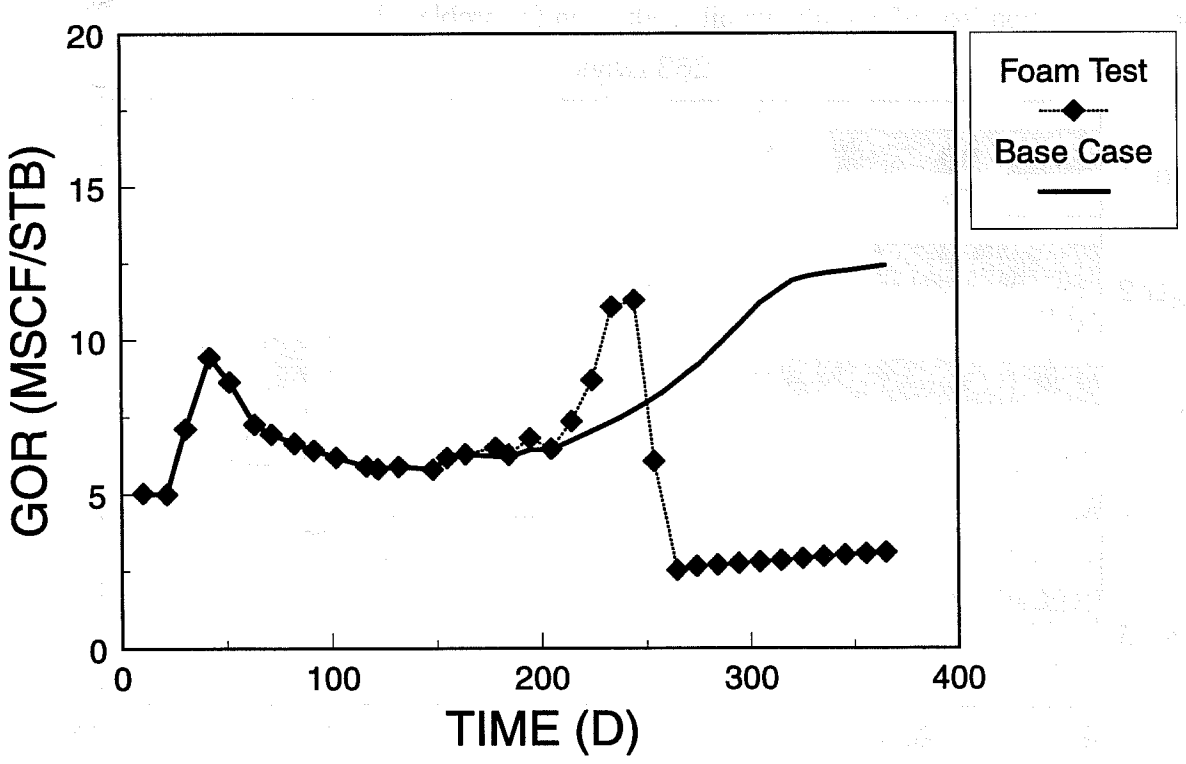

Figure 44. Comparison of water-oil ratio for problem I.

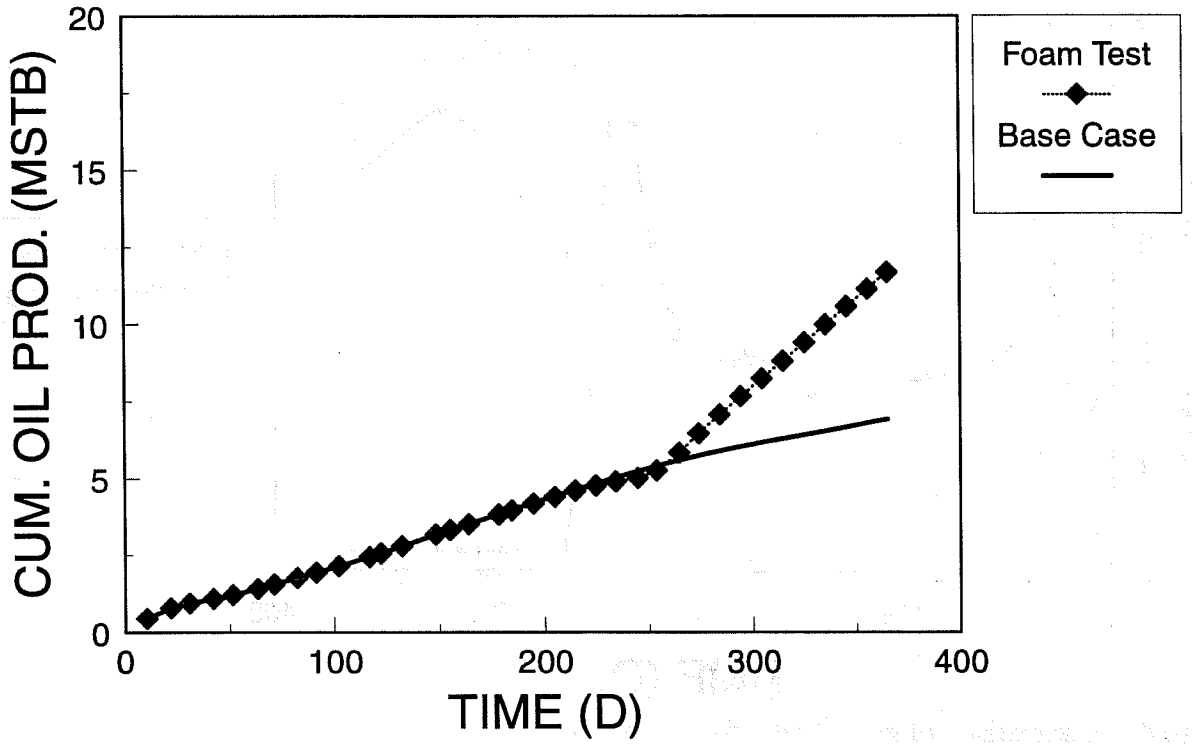

Figure 45. Comparison of cumulative oil production for problem I.

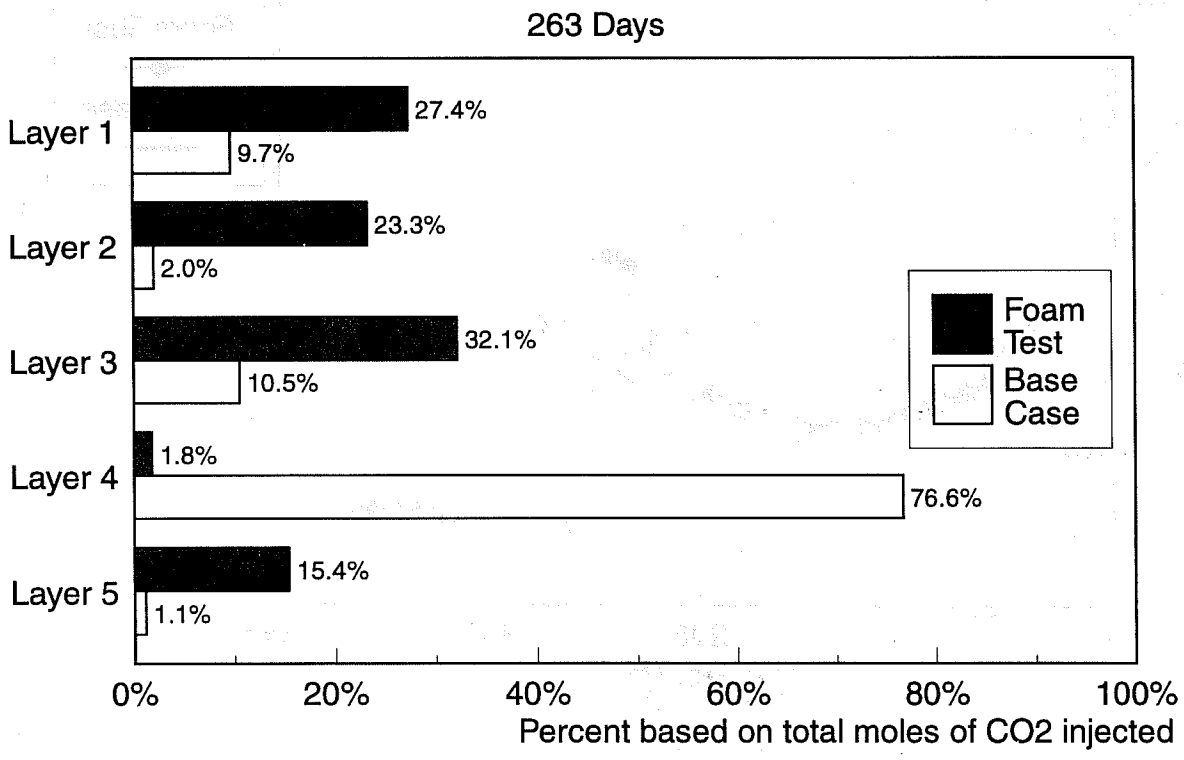

Figure 46. Comparison of CO_2 injection profile at 263 days for problem I.

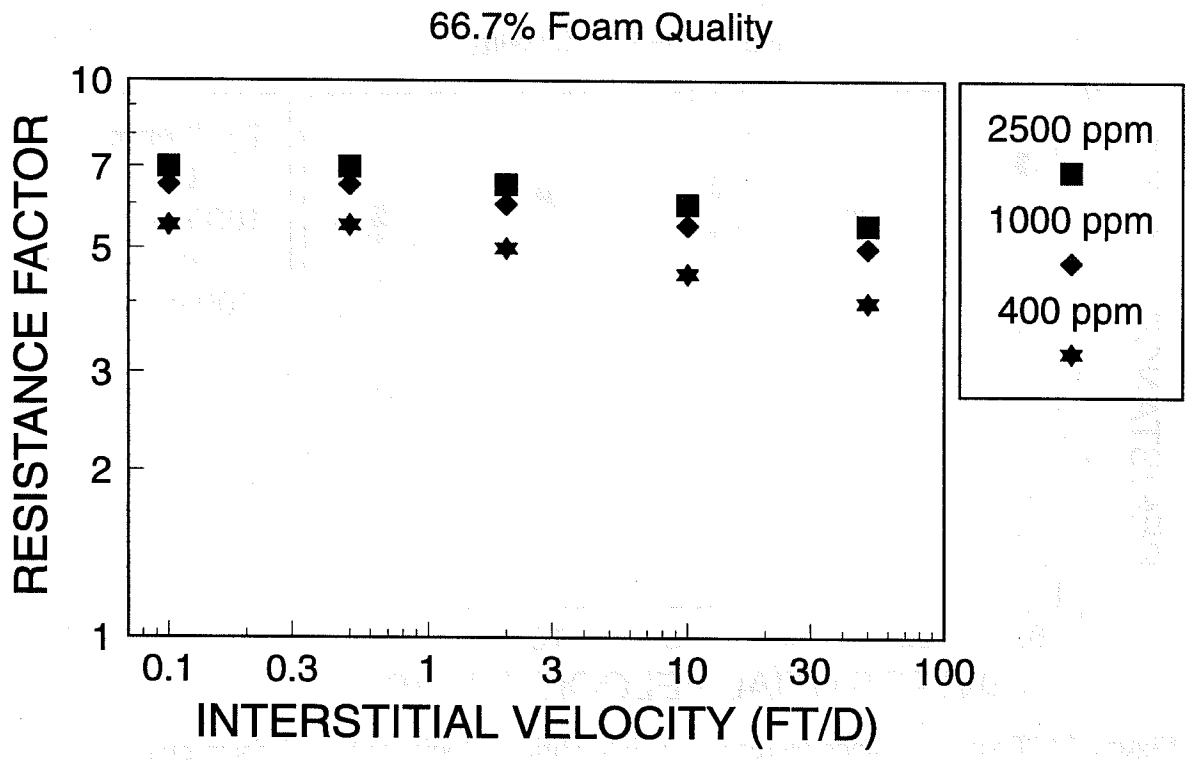

Figure 47. Foam resistance factor versus interstitial velocity at 66.7% foam quality and different surfactant concentrations.

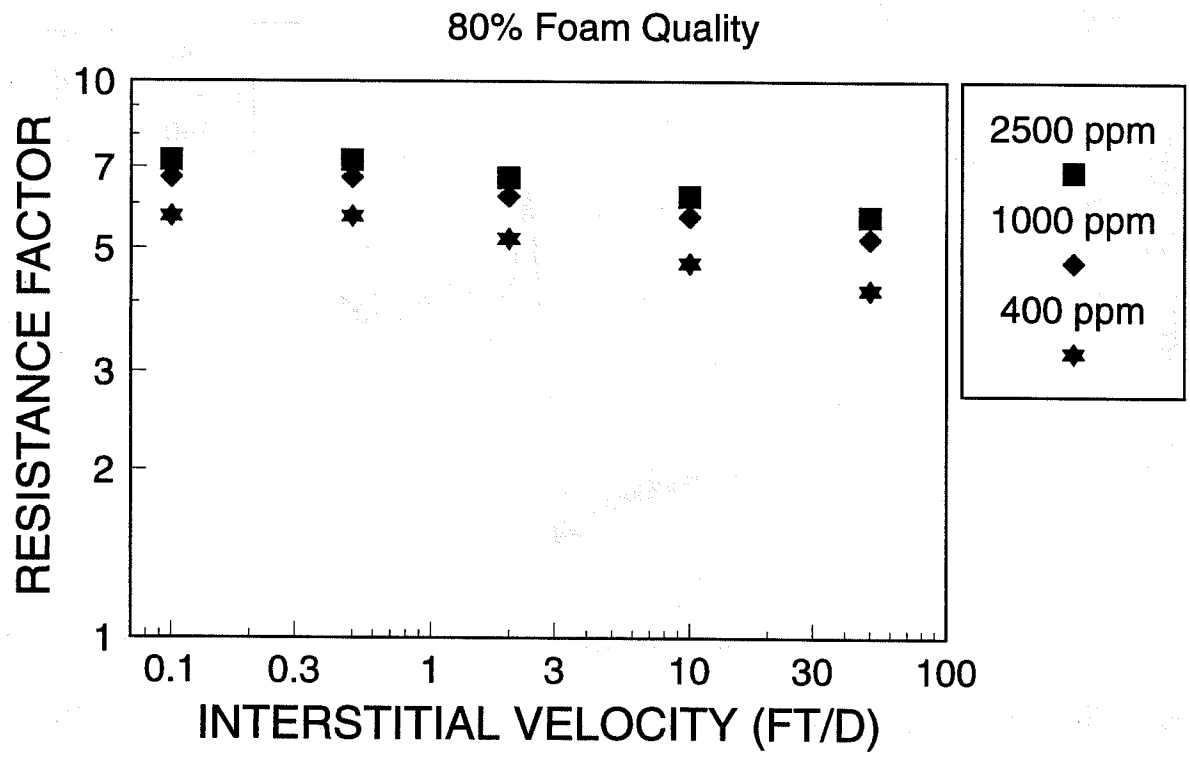

Figure 48. Foam resistance factor versus interstitial velocity at 80% foam quality and different surfactant concentrations.

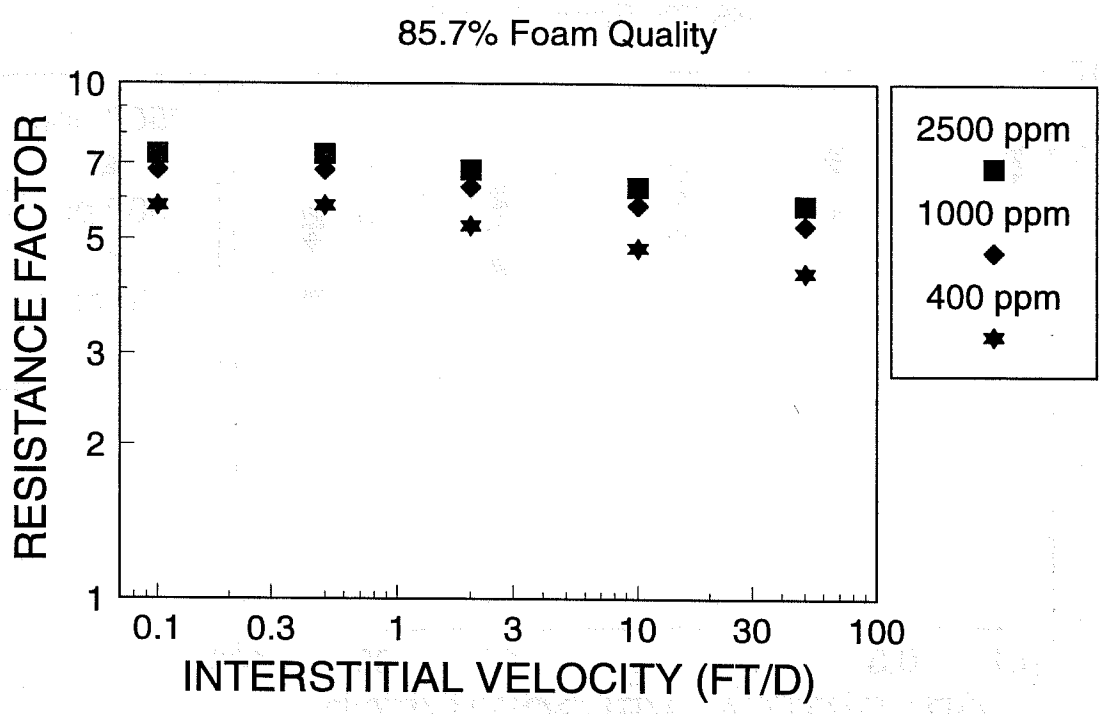

Figure 49. Foam resistance factor versus interstitial velocity at 85.7% foam quality and different surfactant concentrations.

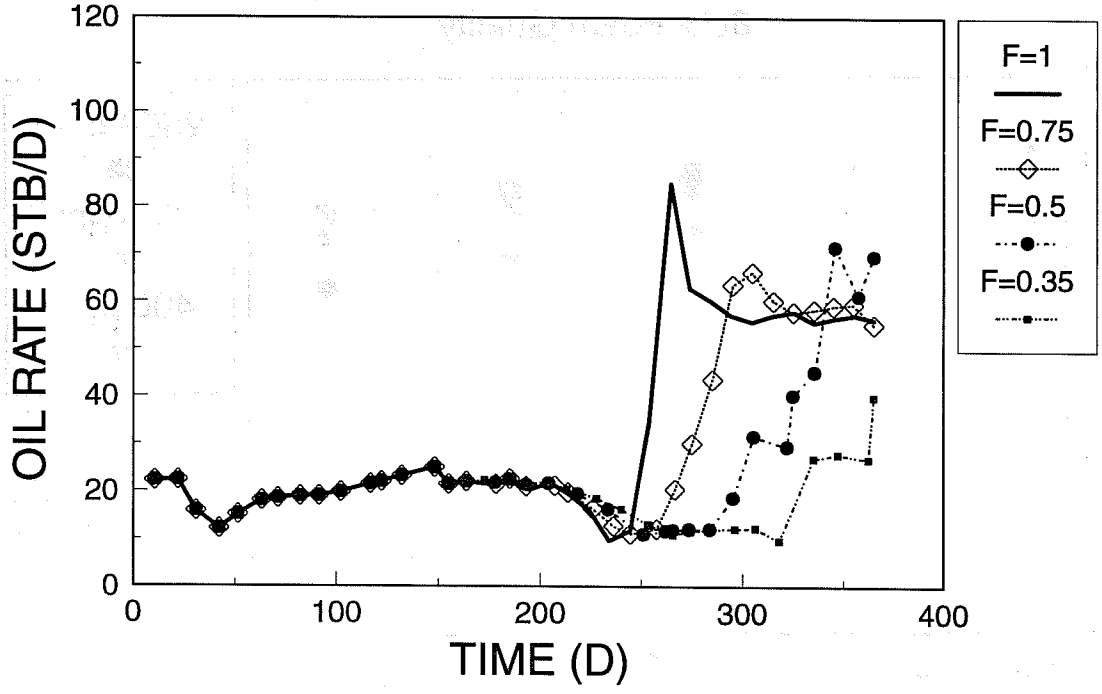

Figure 50. Effect of scaling parameter F on oil rate response for problem I.

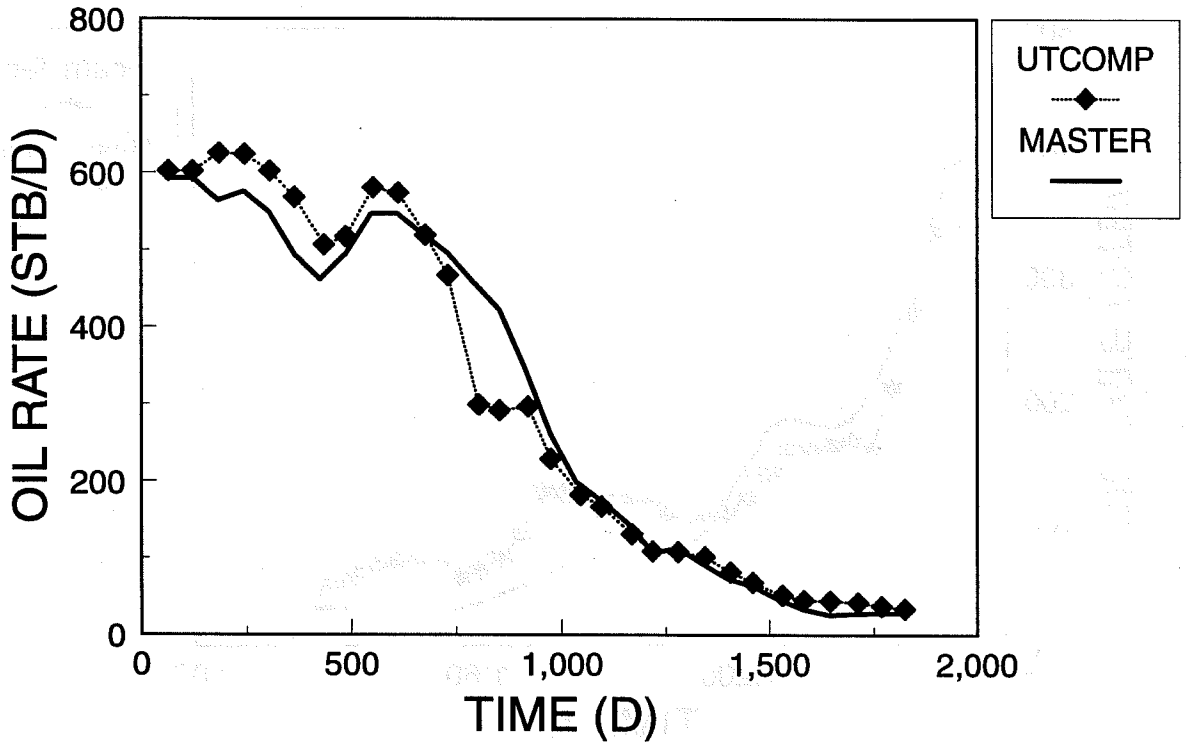

Figure 51. Comparison of oil rate history between UTCOMP and MASTER for problem II.

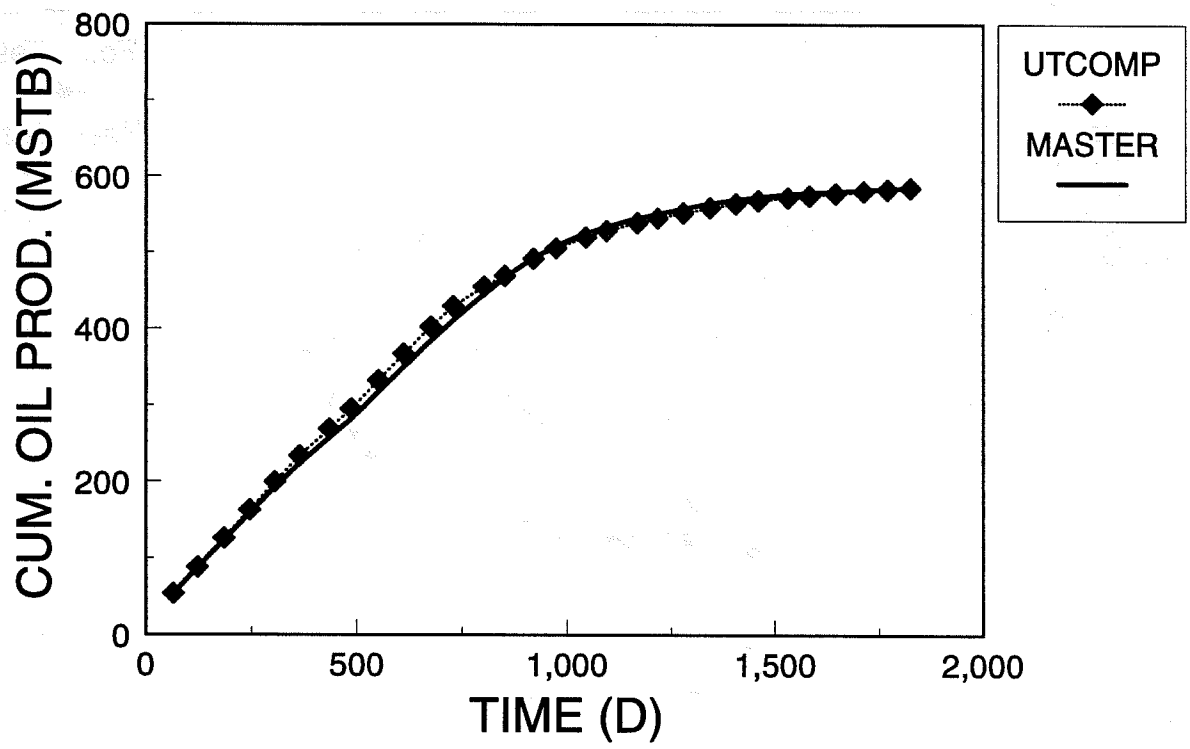

Figure 52. Comparison of cumulative oil production between UTCOMP and MASTER for problem II.

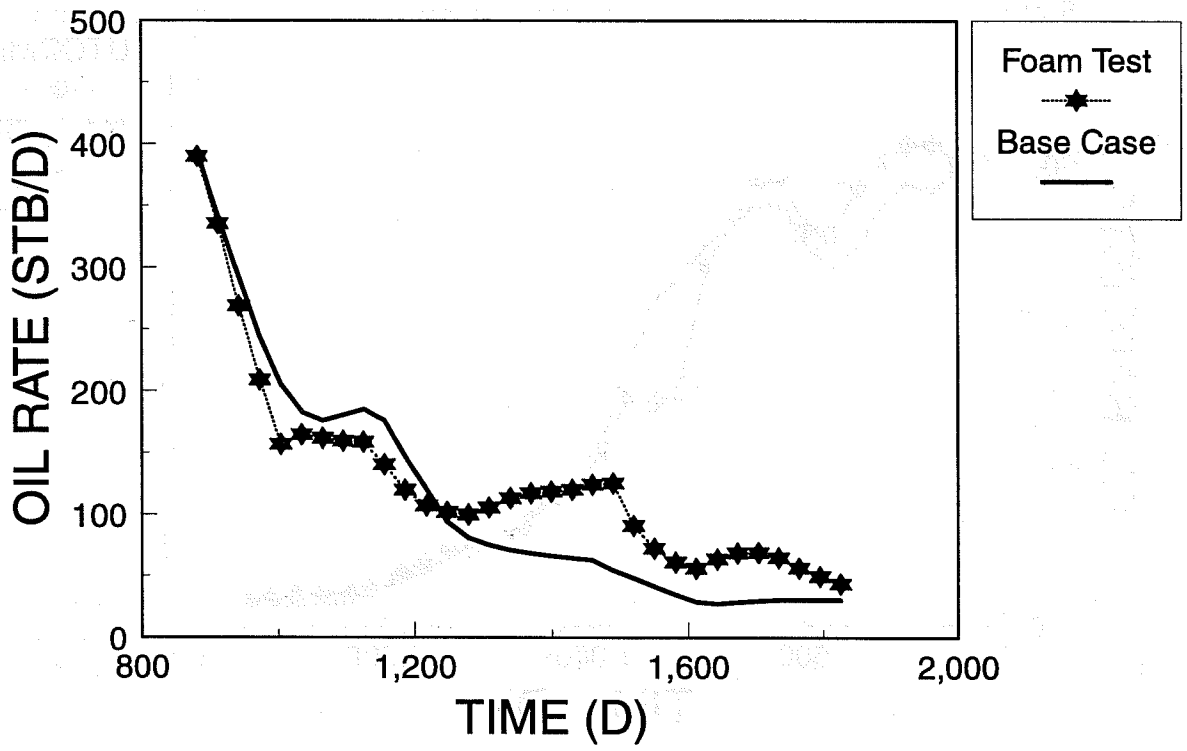

Figure 53. Comparison of oil rate history for problem III.

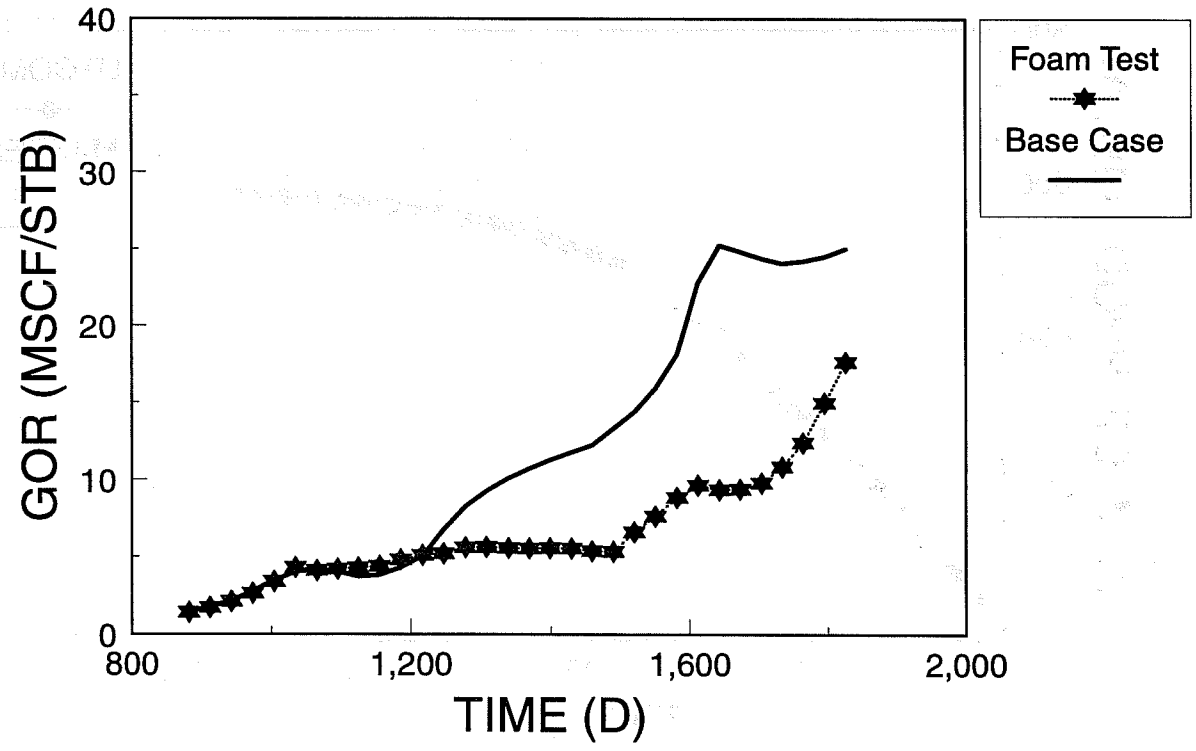

Figure 54. Comparison of gas-oil ratio for problem III.

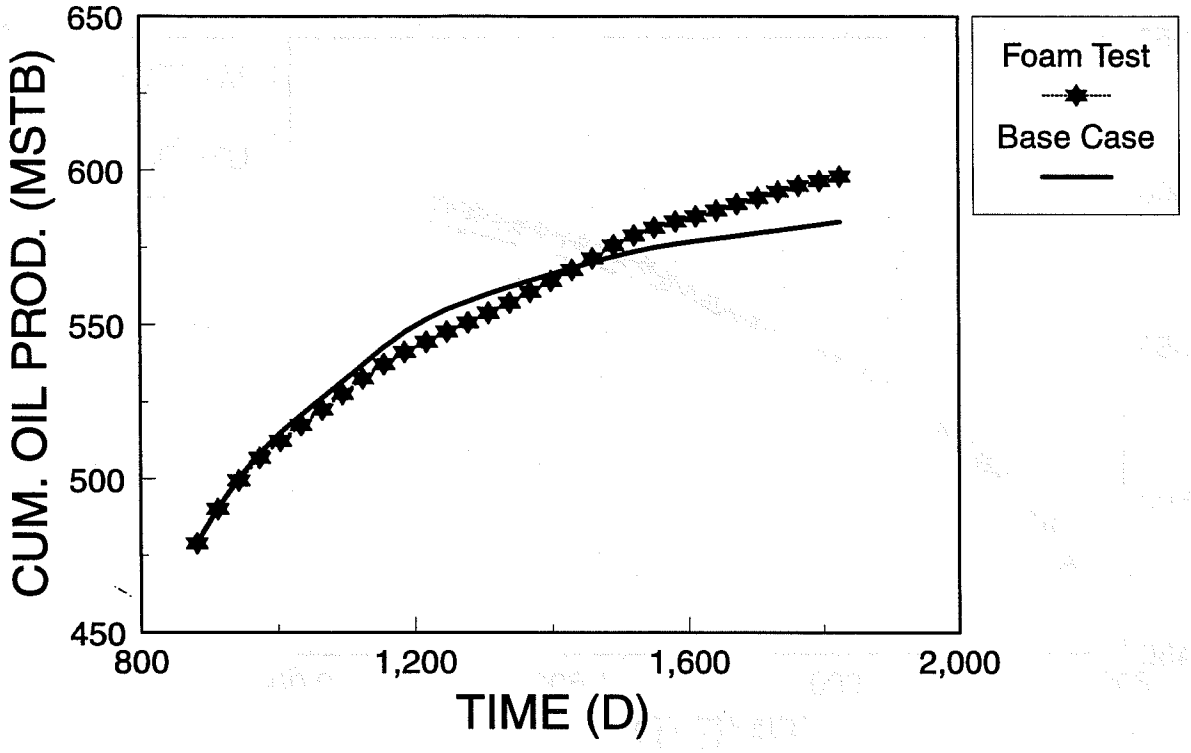

Figure 55. Comparison of cumulative oil production for problem III.

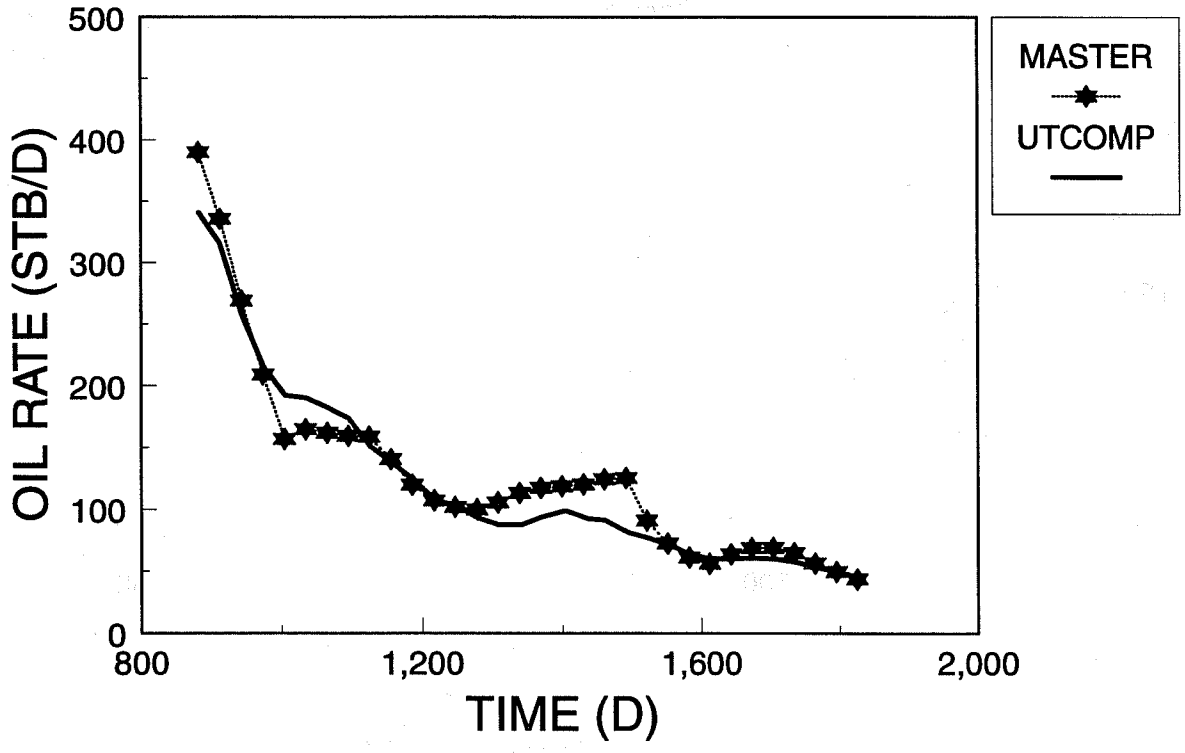

Figure 56. Comparison of oil rate history between MASTER and UTCOMP for problem III.

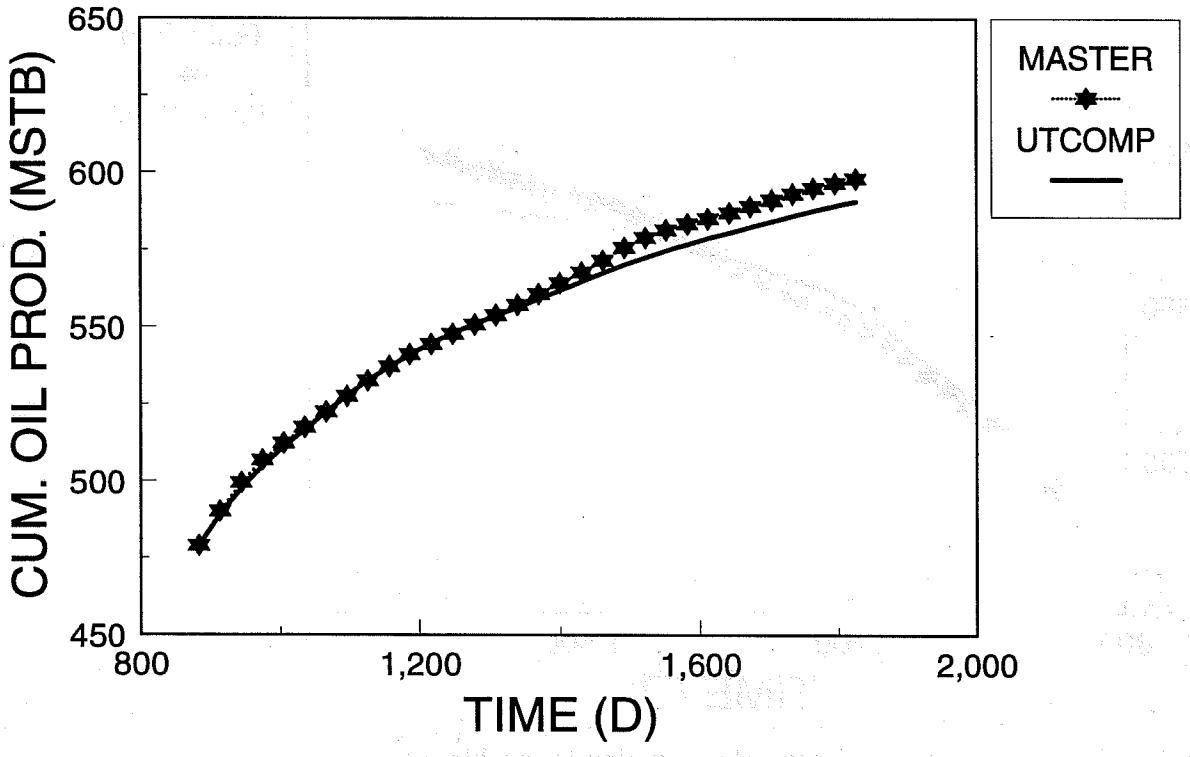

Figure 57. Comparison of cumulative oil production between MASTER and UTCOMP for problem III.

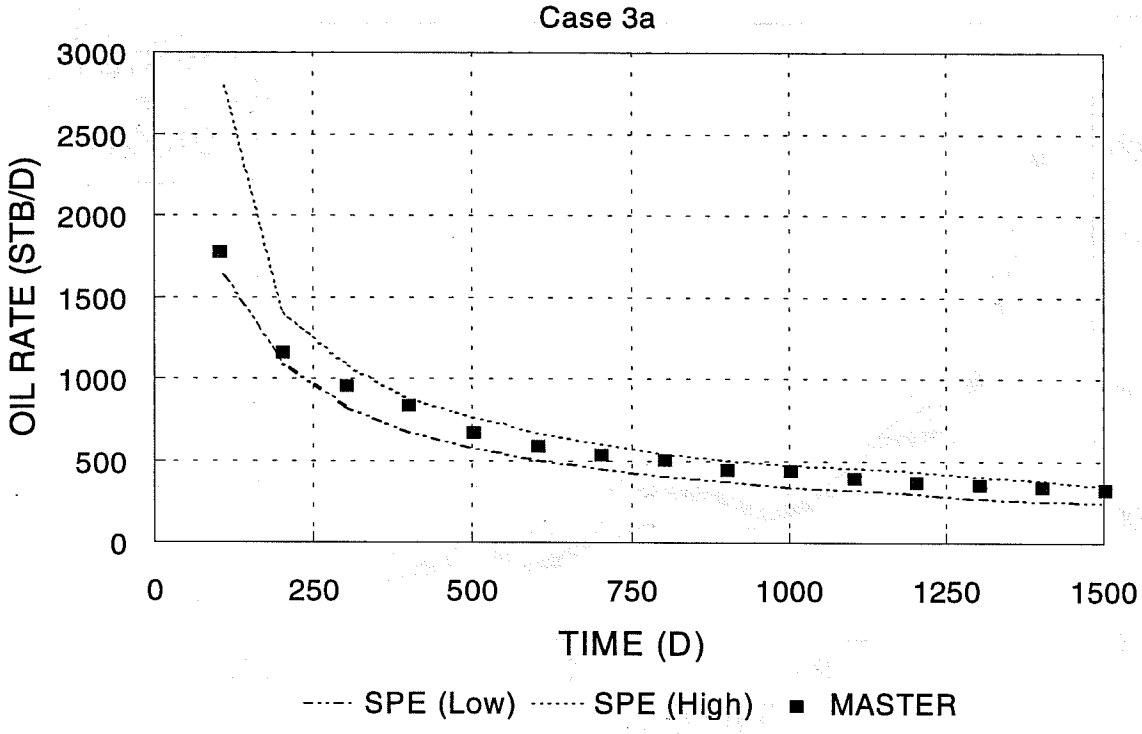

Figure 58. Comparison of oil rate history for case 3a of seventh SPE comparative solution project.

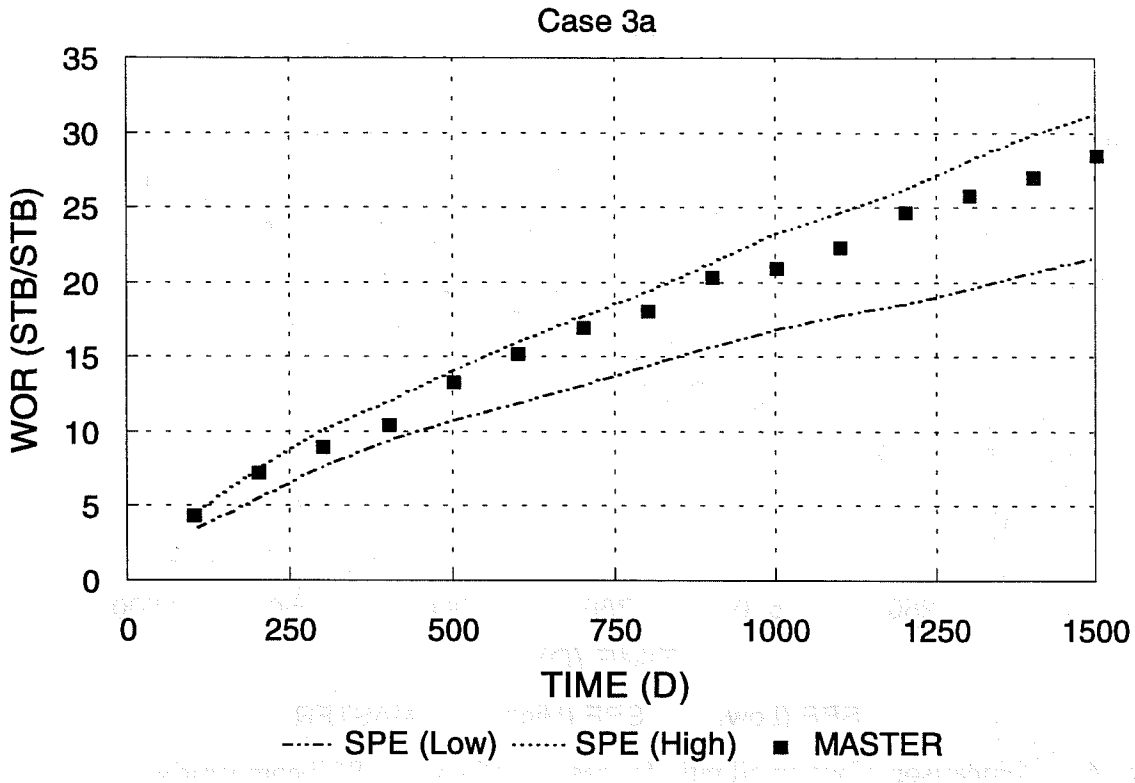

Figure 59. Comparison of water-oil ratio for case 3a of seventh SPE comparative solution project.

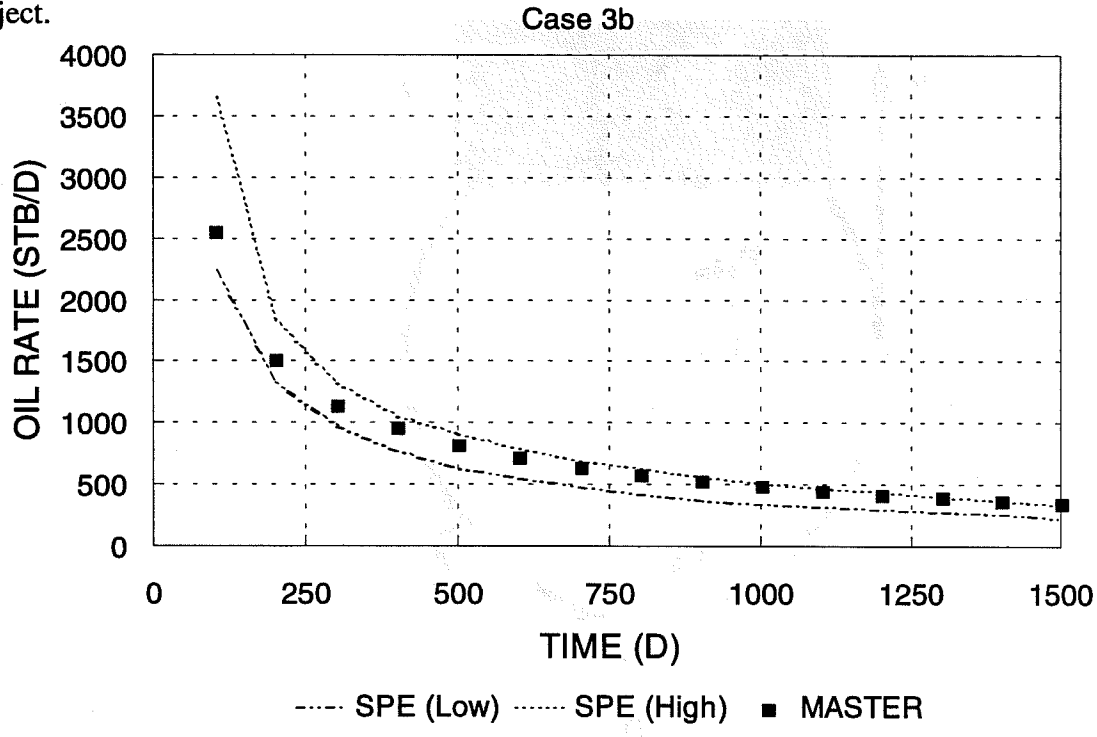

Figure 60. Comparison of oil rate history for case 3b of seventh SPE comparative solution project.

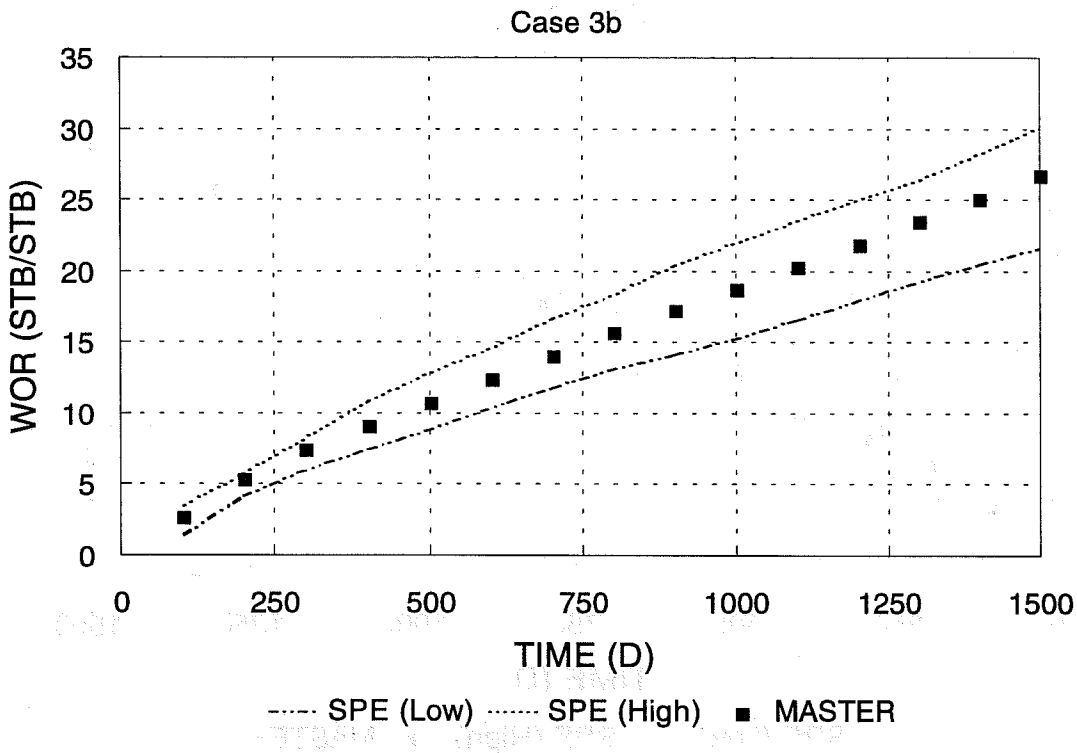

Figure 61. Comparison of water-oil ratio for case 3b of seventh SPE comparative solution project.

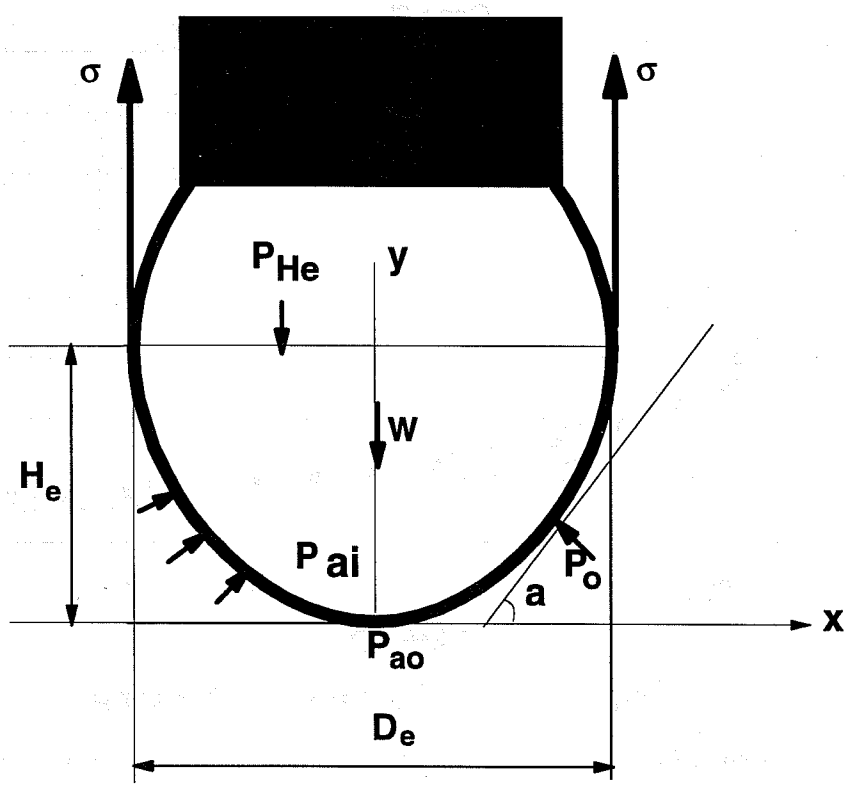

Figure 62. Geometry of a pendant drop.

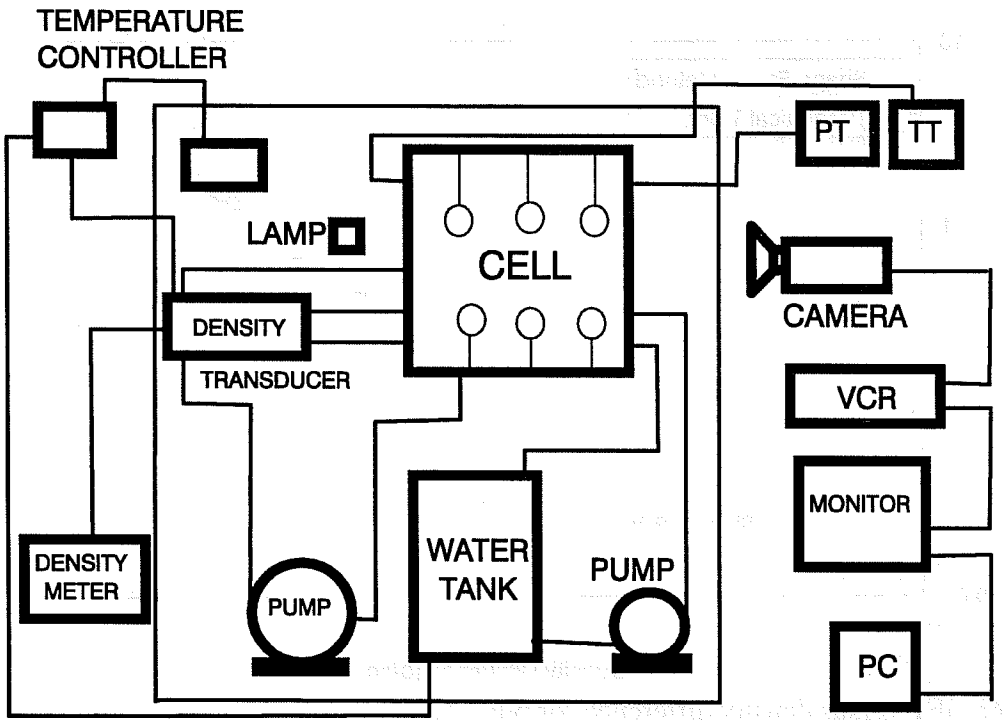

Figure 63. Sketch of pendant drop experimental setup.

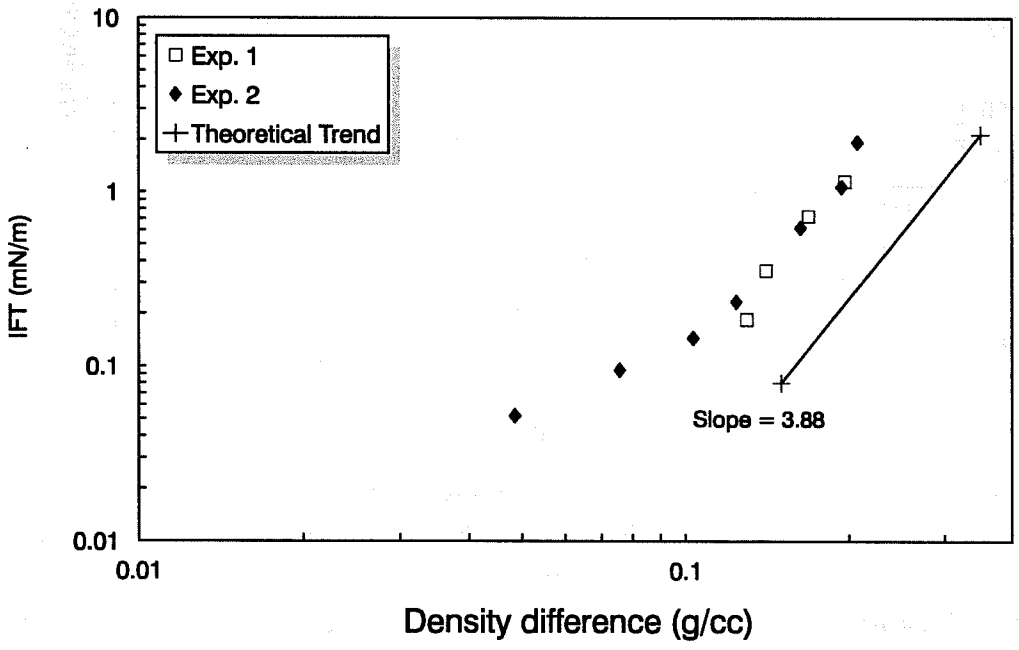

Figure 64. Measured IFT for brine/heptane/alcohol system.

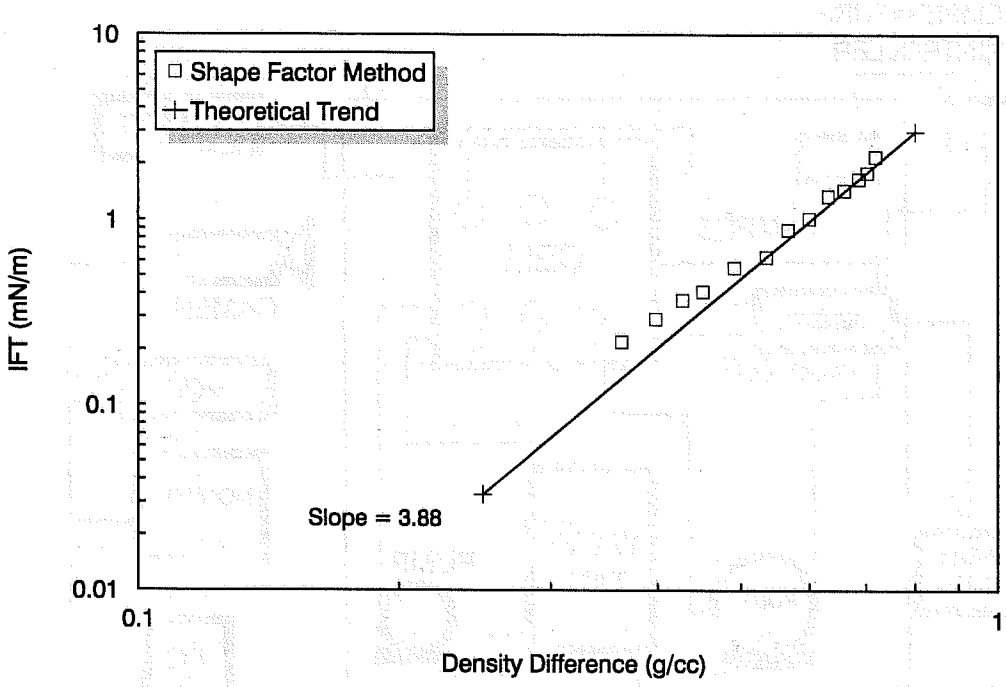

Figure 65. IFT versus density difference for pure CO_2.

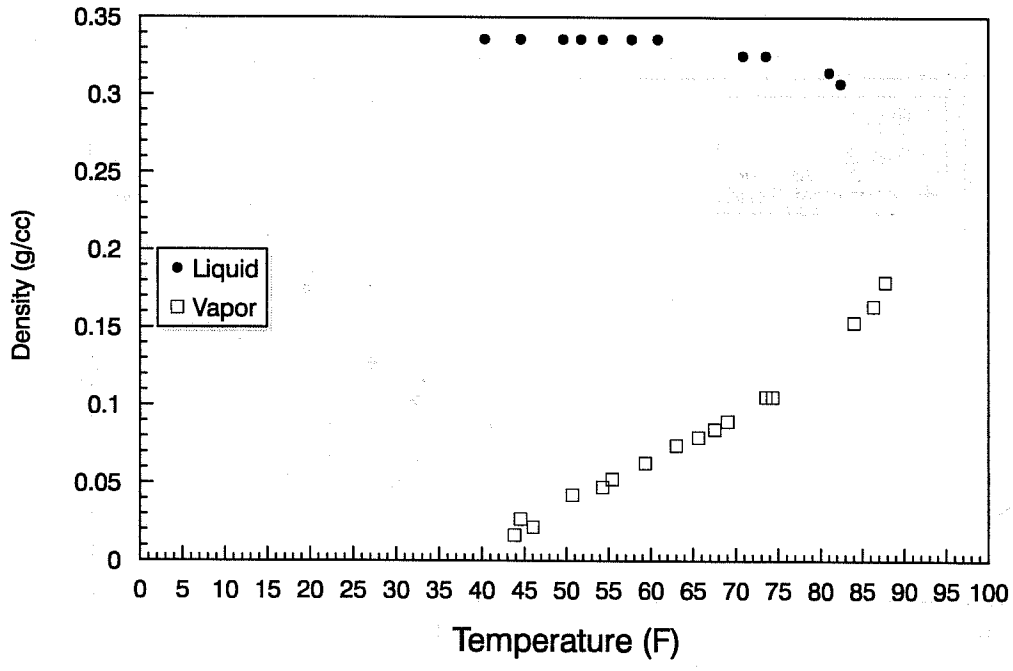

Figure 66. Measured ethane densities.

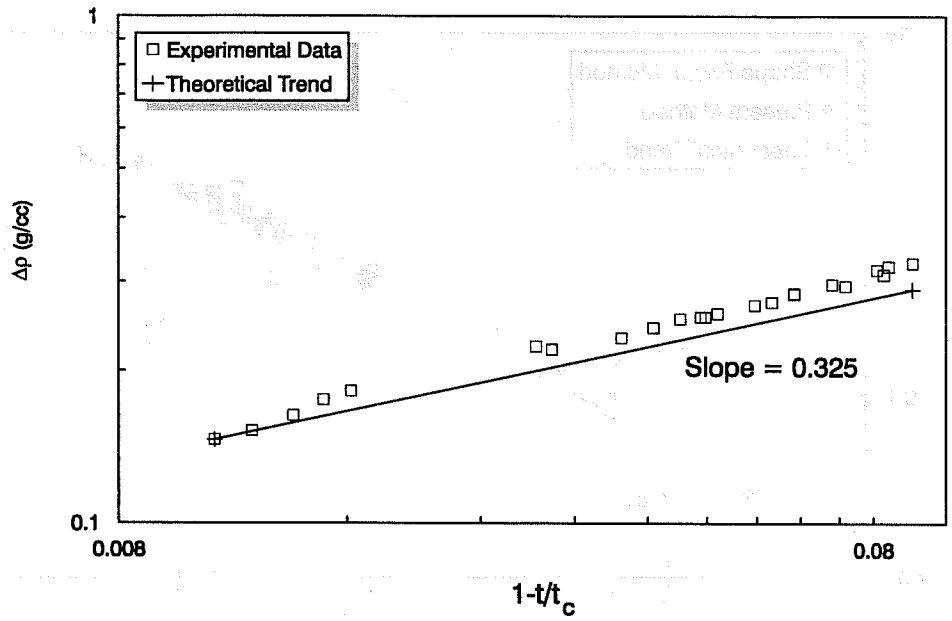

Figure 67. Surface Tension versus reduced temperature for ethane.

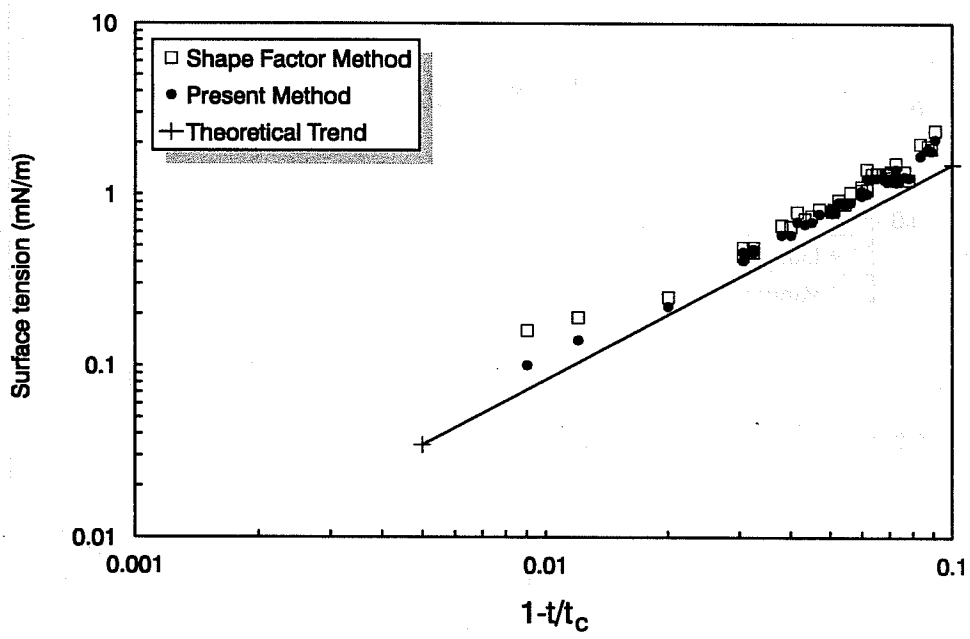

Figure 68. Density difference of ethane versus reduced temperature.

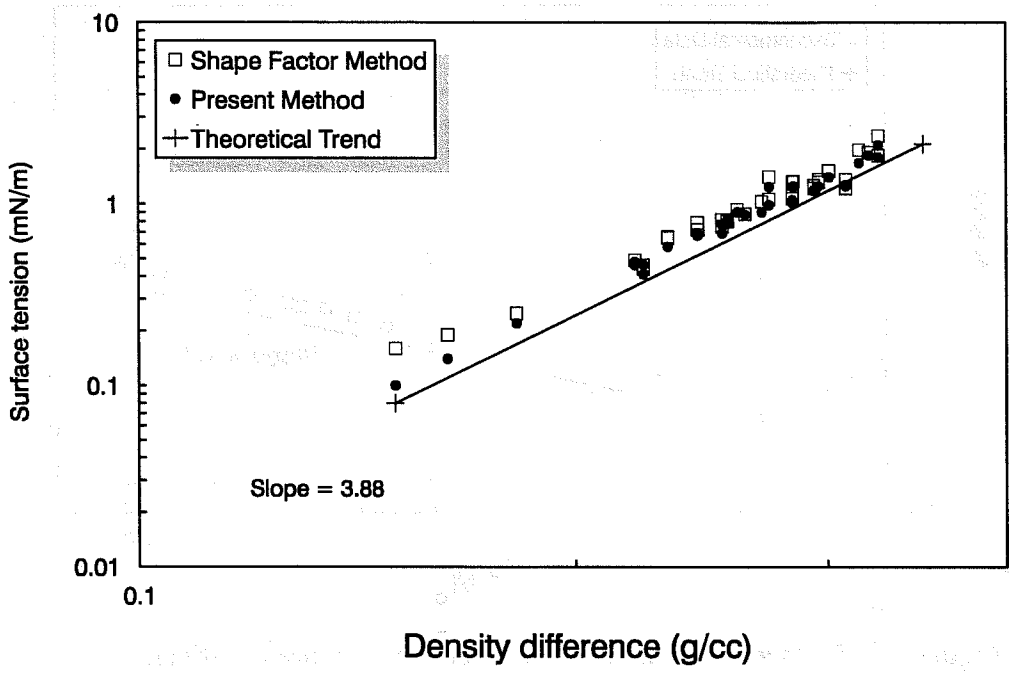

Figure 69. Surface tension versus density difference for ethane.

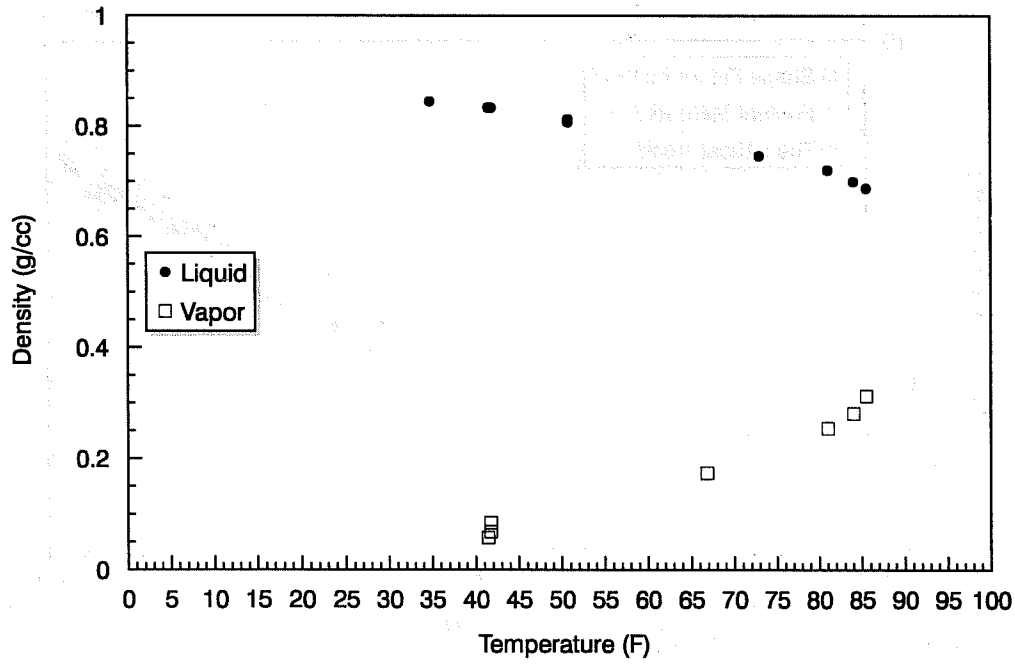

Figure 70. Measured phase densities for CO_2.

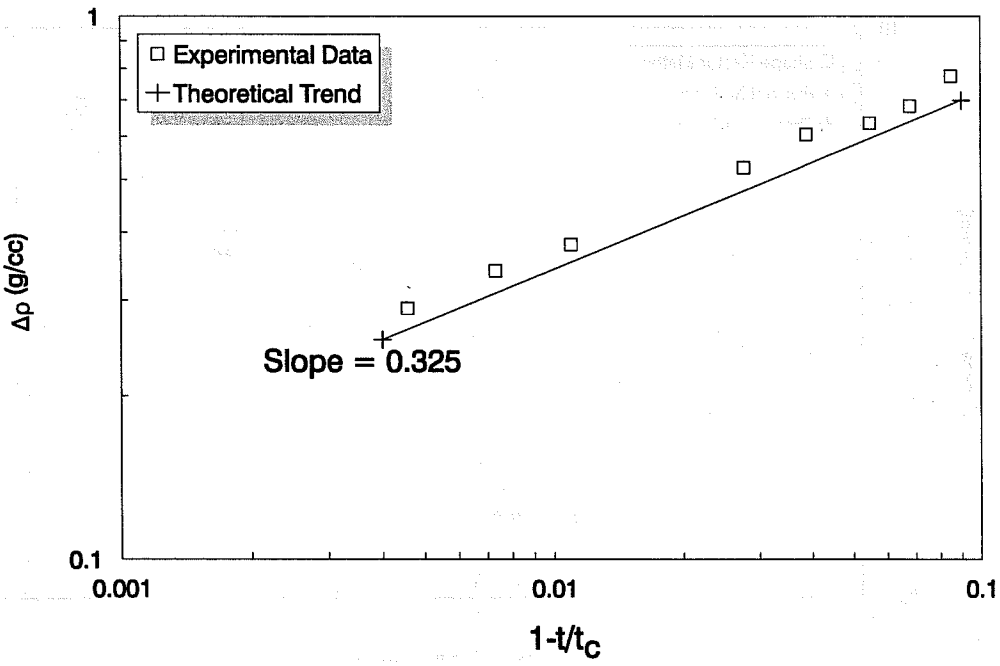

Figure 71. Density difference for CO_2 versus reduced temperature.

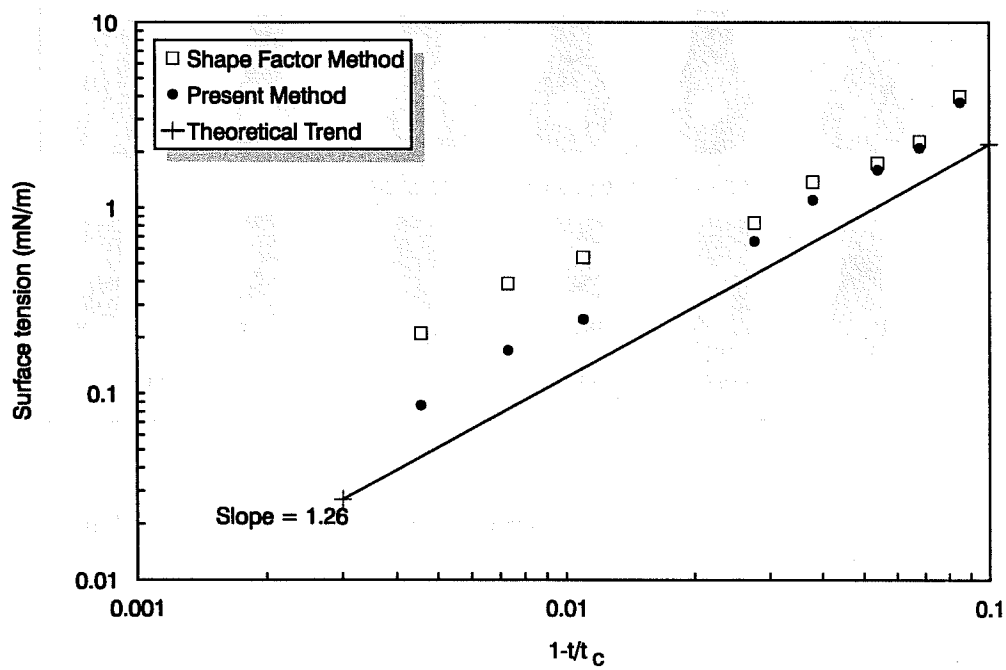

Figure 72. Surface tension versus reduced temperature for CO_2.

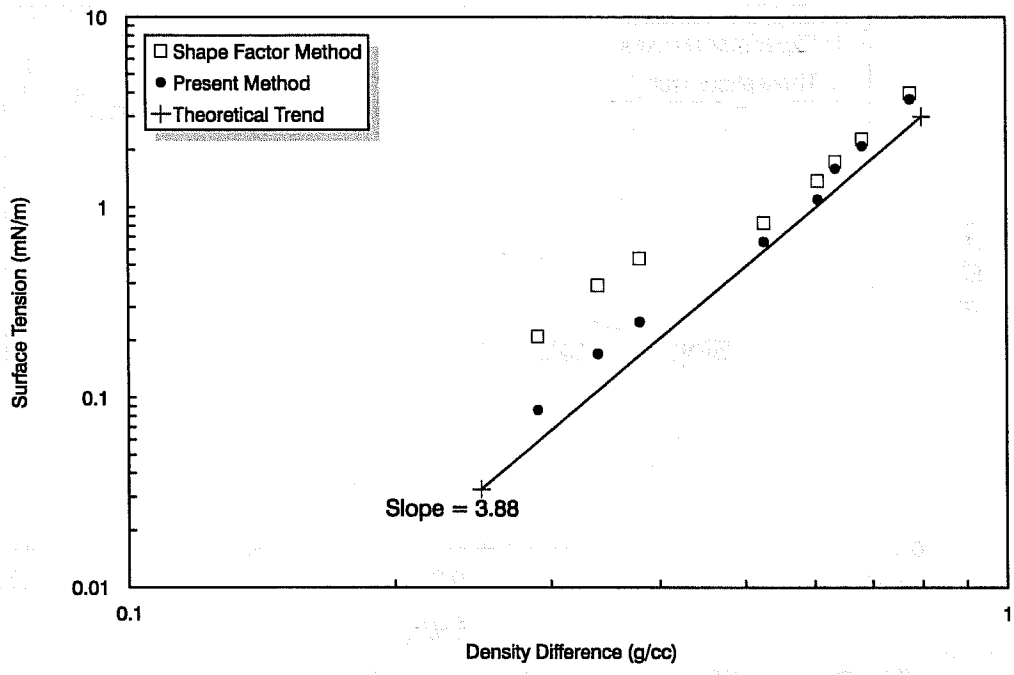

Figure 73. Surface tension versus density difference for CO_2.

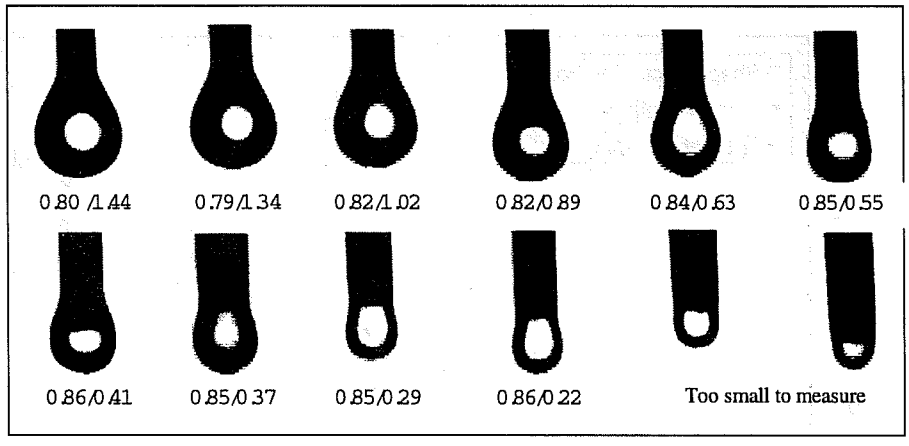

Figure 74. Shape factor/surface tension of pure CO_2 drops. Note change in shape as low IFT is attained.

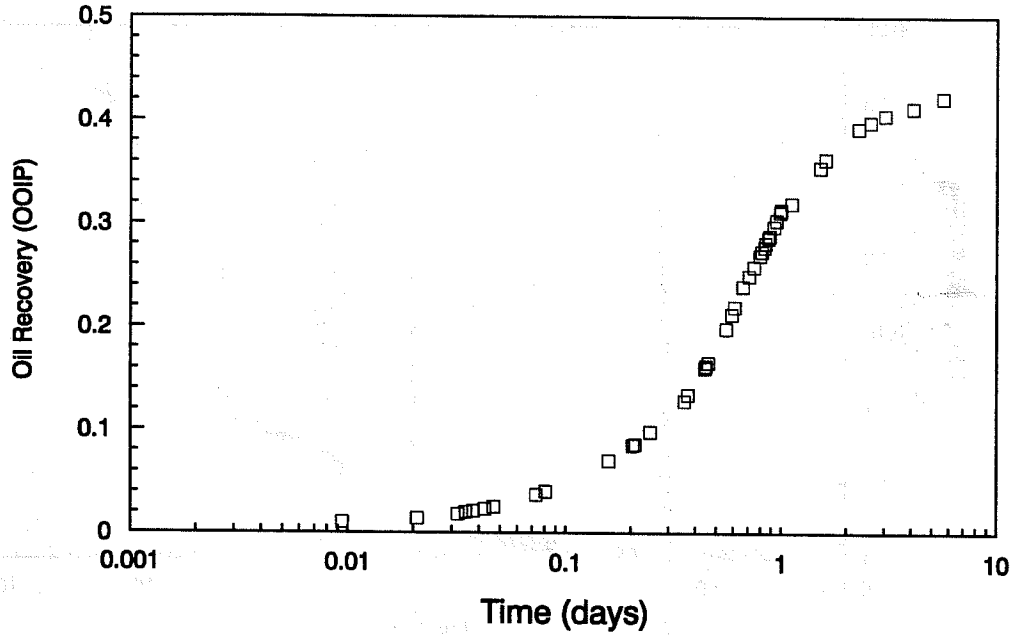

Figure 75. Oil recovery from a Berea core.

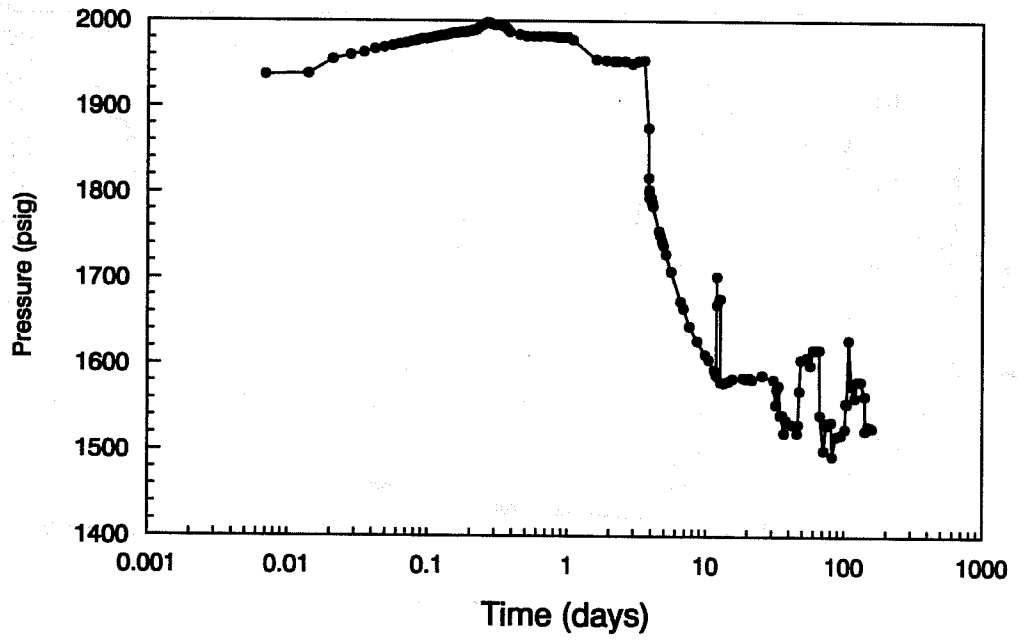

Figure 76. Pressure history for low permeability core experiment.

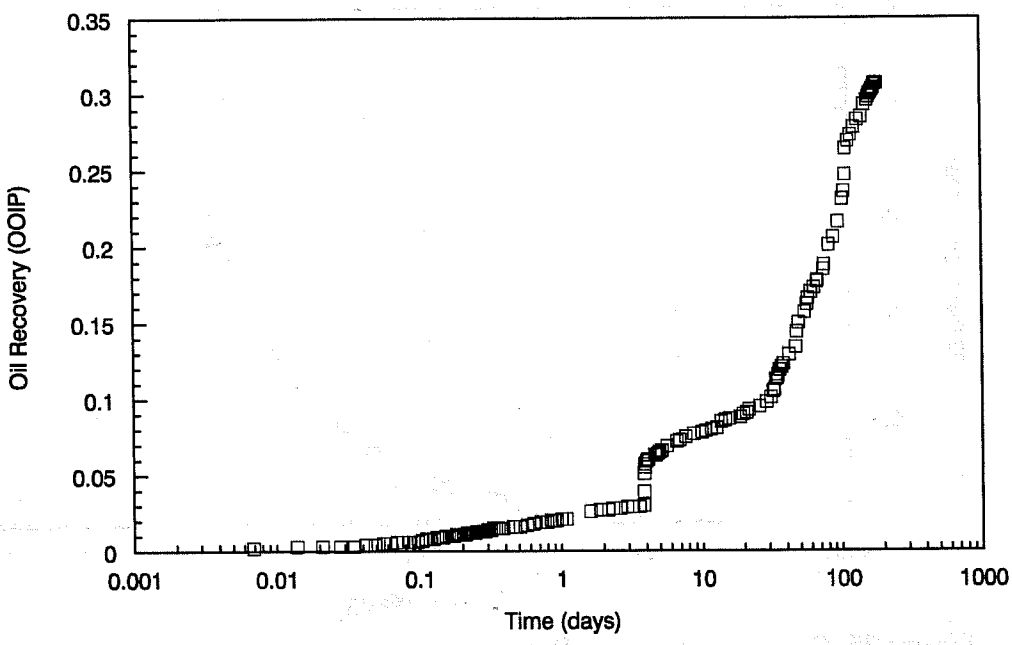

Figure 77. Oil recovery from a Spraberry core.

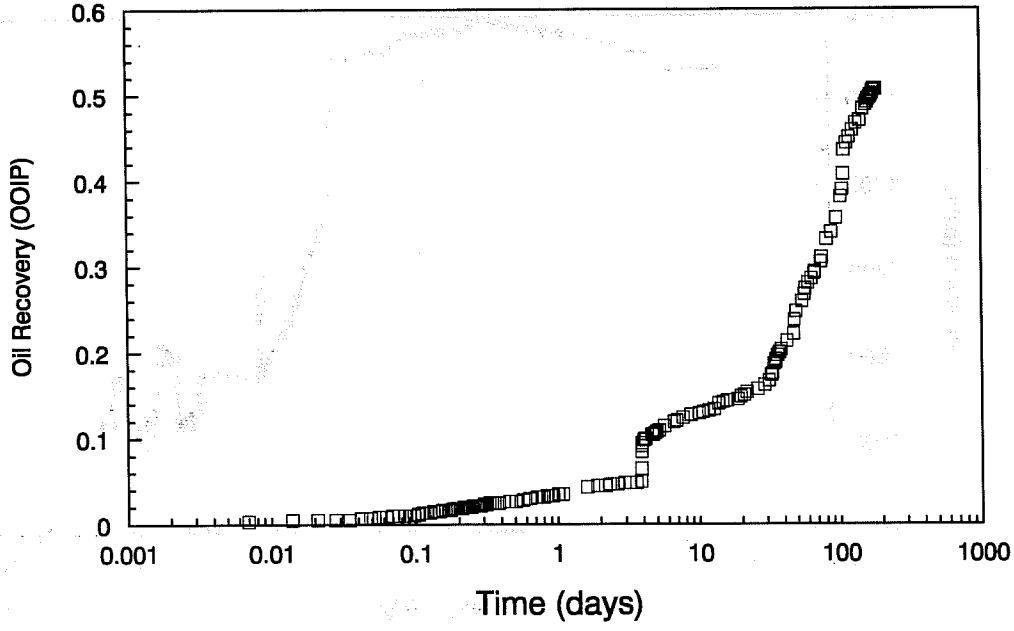

Figure 78. Corrected oil recovery from the Spraberry core.

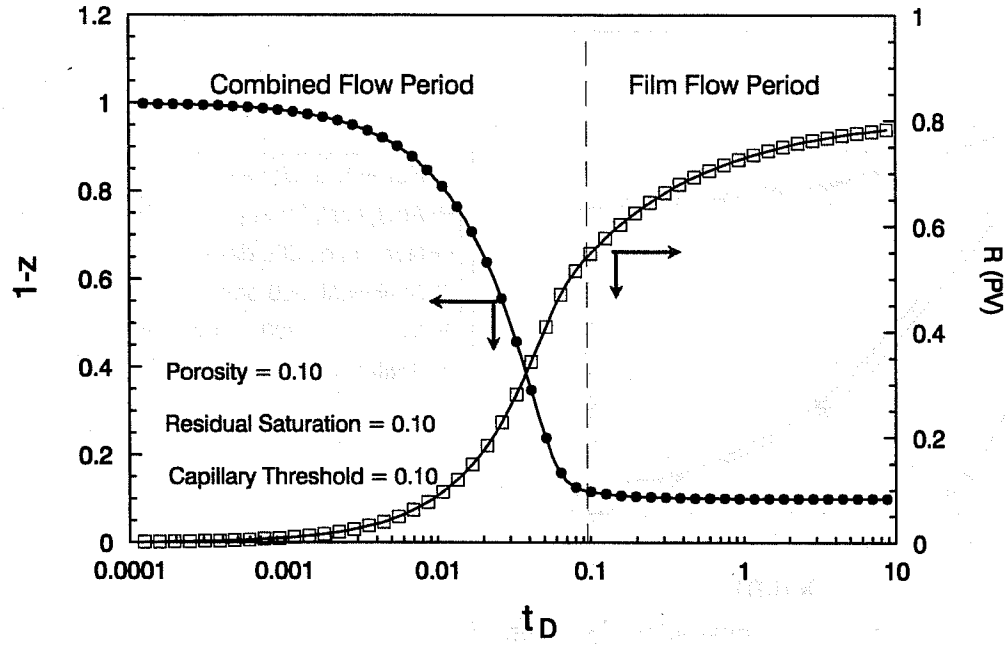

Figure 79. Solution to demarcator and recovery for Fs = 1.0.

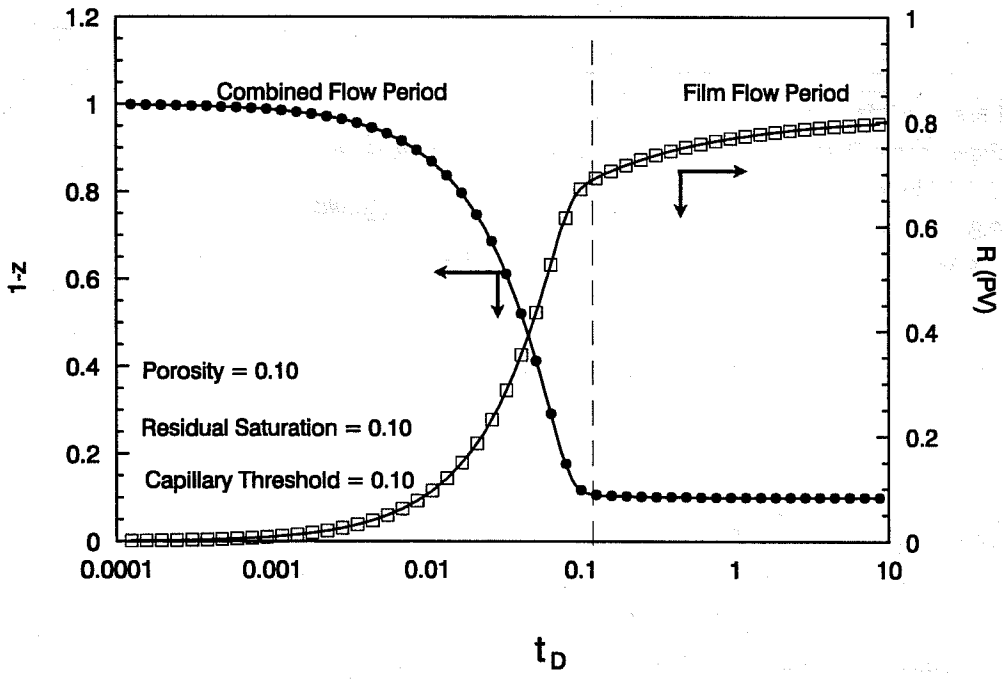

Figure 80. Solution to demarcator and recovery for Fs = 0.5.

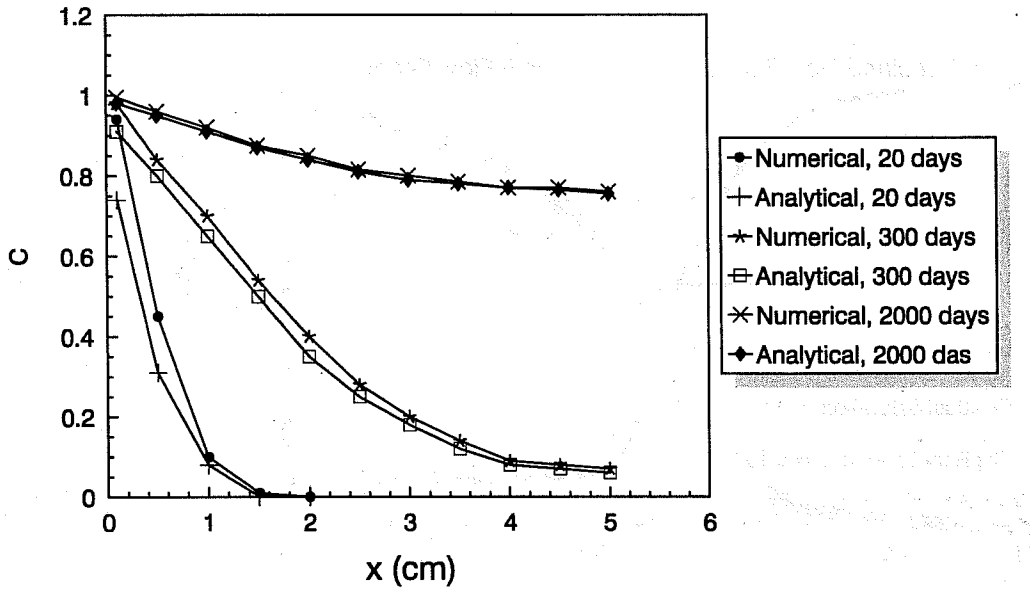

Figure 81. Model calculated dimensionless concentration.

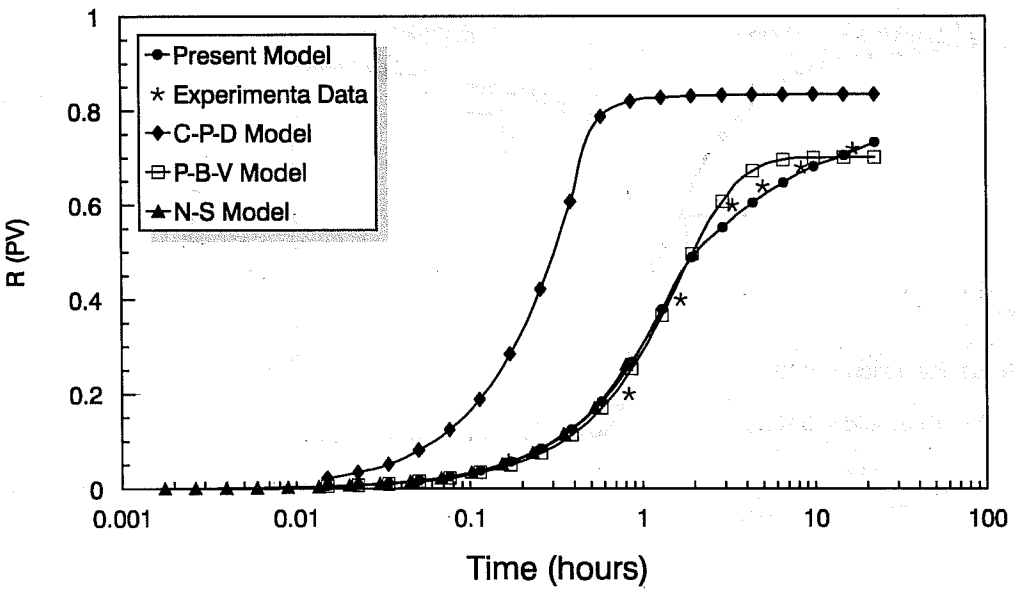

Figure 82. Comparison of calculated and observed oil recoveries.

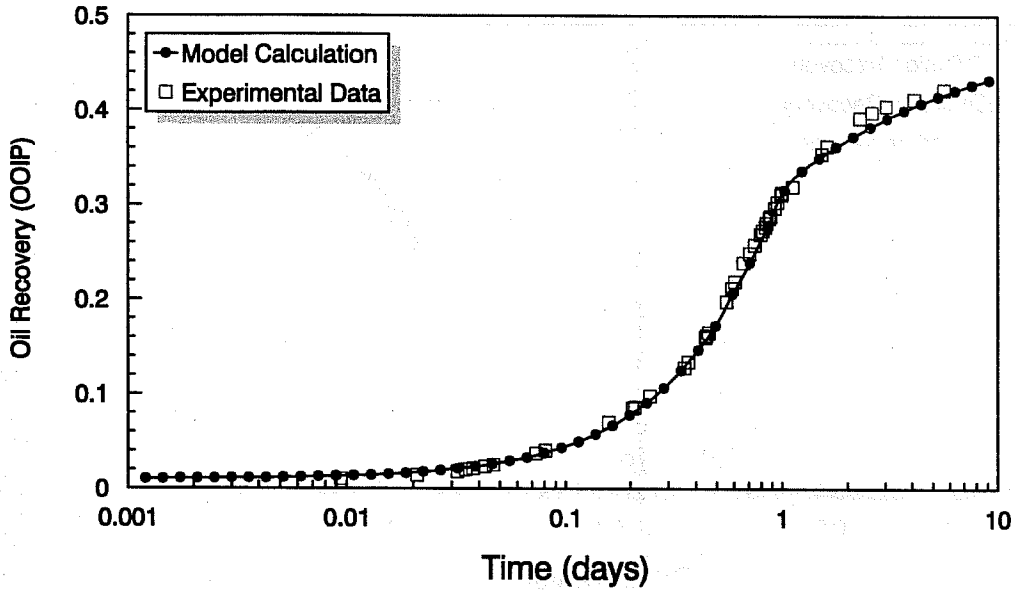

Figure 83. Matched and observed oil recoveries from Berea core.

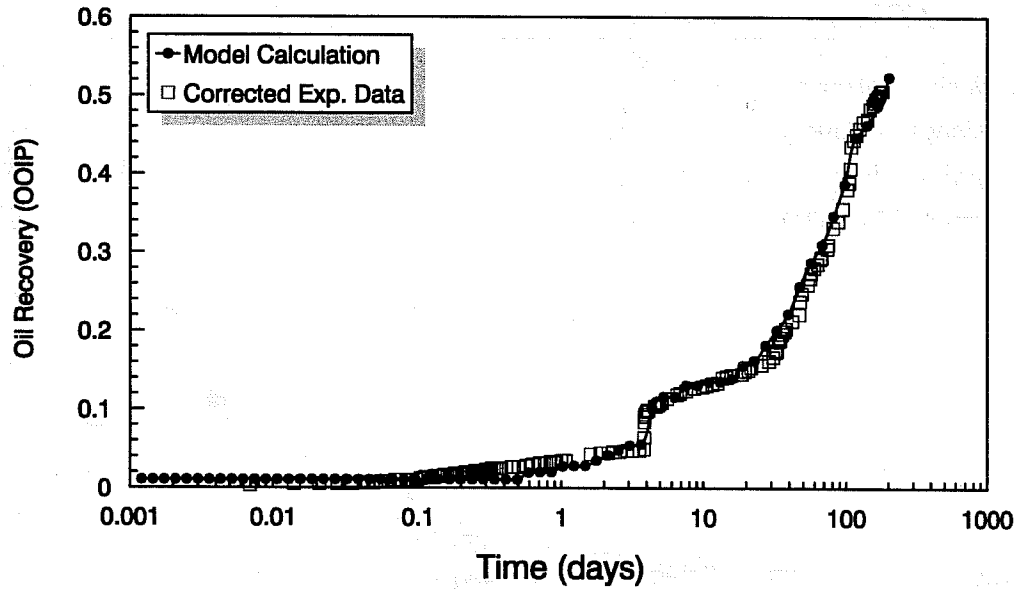

Figure 84. Matched and observed recoveries from a Spraberry core.

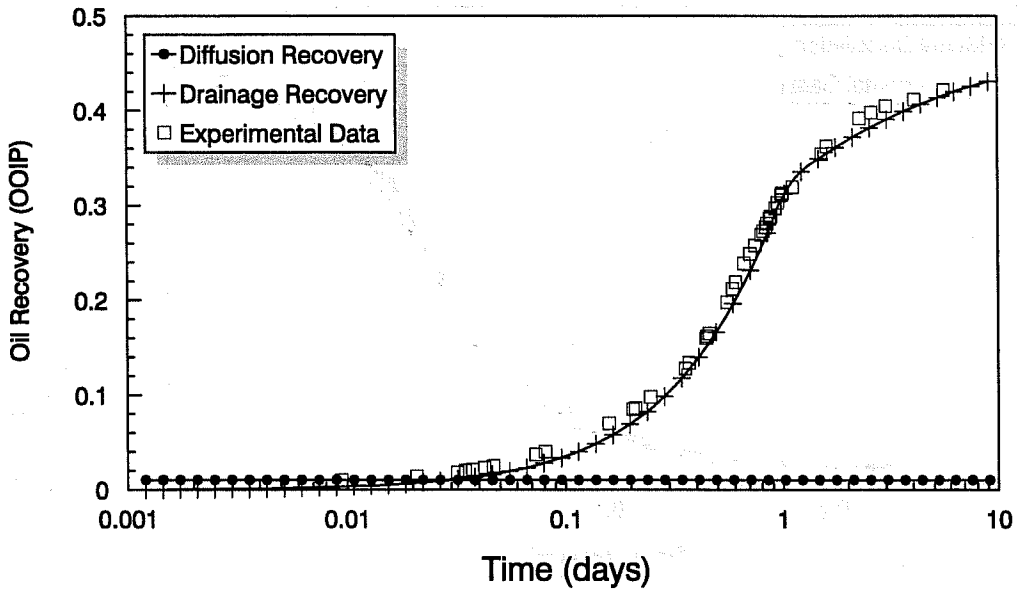

Figure 85. Calculated recovery components for Spraberry core.

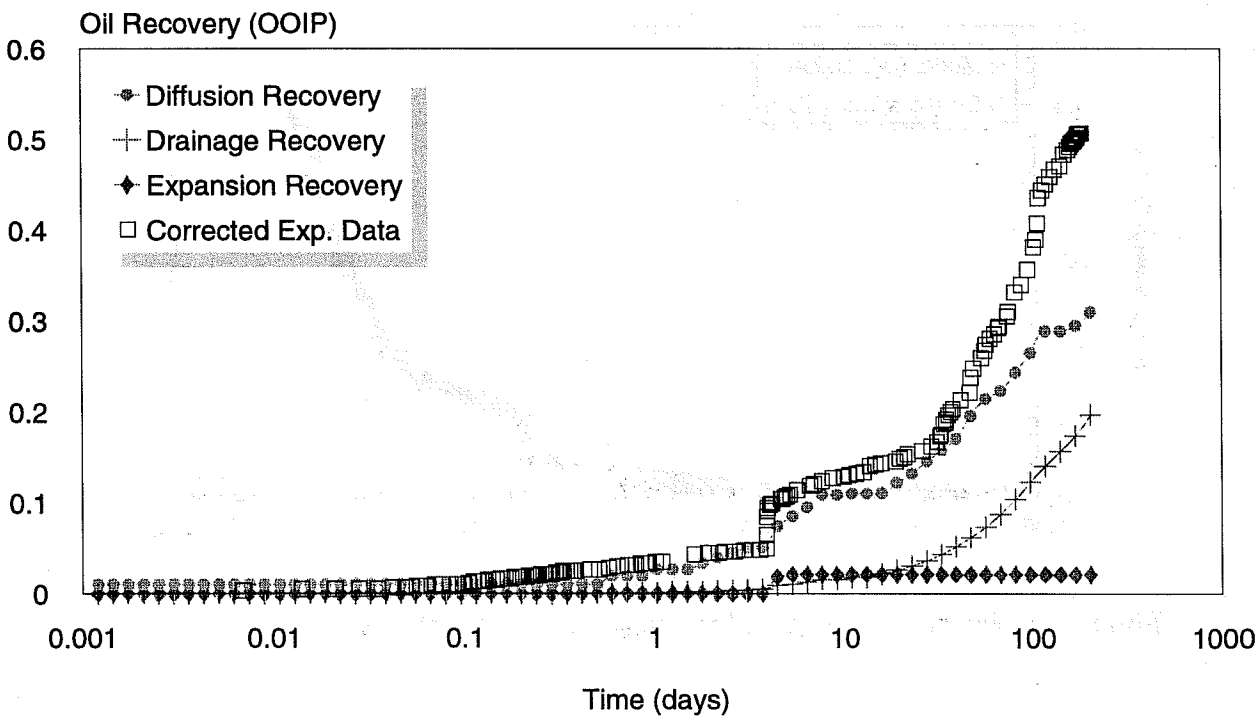

Figure 86. Calculated recovery components for Spraberry core.

CONCLUDING REMARKS

This second annual technical report on PRRC's current CO_2 project defines three specific tasks and describes the work that has been performed on them during the second year of the project covering April 14, 1995 to April 13, 1996. Each of the three tasks is directed towards solving a particular problem encountered in CO_2 flooding, the solutions to which will make possible more efficient oil recovery from fields which are amenable to production enhancement by high-pressure CO_2 injection, especially heterogeneous reservoirs.

The report is divided into three sections, each of which covers in detail the work performed on the corresponding task. In each case vital introductory material is covered, as well as technical descriptions of progress that is of importance to the domestic oil industry. The results of this project will be directly implemented into ongoing and planned field work.

ACKNOWLEDGMENTS

It is a pleasure to acknowledge financial assistance from the U.S. Department of Energy and the State of New Mexico. Support has also come from several oil companies-although as is well known, they themselves are operating under greatly reduced research budgets. The following companies are supporting the PRRC's research into CO_2 applications: AMOCO Production Company, the Chevron Chemical Company, Marathon Oil Company, Mobil E&P, USA, Mobil Research and Evelopment Corporation, Parker & Parsley Development Company, and Texaco E&P Technology Department.

In addition to the Principal Investigators, mention must be made of the numerous other individuals who have participated actively in the research work. These include Drs. Jyun-Syung Tsau, S-H. (Eric) Chang, and Boyun Guo, as well as other laboratory technicians and graduate students: Charles Durbin, David Fritchman, James McLemore, Robert Svec, Chao Li, Ucok Saigian, and Hujuin Li. Also, thanks to Steve Anderson who put the document together. Finally a special thanks to John P. Heller and F. David Martin who retired during the second year of this project.

☆U.S. GOVERNMENT PRINTING OFFICE: 1996 - 559-031/40039